Search for the rare charm meson decays $D^0 \to h^- h^{(\prime)+} e^+ e^-$

by

Shuaiyan Kang

A dissertation submitted to the graduate faculty

in partial fulfillment of the requirements for the degree of

DOCTOR OF PHILOSOPHY

Major: High Energy Physics

Program of Study Committee:
Soeren Prell, Major Professor
Chunhui Chen
Kerry Whisnant
Steve Kawaler
Jonathan Smith

The student author, whose presentation of the scholarship herein was approved by the program of study committee, is solely responsible for the content of this dissertation. The Graduate College will ensure this dissertation is globally accessible and will not permit alterations after a degree is conferred.

Iowa State University

Ames, Iowa

2024

DEDICATION

I would like to dedicate this thesis to my parents, Feiming Huang and Lifeng Kang, without whose support I would not have been able to complete this work.

TABLE OF CONTENTS

Page

LIST OF TABLES

LIST OF FIGURES

ACKNOWLEDGMENTS

I would like to take this opportunity to express my thanks to those who helped me with various aspects of conducting research and writing of this thesis. First and foremost, I would like to thank my major professor, Soeren Prell, for all of the guidance in the physics analysis and my PhD journey. He has also given me advice on improving presentation and communication skills as well as written and oral English. I would like to specifically thank Professor Chunhui Chen and Jim Cochran for giving suggestions for my research and job applications. I would like to thank the Belle I + II charm group for giving me advice on my research and my analysis report. I would like to specifically thank Professor Giulia Casarosa for her help in progressing my analysis forward to the collaboration review of my analysis and Dr. Michel Bertemes and Professor Tom Browder for grammar checks of my paper draft. I would like to thank the ISU HEP group. I want to acknowledge Boping Chen, William Heidorn, Carlos Miguel Vergel Infante, and Roy McKay for giving support to my hardware work. I would like to thank Dr. Graham Beck for his support on my hardware project and job applications. I would also like to thank the ISU HEP group postdocs, Dr. Semma Choudhury and Dr. Michele Veronesi for their support.

I would also like to thank my committee members for their support, Professor Chunhui Chen, Professor Kerry Whisnant, Professor Steve Kawaler, and Professor Jonathan Smith.

ABSTRACT

A search of the rare charm meson decays $D^0 \to h^- h^{(\prime)+} e^+ e^-$, where $hh^{(\prime)} = KK$, $\pi\pi$, $K\pi$ is performed using a 942 fb^{-1} data set collected by the Belle detector at the KEKB asymmetric e^+e^- collider. The preliminary results are approved by the Belle (II) collaborations. The branching fraction of the decay $D^0 \to K^-\pi^+e^+e^-$ is measured to be (39.6 $\pm$ 4.5 (stat) $\pm$ 2.9 (syst)) $\times\ 10^{-7}$, in the ρ/ω mass region $675 < m_{ee} < 875\,\text{MeV}/c^2$. The branching fraction upper limits are set in the range $[2.3, 7.7] \times 10^{-7}$ for the decays $D^0 \to h^- h^{(\prime)+} e^+ e^-$ with ee in different mass regions. No beyond standard model contribution is found above than the background predictions. The measured $D^0 \to h^- h^{(\prime)+} e^+ e^-$ branching fraction upper limits are the tightest to date.

CHAPTER 1. INTRODUCTION

1.1 The standard model - particles, forces, and interactions

Where do we come from? What is matter made of? are some of the oldest questions ever asked by humans, and the answers have evolved through time. The Standard Model (SM), whose framework started building back to around the mid-20th century, was introduced by Abraham Pais and Sam Treiman in 1975 [1]. It is currently the most successful theory that explains phenomena and provides experimental predictions.

In the SM, there are two main groups of elementary particles, *fermions* and *bosons*. Figure 1.1 [2] shows the fermions and bosons of the SM of elementary particles. The *fermions* have spin $\frac{1}{2}$ which are the fundamental blocks of (anti-)matter, and they interact through the exchange of force carrier particles, called gauge (vector) *bosons* (spin 1). The only scalar boson (spin 0), *Higgs*, enables quarks, W/Z bosons, and charged leptons to acquire mass.

1.1.1 Fermions

As shown in Figure 1.1 [2], the fermions are divided into two main categories: quarks and leptons. There are three generations of fermions and their mass increases with generations. The six flavors of quarks are split into three up-type quarks (u, c, t) and three down-type quarks (d, s, b). The up-type quarks have a positive electrical charge (the magnitude of the negative electric charge carried by a single electron is $-1e$) of $+\frac{2}{3}e$, while the down-type quarks have a negative electrical charge of $-\frac{1}{3}e$. The six leptons are divided into three electrically charged leptons and corresponding neutrinos. Each of the six quarks and six leptons has its antiparticle with the same mass [1] but with opposite charge. The fermions carry one or two or all of the three

[1] The neutrino is massless in the SM.

charge(s) (color, electric, weak) and interact with the gauge bosons carrying the same type of charge. Table 1.1 summarizes the available interactions for each type of fermions.

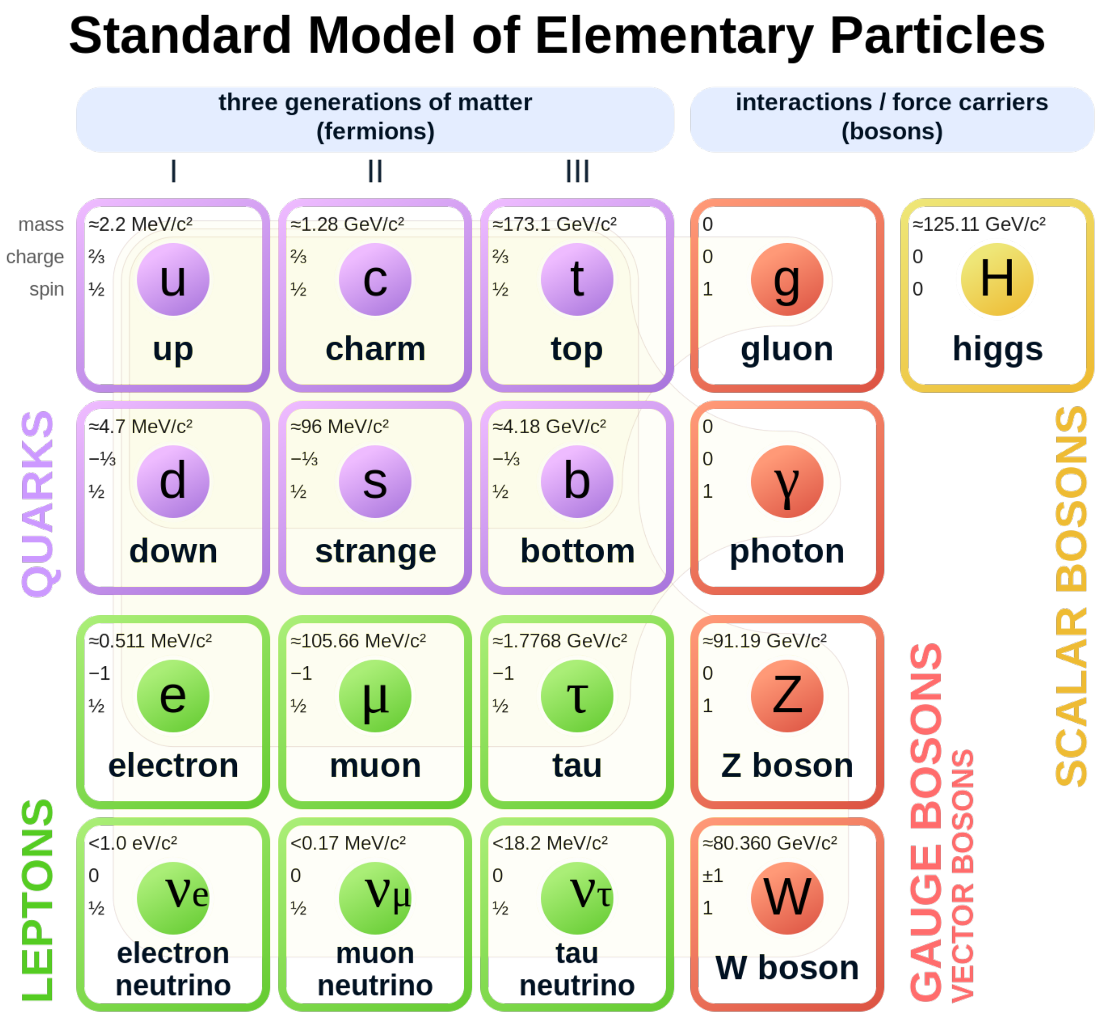

Figure 1.1: The elementary particles of the Standard Model. The three generations of fermions are colored in purple and green, the gauge bosons are colored in red, and the Higgs boson is colored in yellow [2].

1.1.1.1 Quarks

Table 1.1 shows that the quarks participate in all three interactions. Besides the electric charge they carry, the quarks also carry weak isospin (Section 1.1.2.2) of $+(-)\frac{1}{2}$, for the up (down)-type, respectively. Additionally, each quark carries a "color" charge (red, green, blue) so that they can participate in the strong interaction. Similarly, the anti-quark carries anti-red, anti-green, and anti-blue charges. The quarks are constrained by the color confinement (Section 1.1.2.3), which prevents the quarks from being isolated, thus observed in color-neutral hadrons which are formed by a quark-antiquark pair or three (anti)quarks [2]. For example, a meson is a type of hadron made up of a quark and an anti-quark, i.e., J/ψ ($c\bar{c}$), which contains one color anti-color pair (e.g., red anti-red) color charges to be color neutral. A baryon is another type of hadron made up of three (anti)quarks. For example, a proton is a baryon that contains three quarks uud, and the three quarks must have all three color charges as the sum of three different color charges forms a color-neutral state. The quarks can change their flavor through the weak interaction via the W^+ and W^- bosons, described in Section 1.1.2.2.

1.1.1.2 Charged Leptons

The leptons can be observed as free particles. The lightest charged lepton, electron e, was discovered by J. J. Thompson through deflecting the cathode rays emitted by a hot filament with a magnet in 1897 [3]. The second and third generation of charged lepton is muon μ and tau τ, whose masses are about 210 and 3500 heavier than the electron, respectively. The charged leptons carry a weak isospin of $+\frac{1}{2}$ while their anti-particles carry a weak isospin of $-\frac{1}{2}$. Like the quark flavors, the leptons have individual lepton flavor numbers (electron, muon, and tau number). For example, the electron and electron neutrino ν_e have an electron number of +1, and their antiparticle, position e^+ and electron anti-neutrino $\overline{\nu}_e$ have an electron number of −1. They are

[2] An exception for the "top" quark t, due to its heavier mass, the top quark decays before it forms a hadron

Table 1.1: Types of interactions that fermions (anti-fermions) can participate in.

Fermions (spin $\frac{1}{2}$)		Strong	Electromagnetic	Weak
up-type quark down-type quark	u, c, t d, s, b	✔	✔	✔
charged lepton neutrino	e, μ, τ ν_e, ν_μ, ν_τ	✖	✔ ✖	✔

expected to be conserved in the SM in the absence of neutrino mass. The higher generations of the charged lepton can decay to their lower generations. For example, μ decays to an electron with electron anti-neutrino and muon neutrino ($\mu^- \to e^- \,\overline{\nu}_e \,\nu_\mu$). The τ lepton is also able to decay hadronically (e.g., $\tau^- \to \nu_\tau \,\pi^-$) through the weak interaction because of its heavier mass. In the SM, the coupling strength to the lepton is independent of the lepton flavor.

1.1.1.3 Neutrinos

The neutrinos do not carry electric or color charges. As mentioned in the previous section, the electron-neutrino (ν_e), muon-neutrino (ν_μ), and tau-neutrino (ν_τ) are the three flavors (generations) of neutrinos. They have the individual lepton flavor numbers +1 for the neutrino and −1 for the anti-neutrino. On the other hand, the neutrinos are able to change their flavors via so-called neutrino oscillations, which proves that the neutrinos cannot be massless. The neutrinos are massless in the SM, but the Super-Kamiokande neutrino observatory showed that neutrinos have a non-zero mass in 1998 [4] through ν and $\bar{\nu}$ oscillations. The lepton flavor conservation is violated (LFV) in the neutrino oscillations. Searches have been made to find the charged lepton LFV process; for example, the $\mu \to e\gamma$ decays.

1.1.2 Forces and Bosons

The fermions interact through the exchange of force carrier particles. Quantum Field Theory (QFT) is a theoretical framework for elementary particle physics. It is also used for other areas of theoretical physics, such as condensed matter physics. QFT combines classical field theory, special relativity, and quantum mechanics, where particles and forces are represented as "excitations" of the fields. The symmetry groups describing the SM is $SU(3) \times SU(2) \times U(1)$. The $SU(3)$ symmetry group represents the Quantum Chromodynamics (QCD), which describes the strong interactions whose force carrier are gluons g (Section 1.1.2.3). The $SU(2) \times U(1)$ represents the electroweak interaction, which unifies the quantum electrodynamics (QED) of $U(1)$ symmetry and the weak interaction of $SU(2)$ symmetry. The force carrier of the electromagnetism is the photon γ (Section 1.1.2.1). The vector bosons W^+, W^-, Z (Section 1.1.2.2) mediate the weak interactions.

1.1.2.1 Photon

The photon is massless, so it cannot decay and interact with itself because of its neutral charge. This property enables the electromagnetic interaction to be infinite range, which potential is proportional to $\frac{1}{r}$. Photon interacts with quarks and charged leptons. The QED Lagrangian describing the interaction between the electromagnetic field and fermion (charged) is

$$\mathcal{L}_{QED} = \bar{\psi}(i\gamma^\mu \partial_\mu - m)\psi - ej^\mu A_\mu - \frac{1}{4}F_{\mu\nu}F^{\mu\nu} \tag{1.1}$$

where ψ is the fermion field, $\bar{\psi} = \psi\gamma^0$ is called "Dirac adjoint", γ^μ (γ^0, γ^1, γ^2, γ^3) are the 4×4 gamma matrices or "Dirac matrices", $j^\mu = \bar{\psi}\gamma^\mu\psi$ is the conserved $U(1)$ current, A_μ is the electromagnetic field, and $F_{\mu\nu} = \partial_\mu A_\nu - \partial_\nu A_\mu$ is the electromagnetic field tensor. The first term in the Lagrangian represents the free Dirac field Lagrangian, the second term represents the fermion-photon field interactions, and the last term is the kinetic term of the photon.

An example QED process is an electron and positron pair annihilate into a pair of charm and anti-charm quarks $e^+e^- \to c\bar{c}$, shown in the Feynman diagrams in Figure 1.2 (left). In this thesis, the left-hand side of a diagram represents the initial state, while the right-hand side represents the final state. The photon in the middle (internal lines) is a *virtual particle*. A virtual particle does not necessarily carry the same mass as the corresponding real particle (on-shell). The photon in this diagram is an off-shell photon whose mass is the e^+e^- energy in the center-of-mass frame.

1.1.2.2 W and Z bosons

The electrically-charged boson W^+, W^-, and neutral boson Z are the force carriers of the weak interaction. The W and Z bosons are massive, different from the photon and gluons (Section 1.1.2.3). Glashow, Weinberg, and Salam proposed these three bosons in the electroweak theory in the late 1960s [5]. Under the electroweak unification $SU(2)_L \times U(1)_Y$ [3], the weak interactions

[3] Y is the hypercharge, $Y = 2(Q - I_3)$, where Q is the electric charge and I_3 is the weak isospin.

only choose the left-handed (L) quarks and leptons, where the spin is opposite to the direction of the particle. The weak isospin is related to the handedness of the particle, where the left-handed charged lepton (neutrino) has a weak isospin of $-(+)\frac{1}{2}$, and the left-handed up (down)-type quarks have a weak isospin of $+(-)\frac{1}{2}$. The right-handed antiparticles have the opposite weak isospin of the corresponding left-handed particles, while all right-handed particles and left-handed antiparticles have 0 weak isospin. The parity and charge conjugation are separately violated in the weak interaction, while they are both conserved in the strong and electromagnetic interactions.

The charged lepton and quarks with neutral Z interactions act like the photon exchange in QED. Neither the lepton flavor nor the quark flavor will be changed. Figure 1.2 (right) shows an electron and positron pair annihilate into a virtual Z, decaying into a pair of charm and anti-charm quarks.

The electric charged boson W mediated weak interaction, however, is the only interaction that changes the flavor of quarks. The probability of the transition between the up and down type quarks is described by the elements of the Cabibbo-Kobayashi-Maskawa (CKM) matrix [6, 7], which is described in Section 1.1.3.

1.1.2.3 Gluons

The gluons are the force carriers of the strong interaction, described by quantum chromodynamics (QCD). The gluons carry color charges, so they can interact with themselves,

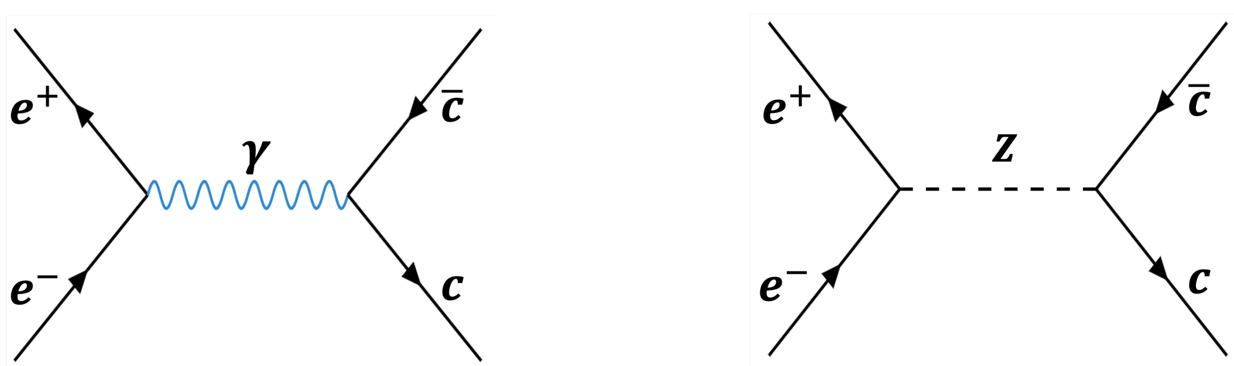

Figure 1.2: An example Feynman diagram of $e^+e^- \to c\bar{c}$ through a virtual photon (left) and through a virtual Z (right).

preventing the strong interaction from being infinite range. Only quarks can participate in strong interaction because only quarks carry color charges. The quarks change their color when interacting with gluons. There are eight gluons, which are linear combinations of two color-anticolor charge states.

Color confinement prevents the quarks and gluons from existing as isolated particles. For example, the strong interaction between a quark-antiquark pair (meson) is attractive. The strong interaction in a meson will become stronger if the distance between the quark-antiquark pair increases until a new quark-antiquark pair appears. On the other hand, the strong interaction between two quarks or two anti-quarks is repulsive, as two (anti) color charges cannot form a color-neutral state.

1.1.2.4 Higgs

The "last block" of the SM to be experimentally found was discovered by the ATLAS and CMS collaborations at the LHC in 2012 [8, 9, 10]. It was predicted by Francois Englert [11] and Peter Higgs [12] for solving the mass problem of gauge bosons. The SM particles (charged leptons, quarks, W, and Z vector bosons) gain their mass after the spontaneous symmetry breaking when interacting with the Higgs field. The process is called the Higgs mechanism, described in detail in [13, 14].

1.1.3 The CKM matrix

1.1.3.1 The Cabibbo angle

The weak interaction between the leptons and the W strictly proceeds within the same lepton generation; in other words, the lepton flavor is conserved. The quark flavor was also thought to be conserved, i.e., conservation of "up/down-ness", which holds in the observed beta decay involving $d \to u$ transition. However, the lightest strange baryon (Λ) decay to proton was observed, which is a cross-generation quark transition s (second generation) to u (first generation). When u, d and s were the only quarks known, Nicola Cabibbo 1963 proposed that the vertex of quarks weak interaction with W carries a factor [6], compared to the vertex of W with lepton coupling. The factor is cos θ_c for the $d-u$ coupling and sin θ_c for the $s-u$ coupling (cross generation). The θ_c is called "Cabibbo angle", which is about 13 degrees determined by experiment [2], which is small but non-zero.

1.1.3.2 The GIM mechanism

Cabibbo's theory successfully explained quite a few strangeness changing decays, but it also predicted a larger branching fraction of $K^0 \to \mu^+\mu^-$ decay compared to the experimental result. In 1970, Glashow, Iliopoulos, and Maiani (GIM) proposed a fourth quark, charm c, a counterpart of the up quark [5]. The charm quark c has the same charge as the up quark but has orthogonal couplings to the strange and down quarks with factors of cosθ_c and -sinθ_c, respectively. The actual lowest-order diagrams of $K^0 \to \mu^+\mu^-$ decay is a sum of two diagrams that interfere destructively because of the negative sign in the coupling of the c and d quark as shown in Figure 1.3. Thus, the total amplitude is largely canceled, and the calculated decay rate, considering the u/c mass difference, is consistent with the experimental value [15].

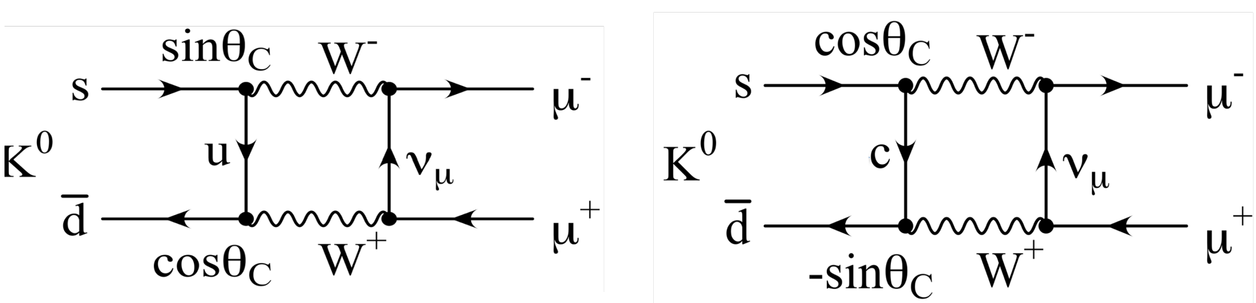

Figure 1.3: Diagrams of $K^0 \to \mu^+\mu^-$ at lowest order [16].

The Cabibbo-GIM scheme offers an interpretation of the conservation of quark flavors; the quark flavor states participating in the interaction are the Cabibbo-rotated states, where the matrix form is called the Cabibbo matrix.

$$\begin{pmatrix} d' \\ s' \end{pmatrix} = \begin{pmatrix} \cos\theta_c & \sin\theta_c \\ -\sin\theta_c & \cos\theta_c \end{pmatrix} \begin{pmatrix} d \\ s \end{pmatrix} \tag{1.2}$$

where the θ_c is the "Cabibbo angle". The primed quarks on the left are the down-type quarks flavor eigenstates, a superposition of down-type quarks mass eigenstates on the right. Now the W couples to the Cabibbo-rotated states $\binom{u}{d'}$, $\binom{c}{s'}$, in which the transitions between the up-type and down-type quarks happen within the same generation.

1.1.3.3 The Cabibbo–Kobayashi–Maskawa matrix

The charge conjugation and parity are found separately violated in the weak interactions. The transformation in which particles are exchanged with their antiparticles and their spatial coordinates are reversed, called CP, was believed to be conserved in the weak interaction. In 1964, the $K_L \to \pi^+\pi^-$ decay was observed with a small branching fraction at an order of $\mathcal{O}(10^{-6})$ [17]. In 1973, when only two generations of quarks were known (u, d, s), Kobayashi and Maskawa proposed that CP violation take place when there are at least three generations of quarks [7]. The charged weak interaction Lagrangian expressed in terms of the mass eigenstates is

$$L_{qqW} = \frac{g}{\sqrt{2}}(W_\mu^+ \bar{u}\gamma^\mu(1-\gamma_5)Vd + W_\mu^- \bar{d}\gamma^\mu(1-\gamma_5)uV^\dagger) \tag{1.3}$$

where g is the weak interaction coupling constant, W_μ is the 3-component $SU(2)$ gauge field, and the summation over all u-type and d-type quark fields is implicit. This is the famous Vector (γ^μ) − Axial vector ($\gamma^\mu\gamma^5$) (V-A) interaction, and the parity is maximally violated as they have the same strength. The V in the equation is the 6-quark model 3 × 3 Cabibbo, Kobayashi, and Maskawa (CKM) complex unitary matrix, which is an extension to the 2 × 2 Cabibbo matrix.

$$\begin{pmatrix} d' \\ s' \\ b' \end{pmatrix} = \begin{pmatrix} V_{ud} & V_{us} & V_{ub} \\ V_{cd} & V_{cs} & V_{cb} \\ V_{td} & V_{ts} & V_{tb} \end{pmatrix} \begin{pmatrix} d \\ s \\ b \end{pmatrix} \tag{1.4}$$

The unitarity of the CKM matrix gives

$$\sum_i V_{ij}V^*_{jk} = \delta_{jk} \tag{1.5}$$

There can be six distinct conditions for which the right-hand side of the equation becomes zero and can be represented as six triangles in the complex plane having equal area. One of the parametrizations of the CKM matrix is essentially expressed in terms of three Euler angles and one phase [18]. The complex phase has observable consequences of CP violation. The magnitudes of the matrix element are [2]

$$|V_{ij}| = \begin{vmatrix} 0.97373 \pm 0.00301 & 0.2243 \pm 0.0008 & 0.00382 \pm 0.00020 \\ 0.221 \pm 0.004 & 0.975 \pm 0.006 & 0.0408 \pm 0.0014 \\ 0.0086 \pm 0.0002 & 0.0415 \pm 0.0009 & 1.014 \pm 0.029 \end{vmatrix} \quad (1.6)$$

which represents the strength of mixing between an up-type quark and a down-type quark. The relatively stronger magnitudes are referred to as “Cabibbo favored” or “CKM favored,” which are the diagonal terms of the CKM matrix, V_{ud}, V_{cs}, and V_{tb}. While the off-diagonal elements are referred to as “Cabibbo suppressed” or “CKM suppressed.” Lincoln Wolfenstein introduced another parameterization of the CKM matrix with the four parameters λ, A, ρ, and η, where ρ and η correspond to the rates of CP violation [19]. The CKM matrix in Wolfenstein parameterization is written as [2]:

$$V_{\mathrm{CKM}} = \begin{pmatrix} 1 - \frac{\lambda^2}{2} & \lambda & A\lambda^3(\rho - i\eta) \\ -\lambda & 1 - \frac{\lambda^2}{2} & A\lambda^2 \\ A\lambda^3(1 - \rho - i\eta) & -A\lambda^2 & 1 \end{pmatrix} + \mathcal{O}(\lambda^4)$$

,where $\lambda \sim 0.22500$, $A \sim 0.826$, $\rho \sim 0.159$ and $\eta \sim 0.348$ [2]. The quark mixing between the same generation is the strongest ~ 1, between the first and second generations, is weaker $\sim \lambda$, while the mixing between the first and third generation is the weakest $< \lambda^3$.

1.1.4 Open questions of the SM

Although great successes have been achieved by the Standard Model, for example, the prediction of the Higgs, it still fails to explain some phenomena or conceptual questions. These unsolved phenomena indicate the existence of new physics (NP) or extensions of the SM.

Astrophysicists have discovered that only $\sim 5\%$ of the energy-matter density of the universe is ordinary matter, while the remaining 95% is divided into dark matter (DM) with 27% and dark energy (DE) with 68%. However, the SM of particle physics has no theory of DM or DE.

The second example is the matter-antimatter asymmetry. The Big Bang should have created equal amounts of matter and antimatter in the early universe. But nowadays, the antimatter is rarely seen in the universe. The CP violation in weak decays introduced by the CKM matrix in SM is insufficient to explain the observed asymmetry.

The observation of neutrino oscillations breaks the SM prediction of massless neutrino. The fourth fundamental force - gravitational force, has not been included in the SM. Some of the SM conceptual problems, like why there are three generations of leptons and quarks in SM, why is the mass range of the elementary particles so dispersed, and why there is no direct direction between leptons and quarks, are still unsolved.

1.2 Rare charm meson decays

1.2.1 The D meson

1.2.1.1 The discovery of charm quark

In 1974, simultaneous experiments led by Burton Richter at Stanford Linear Accelerator Center (SLAC) [20] and Sam Ting at Brookhaven National Laboratory (BNL) [21] observed a series of meson resonances.

Sam Ting and collaborators at BNL built a spectrometer designed to search for heavy particle J, which are expected to decay into an e^+e^- pair like a virtual photon does. The reactions to search for are

$$p + N \to J + X \to e^+e^- + X \tag{1.7}$$

, where N is a light nucleus and Be was used in the experiment, and X represents unreconstructed final state particles [21]. The spectrometer needs to separate electrons/positrons from background hadrons dominated by pions. A double-arm spectrometer was built, one for each charged particle, designed to accurately measure the magnitude ($|\vec{p}|$) and direction (θ) of the momentum of each charged particle. The spectrometer's high rejection power against hadrons is achieved through threshold Cerenkov counters and a calorimeter [4]. The invariant masses of the e^+e^- pair are

$$m(e^+e^-)^2 = (p_1 + p_2)^2 = 2E_1E_2 + 2m_e^2 - 2|\vec{p_1}||\vec{p_2}|cos(\theta_1 + \theta_2) \tag{1.8}$$

, where $p = (E, \vec{p})$ is the four-momentum of the electron/positron, $E_i^2 = m_e^2 + |\vec{p_i}|^2$, and θ_i is the angle relative to the beam direction. A resonance peak would show in the $m(e^+e^-)$ distribution if the particle J exists. Figure 1.4 (left) shows the $m(e^+e^-)$ distribution, and a narrow peak around 3100 MeV/c^2 can be seen.

At the same times, the SPEAR e^+e^- collider was operated at the SLAC with a maximum center-of-mass energy $\sqrt{s}$ of 8 GeV, with data collecting using the Mark I detector [20]. The cross sections[5] of the process $e^+e^- \to$ hardons, $e^+e^- \to ll(l = e, \mu)$ at different $\sqrt{s}$ are measured.

[4]Similar elements are also used in the Belle detector, described in Section 2.3.0.5.
[5]The cross section describes the probability of an event to occur given a collision.

Figure 1.4 (top right plot) shows a huge resonance with all the cross sections jumping by more than two orders of magnitude. The SLAC collaboration is called the particle ψ.

The new particle could not be an excitation of $q\overline{q}$ pair with $q = u$, d, or s because of the extreme narrowness of the resonances measured, and the measured width is limited by the detector resolution. Thus, a new quark flavor called charm (c) was discovered, and the J/ψ was identified as a $c\bar{c}$ bound state called charmonium. In the summer of 1974, Sam Ting's group at BNL found the particle J and kept it secret to validate the finding [22]. A few months later, Burton Richter's group at SLAC found the same particle ψ. Both groups simultaneously published their results in December 2$^{\text{nd}}$ 1974.

1.2.1.2 The D meson

The Mark I collaboration started the search for mesons containing charm quark at $\sqrt{s} \sim 4$ GeV in 1976, and a first resonance D^0 ($\bar{D^0}$) was observed in the neutral combinations, $K^-\pi^+(K^+\pi^-)$, with a mass around 1865 MeV and width less than the detector resolution [23]. Figure 1.5 shows the invariant mass spectra for neutral combinations of charged particle K and π.

The peaks can be seen in the Figure 1.5 (e) and (h) are corresponding to the Cabibbo favored $D^0 \to K^-\pi^+$ and $D^0 \to K^-\pi^+\pi^-\pi^+$ decays, which amplitudes proportional to the diagonal elements of CKM matrix. The other D^0 decay modes in Figure 1.5 are suppressed, called single Cabibbo suppressed decays, where the decay amplitude is proportional to the off-diagonal elements of the CKM matrix. Example Feynman diagrams of the Cabibbo favored decay $D^0 \to K^-\pi^+$, single Cabibbo suppressed decay $D^0 \to K^-K^+$, and double Cabibbo suppressed decay $D^0 \to K^+\pi^-$ are shown in Figure 1.6.

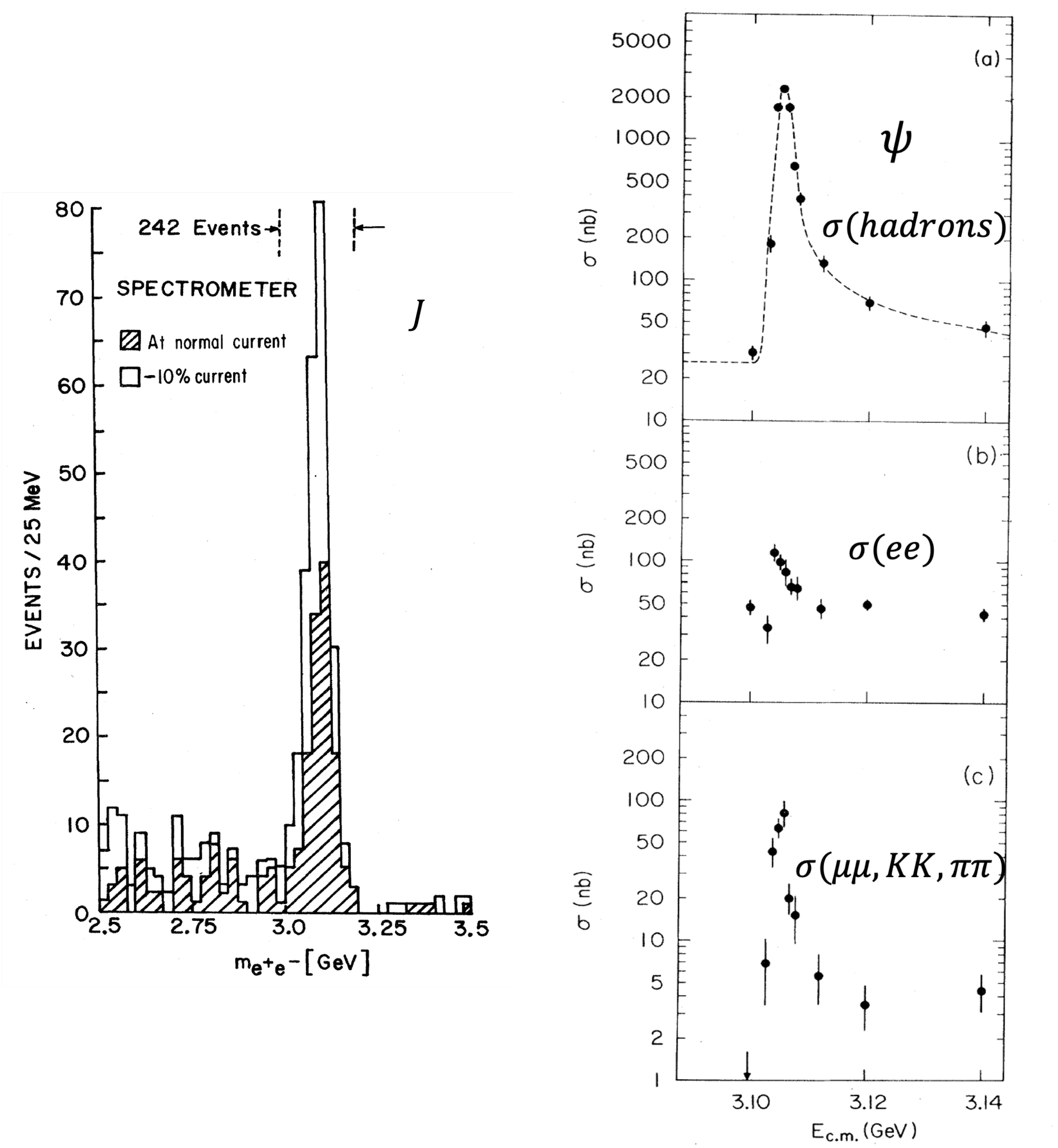

Figure 1.4: The J/ψ particle. The new particle J with a narrow peak around 3100 MeV/c^2 was discovered by BNL (left) [21]. The cross sections of the new particle ψ around 3100 MeV/c^2 discovered by SLAC (right) [20]

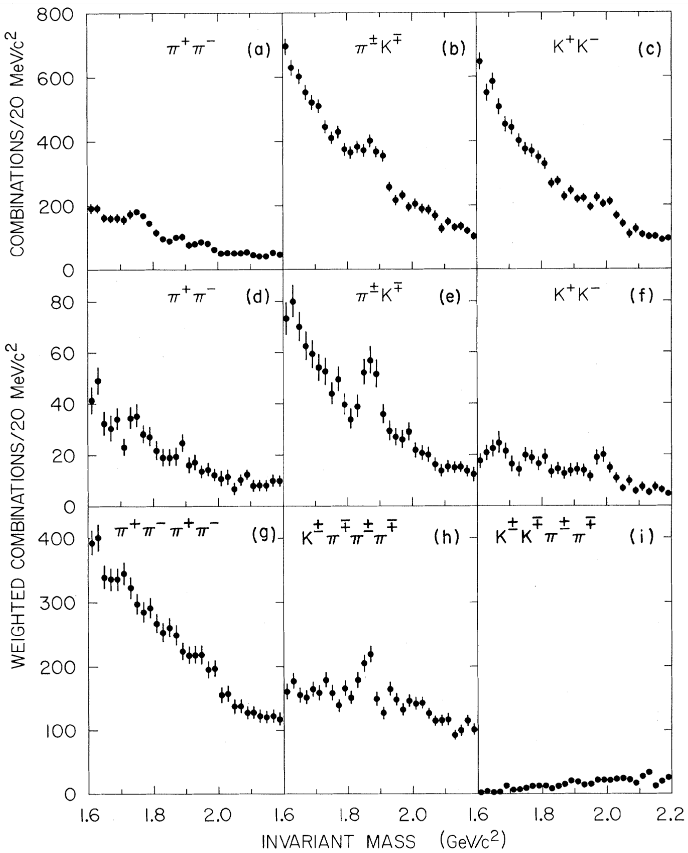

Figure 1.5: The observation of a new neutral state D^0. The invariant mass spectra for neutral combinations of charged particle K and π [23]. No particle identification (time-of-flight, detail in Section 2.3.0.4) is applied to the top row.

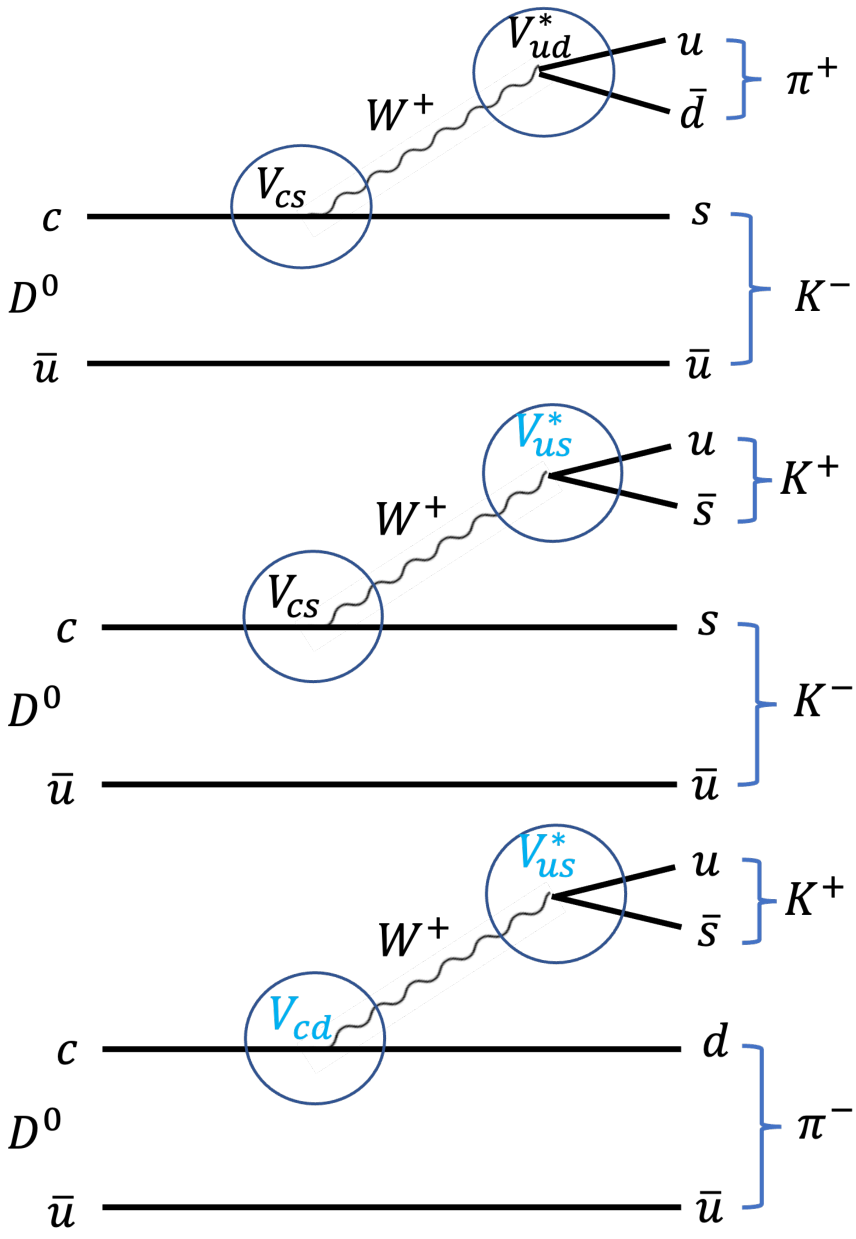

Figure 1.6: Feynman (tree-level) diagrams of $D^0 \to K^-\pi^+$, K^+K^-, and $K^+\pi^-$ decays. The corresponding CKM matrix elements are shown at the vertex. The Cabibbo-suppressed couplings are labeled in cyan. The branching fraction ($\mathcal{B}$) of the Cabibbo favored decay $D^0 \to K^-\ K^+$ is $\sim 3.9\%$, single Cabibbo suppressed $\mathcal{B}(D^0 \to K^-\ K^+)$ is $\sim 0.4\%$, and double Cabibbo suppressed $\mathcal{B}(D^0 \to K^+\ \pi^-)$ is $\sim 0.01\%$.

1.2.2 Rare charm meson decays $D^0 \to h^- h^{(\prime)+} l^+ l^-$

1.2.2.1 FCNC transitions

As mentioned earlier, the $K^0 \to \mu^+\mu^-$ decay is both loop and GIM suppressed[6]. The decay $K_L \to \mu^+\mu^-$ is a type of flavor-changing neutral current (FCNC) transition, which is a process that changes the flavor of fermion without altering the electric charge. Compared to the flavor changing charged current decay, which happens at the tree level mediated by the $W^\pm$ bosons, the FCNC is forbidden at the tree level in the SM as the neutral gauge bosons (Z, γ, and g) only couple to the fermions with the same flavor (flavor-diagonal). The FCNC process can be divided by the amount of change of flavor ΔF, i.e.,$K^0 \to \mu^+\mu^-$ decay changes the strange flavor $\Delta S = 1$.The FCNC is loop suppressed involving two virtual W exchanges, and it can be further suppressed through GIM and CKM suppression.

An example of a FCNC decay, $b \to s\gamma$, was first observed by CLEO Collaboration through the decay of $B^0 \to K^{*0}(892)\gamma$ and $B^- \to K^{*-}(892)\gamma$ in 1993 [24]. The $b \to s\gamma$ decay shown in Figure 1.7 is an electroweak "penguin" decay [25].

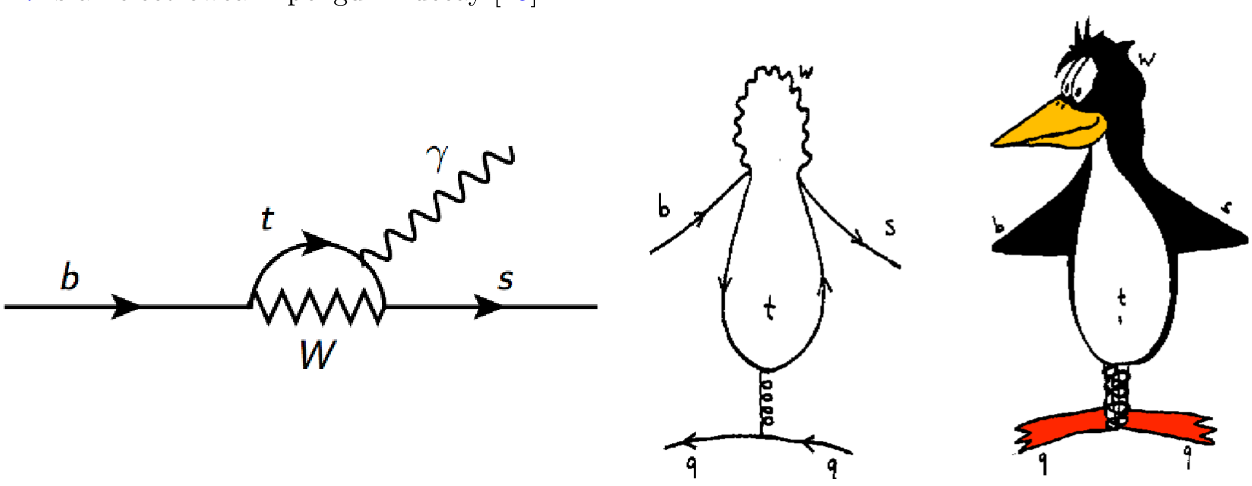

Figure 1.7: The $b \to s\gamma$ decay Feynman loop diagram and the penguin drawings [25].

The amplitude independent of the internal quark mass will vanish because $\sum_i V_{ib}^* V_{is} = 0$. However, the GIM suppression is less effective for the $b \to s\gamma$ decay because the top t quark is the

[6] The top quark contribution is also CKM suppressed due to the small CKM elements $V_{td}V_{ts}$.

heavies quark among other quarks and W mass. Thus the $b \to s\gamma$ amplitude reduces to $\mathcal{M} \propto V_{tb} V_{ts}^* m_t^2 / m_W^2$.

1.2.2.2 The $c \to u\,\ell\ell$ decays

Electroweak penguin decays like $b \to sll, b \to dll$ and $c \to ull$ proceeded via FCNC are (heavily) loop suppressed in the SM, which is a rare process in the SM and thus considered as probes for new physics (NP),i.e., a new heavy resonance particle can give significant virtual contributions that deviate from the SM. Compared to the decays $b \to s\,\ell^+\ell^-$ and $b \to d\,\ell^+\ell^-$, the $c \to u\,\ell\ell$ decays in the SM are further suppressed due to the GIM mechanism, CKM suppression, and the small quark masses in the loop.

The difficulty of interpreting the flavor changing amplitudes is that it involves separated mass scales, ranging from QCD $\Lambda \sim 350\,\mathrm{MeV}$ to $m_t \sim 165\,\mathrm{GeV}$ [26]. The Effective Field Theory (EFT) provides a systematic formalism for analyzing multi-scale problems. It is a QFT evaluated at a given energy range, and it allows a model-independent treatment to calculate the flavor-changing amplitudes. The effective Lagrangian for the $c \to u\,\ell\ell$ transition valid at a given scale of interest $\Lambda \sim m_c$ is given by [27, 28]:

$$\mathcal{H}_{\mathrm{eff}} = \lambda_d \mathcal{H}^d + \lambda_s \mathcal{H}^s + \lambda_b \mathcal{H}^{\mathrm{peng}} \tag{1.9}$$

where the CKM weights $\lambda_i = V_{ci}^* V_{ui}$ and V_{ij} are the CKM matrix elements. The first two effective Hamiltonians containing the four-quark operators $\mathcal{O}_{1,2}$ with the corresponding Wilson coefficients $\mathcal{C}_{1,2}$ which represent effective strength of the interactions are given by [28]:

$$\mathcal{H}^{q=d,s} = -\frac{4G_F}{\sqrt{2}}(\mathcal{C}_1\mathcal{O}_1 + \mathcal{C}_2\mathcal{O}_2) \tag{1.10}$$

$$\mathcal{O}_1 = (\bar{q}_L^{\alpha}\gamma^{\mu}c_L^{\alpha})(\bar{u}_L^{\beta}\gamma_{\mu}c_L^{\beta}),\;\; \mathcal{O}_2 = (\bar{q}_L^{\alpha}\gamma^{\mu}c_L^{\beta})(\bar{u}_L^{\beta}\gamma_{\mu}c_L^{\alpha}) \tag{1.11}$$

where G_F is the Fermi constant, $q_{L/R}$ is the left (right) handed quark, and α/β is the color index. The explicit form of $\mathcal{H}^{\mathrm{peng}}$ is [27]

$$\mathcal{H}^{\mathrm{peng}} = -\frac{4G_F}{\sqrt{2}}(\sum_{i=3,\ldots 10} \mathcal{C}_i\mathcal{O}_i) \tag{1.12}$$

with the QCD penguin operators $\mathcal{O}_{3,\ldots,6}$, electromagnetic operator $\mathcal{O}_7$, chromomagnetic operator $\mathcal{O}_8$, and NP sensistive electroweak penguin operators $\mathcal{O}_9$ (vector component), $\mathcal{O}_{10}$ (axial vector component) defined as [27]:

$$\mathcal{O}_9 = \frac{e^2}{(4\pi)^2}(\bar{u}\gamma^\mu P_L c)(\bar{l}\gamma_\mu l), \;\; \mathcal{O}_{10} = \frac{e^2}{(4\pi)^2}(\bar{u}\gamma^\mu P_L c)(\bar{l}\gamma_\mu \gamma_5 l) \tag{1.13}$$

, where $P_{L/R}$ is the left (right) handed projector $(1 \mp \gamma_5)/2$.

NP appears as the shift of the Wilson coefficients

$$\mathcal{C}(\mu)_i = \mathcal{C}(\mu)_i^{SM} + \mathcal{C}(\mu)_i^{NP} \tag{1.14}$$

where μ represents the energy scale, and NP represents the effect of new physics. With a significant amount of signal observed, one can further search for new physics by extracting the Wilson Coefficients from physics observables and comparing them with the SM predictions.

Many extensions of the SM predict the existence of new, heavy particles that couple to the SM fermions and bosons. Amplitudes from these NP contributions can interfere with those from the SM, altering physics observables from the SM predictions (e.g., total and differential decay rates, decay-angular distributions, *CP*, and lepton-flavor universality (LFU)). The recent $b \to s\,\ell^+\ell^-$ analysis results performed by *BABAR* [29], Belle [30], and LHCb [31, 32, 33, 34, 35] show consistency with SM predictions.

1.2.2.3 The $D^0 \to h^- h^{(\prime)+} l^+ l^-$ decays

The decays $D^0 \to X^0 \ell^+ \ell^-$, where X^0 is a light-quark system and $\ell = e$ or μ, can have contributions from both short-distance (SD) and long-distance (LD) amplitudes. The short-distance contributions arise from the electroweak box or loop diagrams (Figure 1.8). Their branching fractions are predicted to be at most 2×10^{-9} [36]. However, long-distance contributions from photon pole or vector meson dominance (VMD) amplitudes (Figure 1.9), which proceed through the decays $D^0 \to X^0(\gamma^*/V^0) \to X^0 \ell^+ \ell^-$, where γ^* is a virtual photon and V^0 is an intermediate pseudoscalar or vector meson, can be up to 2×10^{-6} [36]. SM predictions for SD and LD contributions to the branching fractions of $D^0 \to X^0 \ell^+ \ell^-$ decays are given in Table 1.2.

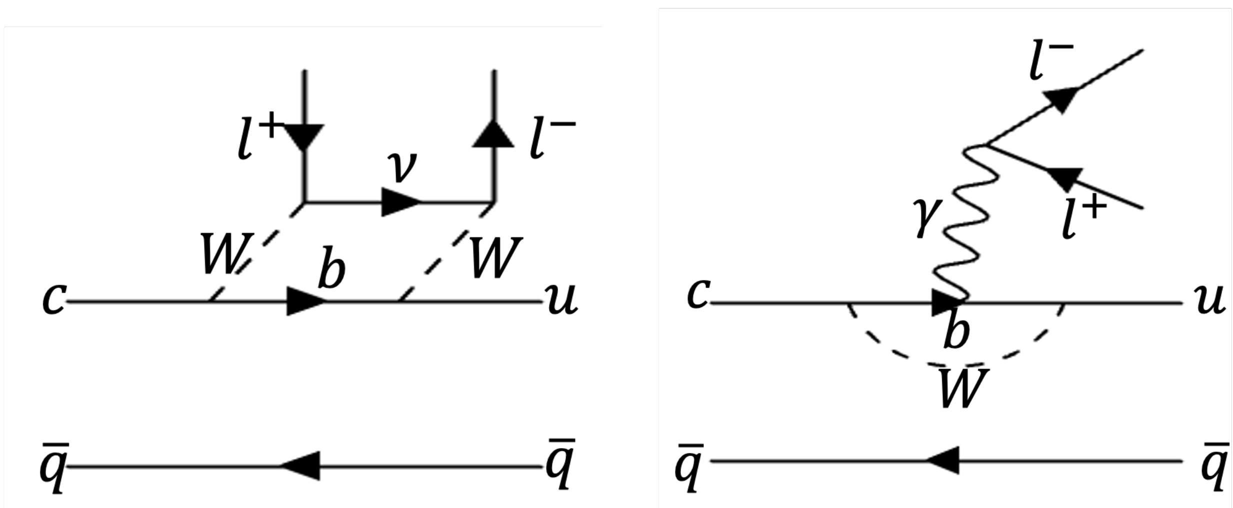

(a) (b)

Figure 1.8: SD contributions to FCNC D decays through the electroweak box (a) and loop (b) diagrams.

Several new physics models such as leptoquarks, minimal supersymmetric standard model (MSSM), little Higgs, Z' model, and models with warped extra dimensions predict significantly enhanced rates for $c \to u\, \ell^+ \ell^-$ decays, deviations from SM decay-angular distributions as well as the presence of lepton flavor conservation violating transitions and CP symmetry violation [37, 38, 39, 40]. For example, branching fractions of $D \to X \ell^+ \ell^-$ decays are found to be $\mathcal{O}(10^{-10})$ in a leptoquark model [41]. Thus, limits (details about the upper limit are in Section 4.1.3) on the

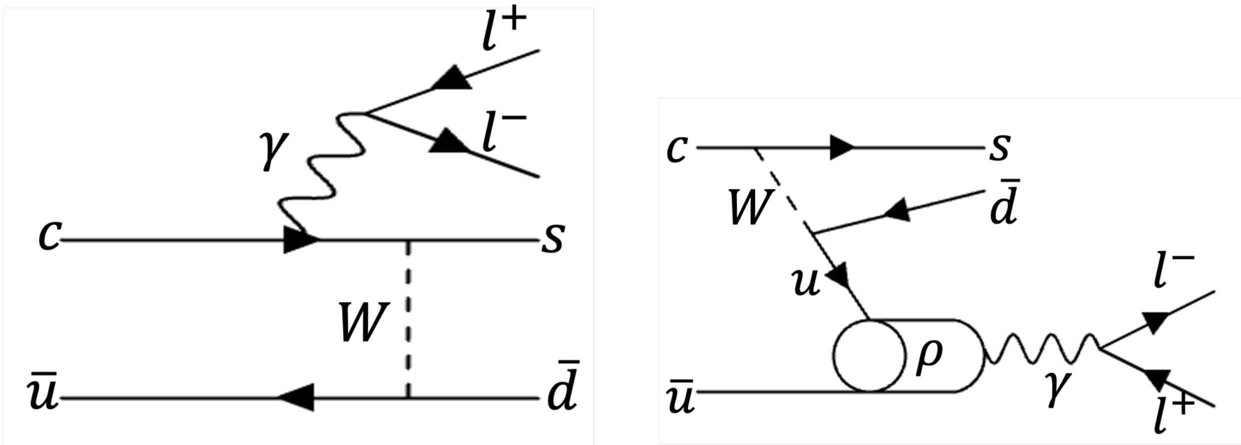

(c) (d)

Figure 1.9: LD contributions to $D^0 \to X^0 l^+ l^-$ decays through photon pole (c) and VMD (d) diagrams.

branching fractions of $D^0 \to X^0\ell^+\ell^-$ decays allow us to probe for NP and to characterize the long-distance contributions to the decay amplitudes.

The *BABAR* [42, 43, 44, 45], BES III [46], CLEO II [47], Fermilab E653 [48] and E791 [49], and LHCb [50, 51, 52] Collaborations have searched for rare and forbidden $c \to X\,\ell\ell^{(\prime)}$ decays in several final states. Recently, several four-body decays $D^0 \to hh'\ell^+\ell^-$ (where $h, h' = K^\pm, \pi^\pm$) have been observed. *BABAR* has observed the decay $D^0 \to K^-\pi^+e^+e^-$ in the mass range $0.675 < m_{e^+e^-} < 0.875$ GeV/c^2 at a rate compatible with VMD contributions [43] and the decay $D^0 \to K^-\pi^+\mu^+\mu^-$ previously observed by LHCb [50]. LHCb has also observed the decays $D^0 \to \pi^-\pi^+\mu^+\mu^-$ and $D^0 \to K^-K^+\mu^+\mu^-$ [51]. *BABAR* has set branching fraction upper limits in the range (1-44)$\times 10^{-6}$ at 90% confidence level (CL) for the decays of the form $X_c^+ \to h^\pm\ell^\mp\ell^{(\prime)+}$, where X_c^+ is a charged charm hadron (D^+, D_s^+, Λ_c^+) based on 0.384 ab^{-1} of e^+e^- annihilation data collected near the Υ(4S) resonance [42]. LHCb has searched for the decay $\Lambda_c^+ \to p\mu^+\mu^-$ and set the upper limit $\mathcal{B}(\Lambda_c^+ \to p\mu^+\mu^-) < 7.7 \times 10^{-8}$ at 90% C.L. [52]. CLEO II has set branching fraction upper limits from 45×10^{-6} to 180×10^{-6} at 90% C.L. for the decays $D^0 \to X^0\ell^+\ell^{(\prime)-}$, where X^0 is a $\pi^0, \eta, K_S^0, \rho^0, \omega, \phi$ or $\bar{K}^{*0}$ meson and $\ell = e, \mu$ with 3.85 fb^{-1} of e^+e^- annihilation data collected near the Υ(4S) resonance [47]. BES III has set branching fraction upper limits in the range (4-12)$\times10^{-6}$ at 90% CL for the decays $D^0 \to X^0 e^+e^-$, where X^0 is a π^0, η, K^0_S, or ω meson, and in the range (11-41) for the decays $D^0 \to h^- h^{(\prime)+} e^+ e^-$ [46].

Table 1.2: Measured branching fractions or 90% C.L. upper limits ($\times10^{-6}$) of the rare decays $D^0 \to hh^{(\prime)}\ell^+\ell^-$ along with estimates for branching fractions uncertainties or upper limits with the full Belle dataset (1 ab^{-1}) and a 5 ab^{-1} Belle II dataset. The corresponding Standard Model predictions for the SD and LD contributions to the branching fractions are also given [36, 37, 53].

$D^0 \to$	$\mathcal{B}$ measured	Belle expected $\sigma(\mathcal{B})$ or $\mathcal{B}$ UL	Belle II expected $\sigma(\mathcal{B})$ or $\mathcal{B}$	SM SD $\mathcal{B}$	SM LD $\mathcal{B}$
$\pi^+K^-\mu^+\mu^-$	$4.17 \pm 0.12 \pm 0.40$ [50]	±0.35	±0.16		~ 10
$\pi^+K^-e^+e^-$	$4.0 \pm 0.5 \pm 0.2$ [43]	±0.35	±0.16		~ 10
$\pi^+\pi^-\mu^+\mu^-$	0.96 ± 0.12 [51]	±0.35	±0.16		~ 1
$\pi^+\pi^-e^+e^-$	< 7 [46]	±0.35	±0.16		~ 1
$K^+K^-\mu^+\mu^-$	0.15 ± 0.03 [51]	< 0.7	< 0.32		~ 0.1
$K^+K^-e^+e^-$	< 11 [46]	< 0.7	< 0.32		~ 0.1
$\pi^0\ell^+\ell^-$	< 4 [46]	< 3.7	< 1.7	1×10^{-6}	0.21
$\eta\,\ell^+\ell^-$	< 3 [46]	< 7.7	< 3.5	2.5×10^{-4}	0.05
$\eta'\ell^+\ell^-$	—			9.7×10^{-6}	0.02
$\bar{K}^0\ell^+\ell^-$	< 24 [46]	< 7.7	< 3.5	0	0.43

The analysis searches the full Belle data set for the decays $D^0 \to h^- h^{(\prime)+} e^+ e^-$, where $h^{(\prime)} = K, \pi$. The research objective is divided into two parts. The first part is probing the NP at m_{ee} regions where the ee resonance contributions are relatively small, i.e., as shown in Figure 1.10, and probing the potential NP contribution to the FCNC process $c \to u\, e^+e^-$ through $D^0 \to \pi^-\pi^+e^+e^-$, $K^-K^+e^+e^-$ decays in particular. The second part is searching for the $D^0 \to h^- h^{(\prime)+} e^+ e^-$ decay with ee at potential resonances, especially to confirm the branching fraction of the Cabibbo favored long-distance decay $D^0 \to K^-\pi^+e^+e^-$ with m_{ee} at $m_{\rho/\omega}$ region with recent *BABAR* measurements [43].

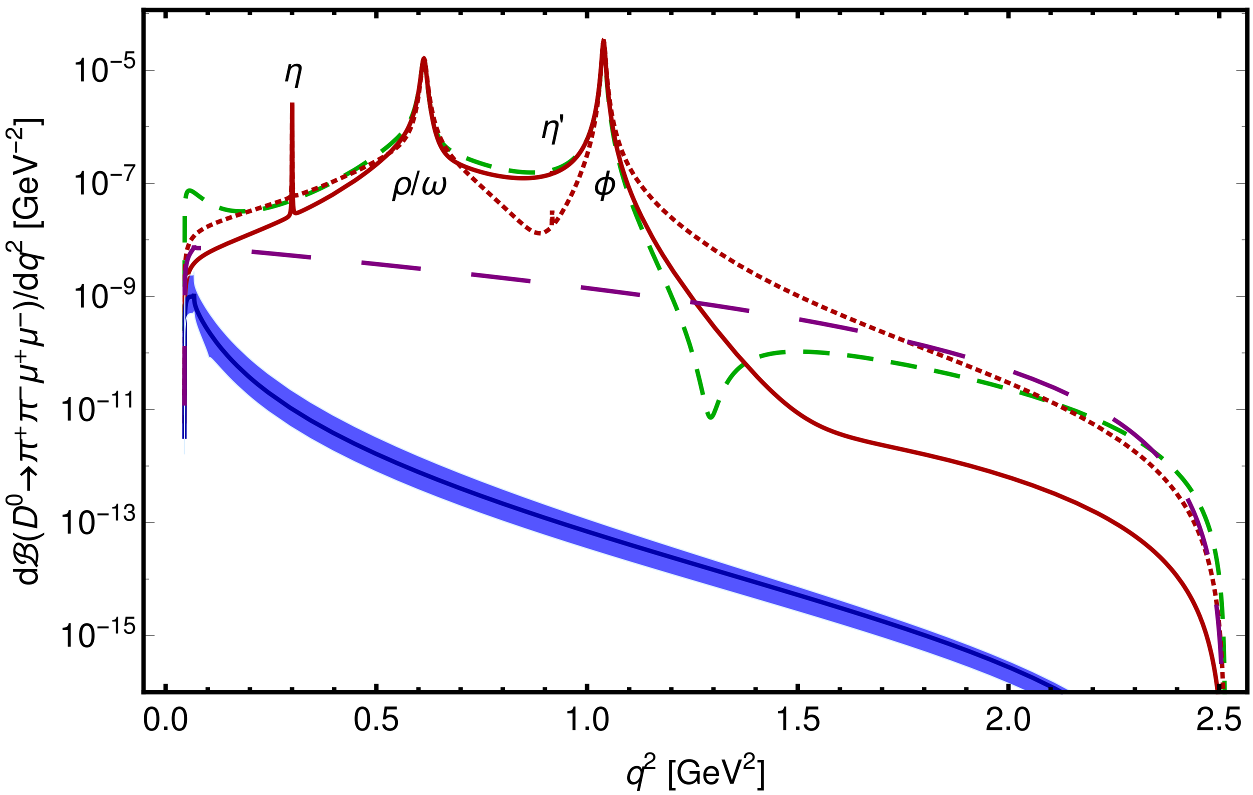

Figure 1.10: $D^0 \to \pi^-\pi^+\mu^+\mu^-$ differential branching fraction ratio $d\mathcal{B}(D^0 \to K^-\pi^+\mu^+\mu^-)/dq^2$, where q^2 is di-muon invariant mass squared. The solid blue band corresponds to the prediction of SM nonresonant contributions with uncertainties. The long-dashed purple curve predicts NP nonresonant contribution. The red and green curves represent SM resonant contributions, whose distribution includes uncertainties related to different relative strong phase between ρ and ϕ [54]. The resonant contributions are relatively smaller at q^2 regions away from $\eta, \rho/\omega, \phi$ regions (m^2), which give room for probing potential NP contribution in nonresonant regions.

CHAPTER 2. THE BELLE EXPERIMENT

2.1 e^+e^- collisions

The objective is to find the events from the rare decays $D^0 \to h^- h^{(\prime)+} l^+ l^-$. The production of a particular type of event (N) is then given by the product of the instantaneous luminosity ($\mathcal{L}$) and the cross section (σ)

$$\frac{dN}{dt} = \mathcal{L} \cdot \sigma \tag{2.1}$$

The instantaneous luminosity has a unit of $\mathrm{cm}^{-2}\mathrm{s}^{-1}$, which refers to the flux of particles crossing the interaction area in a given time interval. The cross section is a measurement of the probability of a specific scattering process under some given set of initial and final conditions, which describes the probability of an event to occur given a collision. For example, the cross section of a scattering process between two point-like particles described as $q_1 + q_2 \to q_3 + q_4$ is given by Fermi's golden rule [15]

$$\sigma = \frac{1}{64\pi^2 s} \frac{|p_f|}{|p_i|} \int |\mathcal{M}|^2 d\Omega \tag{2.2}$$

, where the energy of the system ($\sqrt{s}$), the momenta (p) of the initial and final state particles, and the solid angle ($d\Omega$) are all evaluated in the center-of-mass frame. The $\mathcal{M}$ is the amplitude calculated by the Feynman diagrams, e.g., the lowest order $e^+e^- \to q\bar{q}$ amplitude gives [15]

$$\mathcal{M} = \frac{Qg^2}{(p_{e^+} + p_{e^-})^2} [\bar{\nu}(e^+)\gamma^\mu u(e^-)][\bar{u}(q)\gamma_\mu v(\bar{q})] \tag{2.3}$$

where Q is the electric charge in unit of e, g is the QED coupling constant, and p is the four momentum $(E, \vec{p})$ of the particles. Figure 2.1 shows the the cross section of e^+e^- annihilation into hadrons as a function of the e^+e^- center-of-mass energy.

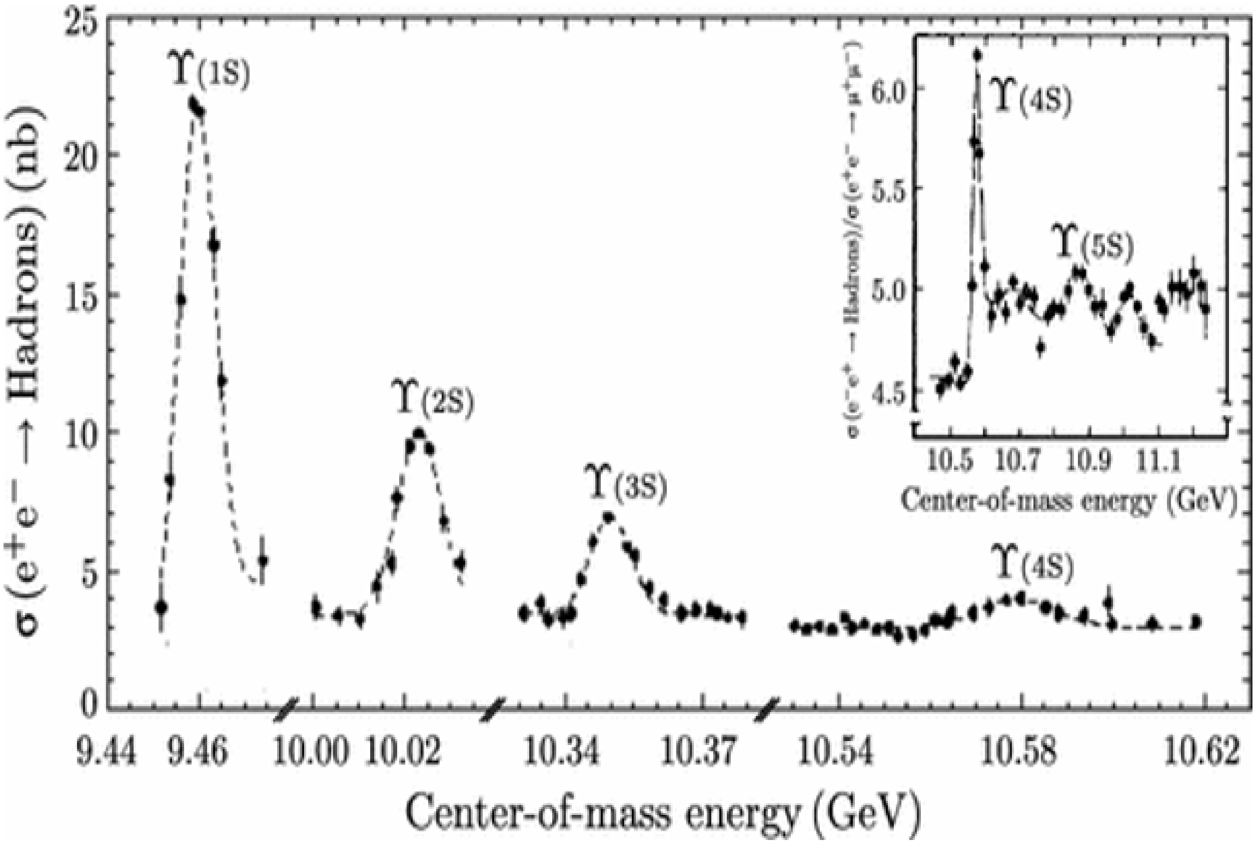

Figure 2.1: Cross section $e^+e^- \to$ hadrons vs center-of-mass energy [55] The peaks correspond to the process of $e^+e^- \to b\bar{b}\,(\Upsilon(nS))$, which forms the $\Upsilon(nS)$ resonances. The e^+e^- annihilation to other quark anti-quark pairs $e^+e^- \to u\overline{u}, d\overline{d}, s\overline{s}, c\overline{c}$ are shown below and between the resonance peaks. .

2.2 The KEKB accelerator

The KEKB accelerator [56] is a two-ring asymmetric-energy e^+e^- collider aiming to produce $B\overline{B}$ mesons, also called the "B factory." The "KEKB" consists of two 3 kilometers long storage rings, one storing 8 GeV electrons and the other storing a 3.5 GeV positrons ring, and an injection linear accelerator that accelerates the electrons and positrons. Figure 2.2 gives a schematic of KEKB. The two rings cross at one point called the interaction point (IP). Since the center-of-mass energy is slightly above the mass threshold of $\Upsilon(4S)$ (10.58 GeV), the B mesons are almost at rest in the center of mass frame, where their decay particles are isotropically distributed. While the "continuum" process, i.e., the $c\bar{c}$ pairs ($e^+e^- \to c\bar{c}$) are boosted because they are produced with center-of-mass energy much greater than their rest mass, where their decay particles are strongly directional.

The luminosity of an e^+e^- collider is given by

$$\mathcal{L} = \frac{N_b n_{e^+} n_{e^-} f}{A_{eff}} \tag{2.4}$$

, where n is the number of electrons/positrons in each bunch [1], N_b is the number of bunches, f is the circulation frequency, and A_{eff} is the effective cross-sectional area of the beams at the IP [57]. In KEKB, the electron and positron beams collide at a small crossing angle ($\pm$ 11 mrad), which allows for a shorter bunch spacing and thus higher luminosity [57]. The data collecting period is over ten years from June 1999 to June 2010.

[1] A bunch is a packed group of particles traveling together within a particle accelerator

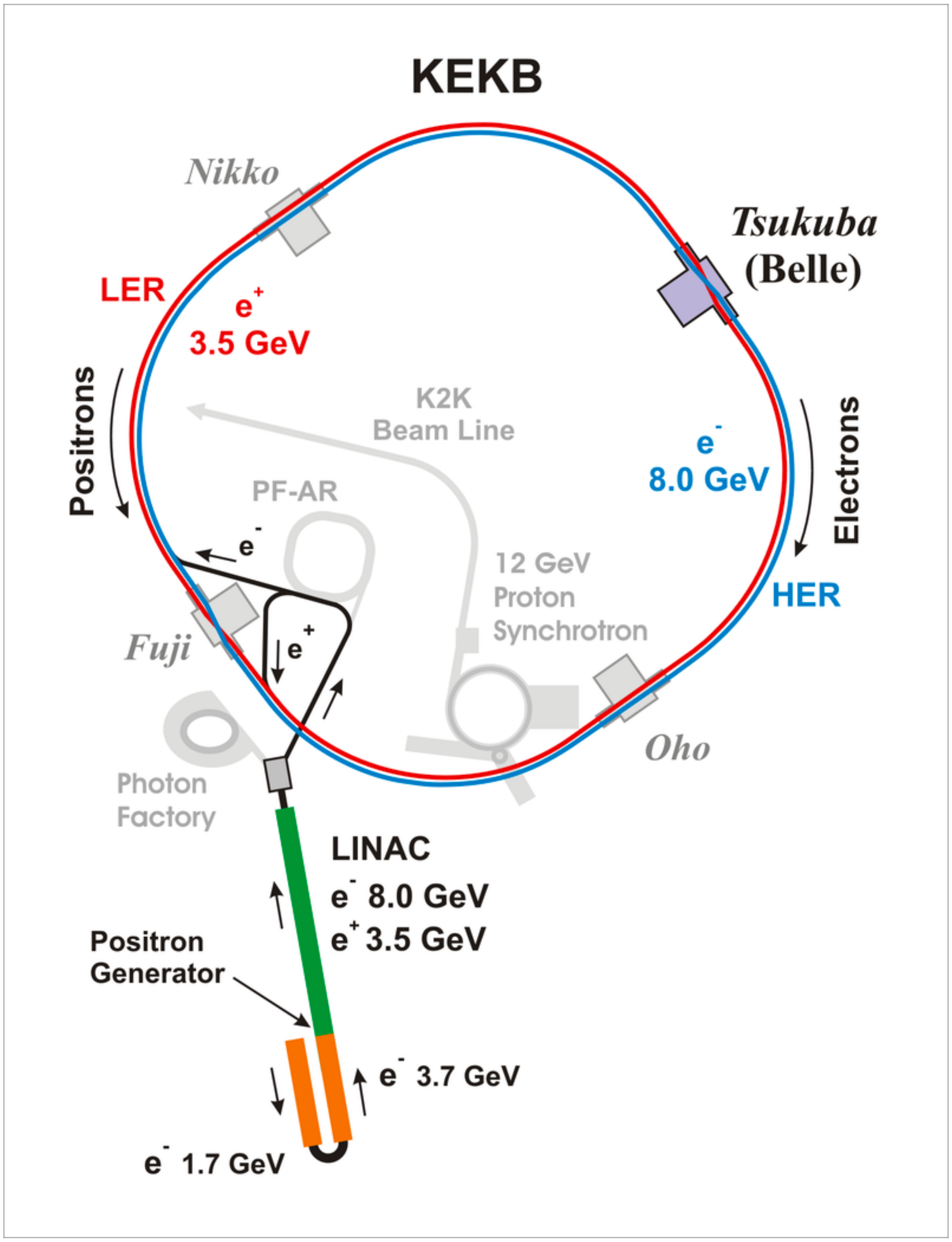

Figure 2.2: Schematic view of the KEKB accelerator [56]

2.3 The Belle detector

An overview of the Belle detector and a schematic longitudinal cross section of the Belle detector is shown in Figure 2.3. The detector is composed of a barrel part, a forward part, which is in the direction of the incoming e^- beam, and a backward part, which is in the direction of the incoming e^+ beam. The coordinate system used in the Belle detector is: the x-axis and y-axis are horizontal and vertical points away from the center of the KEKB ring, and the z-axis is in the opposite direction of the e^+ beam. The $x - y$ plane is orthogonal to the beam direction and referred to as the transverse plane. Cylindrical coordinates (r, ϕ) are used in the $x - y$ plane with the azimuthal angle ϕ around the beam direction. The Belle sub-detectors from inside to outside are silicon vertex detector (SVD), central drift chamber (CDC), aerogel Cerenkov counters (ACC), time-of-flight counters (TOF), CsI(Tl) crystal calorimeters (ECL), K_L^0 and muon detector (KLM). The SVD, CDC, TOF, ACC, and ECL are located inside a superconducting solenoid of a 1.7 m radius that maintains a 1.5 T magnetic field.

2.3.0.1 Silicon vertex detector

The silicon vertex detector is the innermost part of the Belle detector. The SVD is used to reconstruct vertices, measure the momentum of low-energy charged particles, and provide angles and positions to the second tracking detector - CDC.

The SVD1 was used in the first three years and consisted of three layers of double-sided silicon strip detectors (DSSD). Figure 2.4 shows the geometry of SVD1. It contains 102 DSSDs in total. Its coverage is $23° < \theta < 140°$ while the full acceptance of the Belle detector is $17° < \theta < 150°$.

The SVD2 replaced SVD1 in the summer of 2003 with the coverage increased to the acceptance of the CDC $17° < \theta < 150°$. Figure 2.5 shows the geometry of SVD2. It consists of four layers of DSSD and contains 138 DSSDs in total.

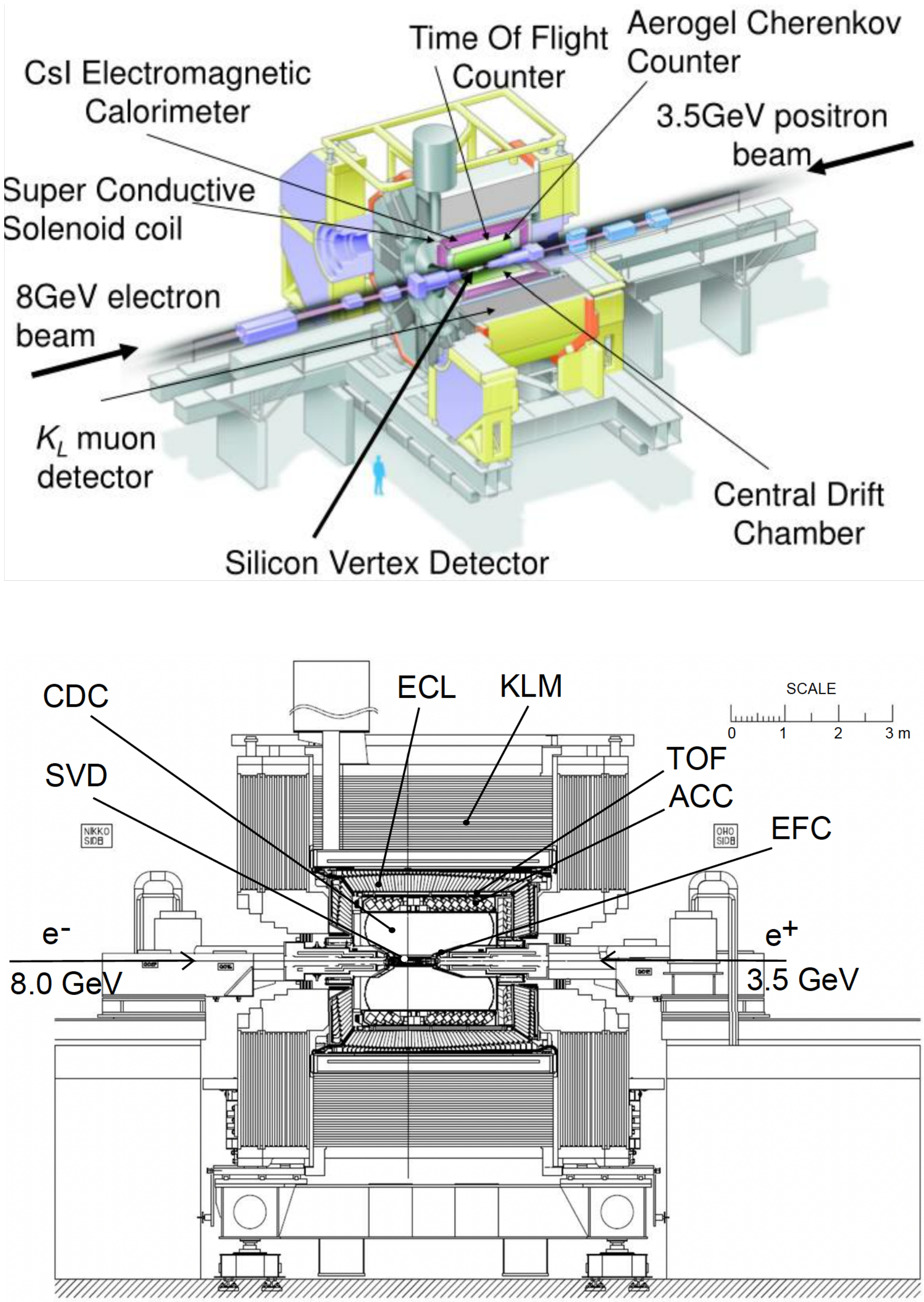

Figure 2.3: The overview of the Belle detector [57].

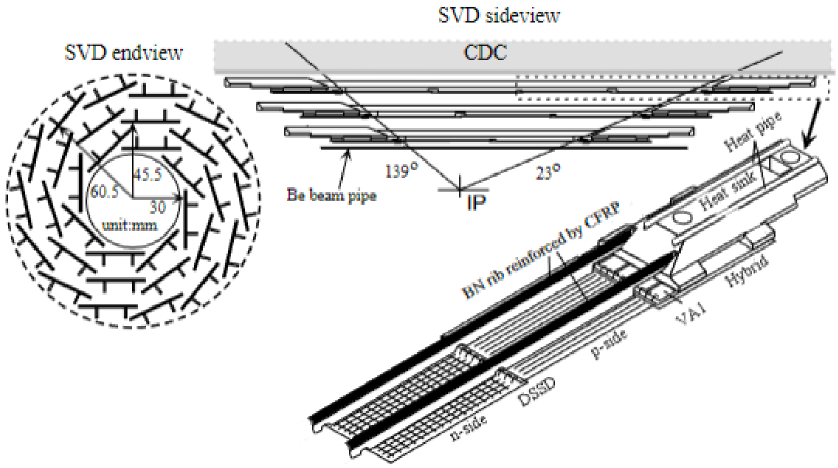

Figure 2.4: The SVD1 sub-detector configuration. [58]

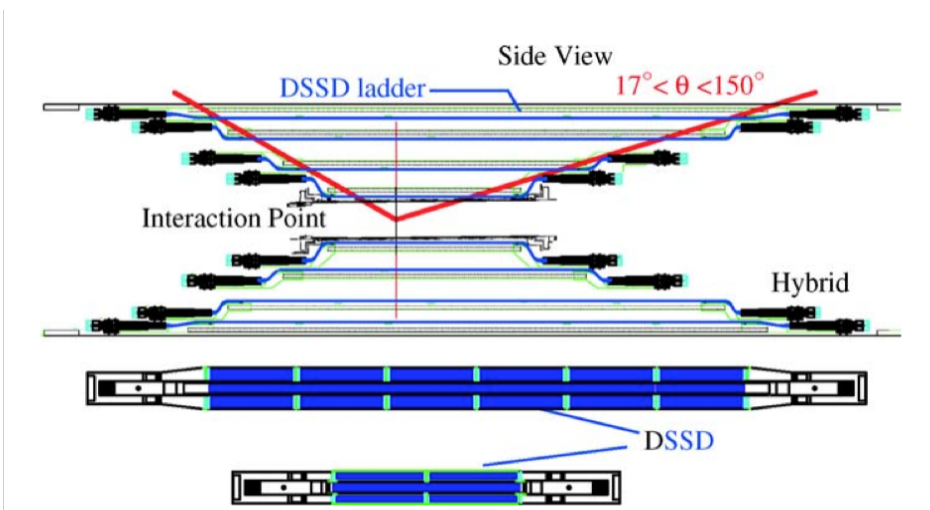

Figure 2.5: The SVD2 sub-detector configuration. [59]

2.3.0.2 Central drift chamber

The Central Drift Chamber precisely measures the particle momenta and helps with particle identification (PID) by measuring the energy loss (dE/dx). The CDC reconstructs tracks by precisely measuring their hit coordinates left by the charged particles in the detector volume, enabling their momentum reconstruction. The charged particles lose energy while traveling within the CDC volume and the dE/dx measurement is used in the particle identification (PID).

Figure 2.6 shows the geometry of CDC. The CDC is asymmetric in the z direction, and it covers an angular range of $17° < \theta < 150°$. The inner radius is 103 mm, and the outer radius is 874 mm. The chamber has 50 layers of anode wires, 32 axial (parallel to the z axis), 18 stereo (slant to the z axis to differentiate hits at different z positions) wire layers, and three cathode strip layers. The CDC has 8400 drift cells filled with low-Z gas to minimize multiple scattering for better momentum resolution. The gas is ionized whenever a charged particle passes through, and the sense wire can pick up a signal. The Bethe-Bloch formula [60] describes the charged particle energy loss, which mainly depends on the velocity β. For a given momentum, the energy loss is different for different masses. The charged particles are identified through their masses, inferred from their momentum and energy loss measured in the CDC. Figure 2.7 shows a scatter plot of the measured dE/dx and momentum for different particles.

The transverse momentum p_t resolution of the tracking system consisting of the SVD and CDC sub-detectors is

$$\sigma_{p_t}/p_t = 0.0019 p_t \oplus 0.0030/\beta \tag{2.5}$$

, where the p_t is measured in GeV/c and $\oplus$ means sum in quadrature [57].

2.3.0.3 Aerogel Cerenkov counters

An array of silica-aerogel threshold Cerenkov counters is part of the Belle particle identification system, along with the dE/dx in the CDC and the time-of-the flight detector. The

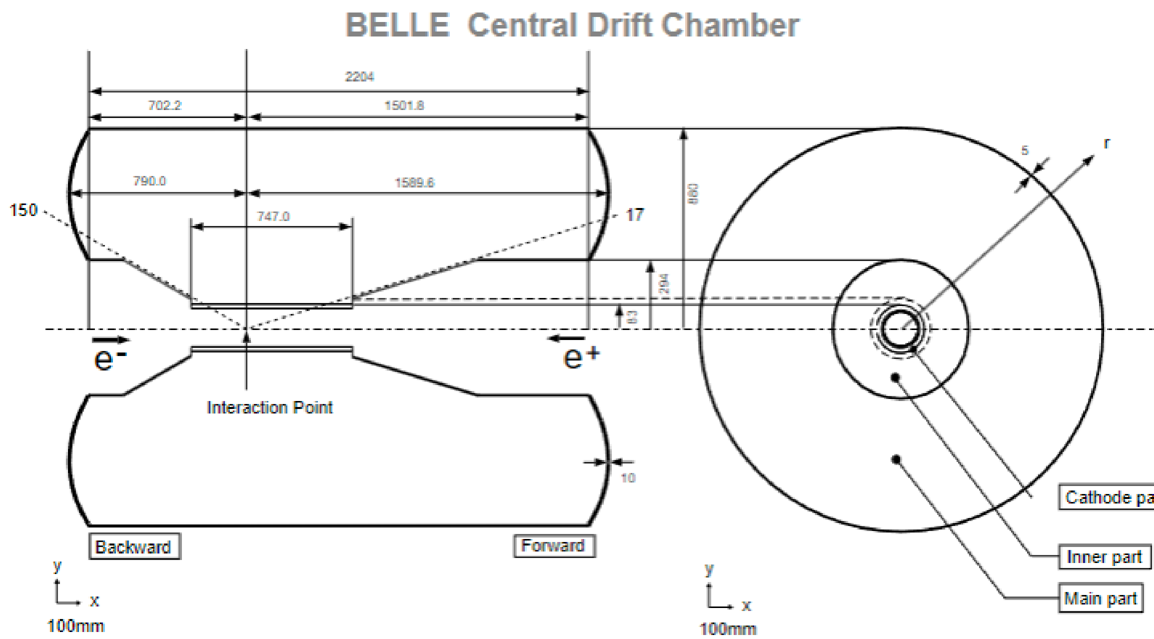

Figure 2.6: The CDC sub-detector overview [59].

Cerenkov radiation is emitted when a particle's speed is greater than the light in a matter

$$n > \frac{1}{\beta} = \sqrt{1 + (\frac{m}{p})^2} \tag{2.6}$$

where n is the refractive index of the matter. Thus, for a given index n, there is a momentum region where π can have Cerenkov radiations, but heavier particles like K do not. The set of index n is chosen to separate the π and K for the momentum regions of interest. Two (one) photo-multiplier tubes are attached to each module in the barrel (endcap) part to detect the Cerenkov light or photons.

Figure 2.8 shows the configuration of the Belle aerogel Cherenkov counter. The polar angle coverage is $33.3° < \theta < 127.9°$ in the barrel, and $13.6° < \theta < 33.4°$ in the forward endcap and allowing for efficient K-π separation in the momentum range between 1.5 GeV/c and 3.5 GeV/c. The ACC has 960 counter modules in total. The barrel device consists of 60 identical sectors in the ϕ direction, and 16 modules are arranged in each sector. The end cap device consists of 12 identical sectors in the ϕ direction, and each sector contains 19 modules, which are configured to have a 5-layer structure in the radial direction.

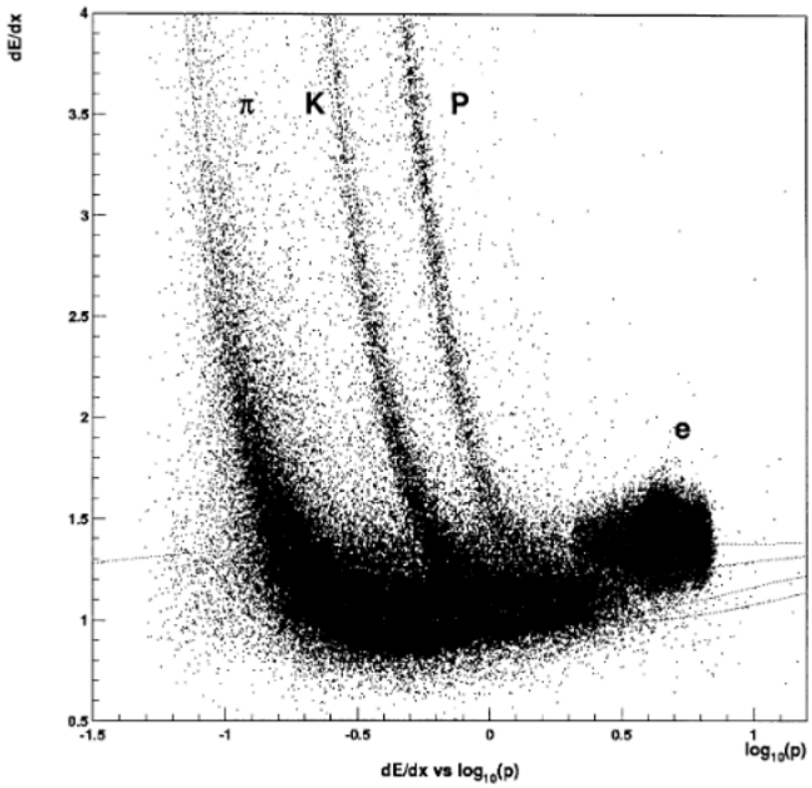

Figure 2.7: dE/dx measured in the CDC and momentum for different particles [58].

2.3.0.4 Time-of-flight system

The TOF measures the time of fight for charged tracks reconstructed by the CDC. The mass of a particle can be calculated from

$$T = \frac{L}{c\beta} = \frac{L}{c}\sqrt{1 + (\frac{m}{p})^2} \tag{2.7}$$

where L is the flight length.

The TOF is only installed in the barrel section of the detector outside the barrel section of ACC, as shown in Figure 2.8. The time-of-flight system can separate K and π for tracks with momenta below 1.2 GeV/c. The TOF is designed to have a time resolution of 100 ps for μ tracks. The TOF acceptance is $33^\circ < \theta < 121^\circ$ in the lab frame, and the minimum p_t to reach a TOF counter is 0.28 GeV/c.

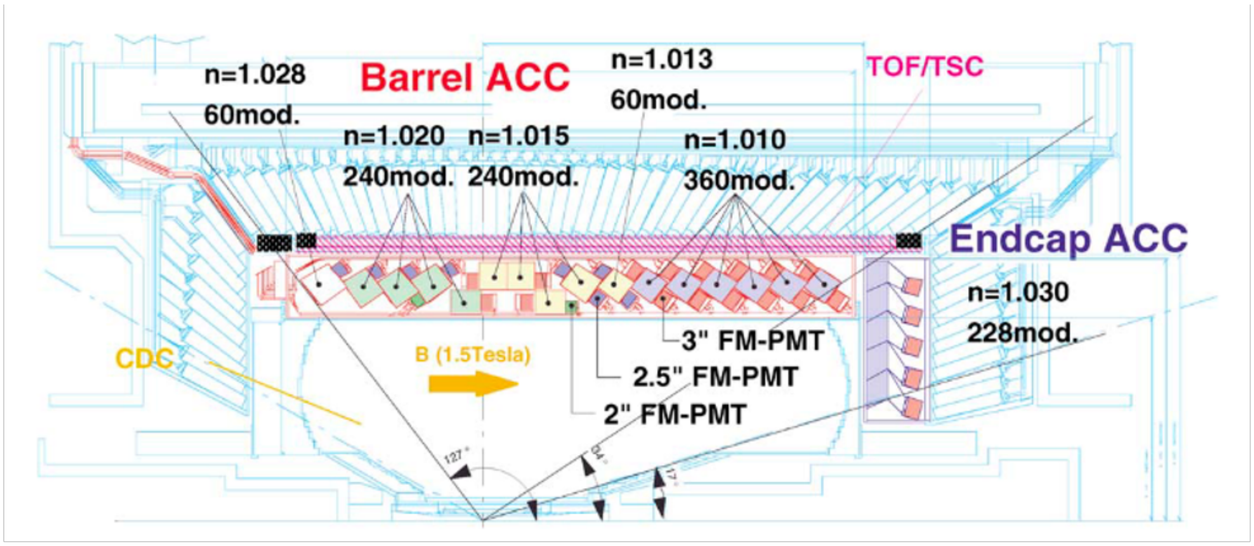

Figure 2.8: The ACC and TOF sub-detectors overview [58].

2.3.0.5 Electromagnetic calorimeter

The main objective of the ECL is to detect and measure photons with high efficiency and good resolutions in energy and position. The energy of an electron or photon is deposited in electromagnetic showers when it hits a crystal. The ratio E/p, the shower energy to the track momentum, is used for electron/hadron separation.

The overall configuration of the Belle electromagnetic calorimeter system is shown in Figure 2.9. The entire system contains 8736 CsI(Tl) crystals and weighs about 43 tons. The ECL consists of three sections: the forward endcap section has a polar angle coverage of $12.4° < \theta < 31.4°$, the barrel section coverage is $32.2° < \theta < 128.7°$, and the backward endcap coverage is $130.7° < \theta < 155.1°$. The ECL energy resolution varies from 4% at 100 MeV to about 1.6% at 8 GeV, and the angular resolution is about 13 mrad (3 mrad) at low (high) energies.

2.3.0.6 K_L^0 and μ detector

The KLM detection system is used to identify K_L^0 and μ with high efficiency for momenta greater than 600 MeV/c. Figure 2.10 shows the cross-section of a superlayer for the barrel region. The KLM consists of alternating glass electrode resistive-plate counters (RPCs) layers and 4.7 cm

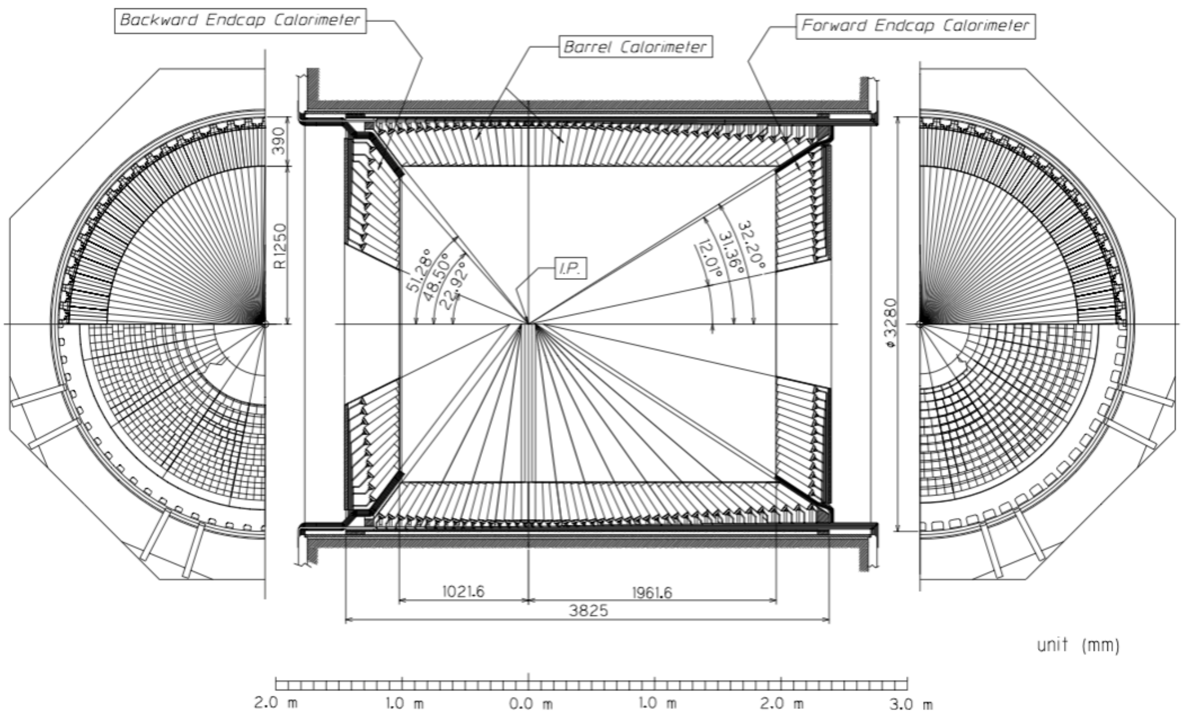

Figure 2.9: The ECL sub-detector overview [58].

thick iron plates. The KLM barrel polar angle coverage is $45^\circ < \theta < 125^\circ$, and the forward and backward end caps extend this range to between 20° and 155°. There are 15 detector layers and 14 iron layers in each octagonal barrel region and 14 detector layers and 14 iron layers in each endcap.

Hadrons interact with the iron plates and produce a shower of ionizing particles detected by the RPC layers. The cluster of hits is deposited in the KLM. A K_L^0 leaves a cluster in the KLM without an associated track in the CDC, which is distinguished from other charged hadrons. Muons in the KLM have a greater penetration depth than K_L^0 as they do not have strong interaction. The range and transverse direction of a non-showering charged particle discriminates between muons and K/π.

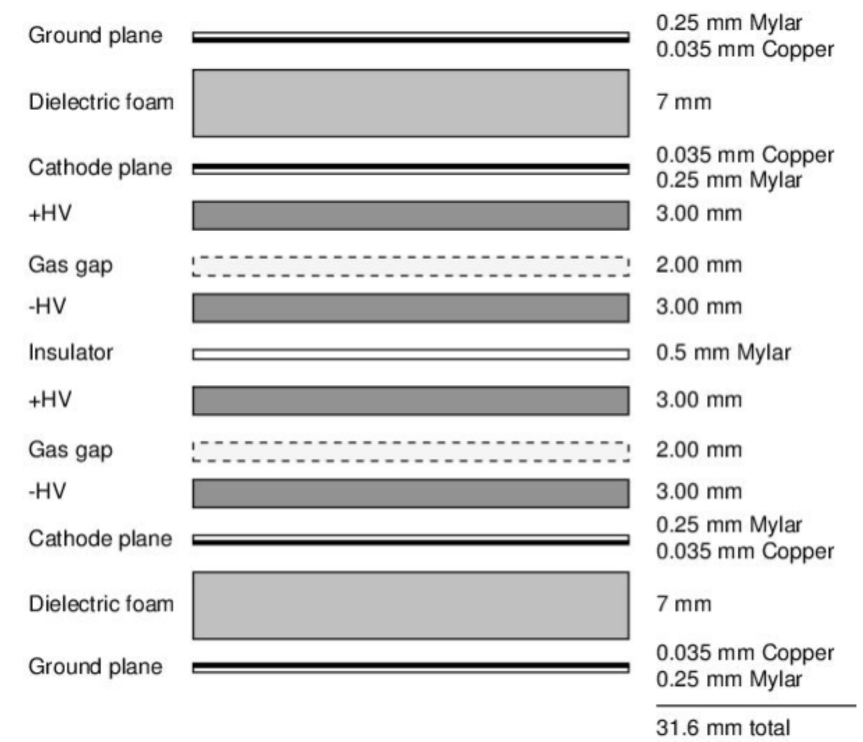

Figure 2.10: Cross section of a KLM superlayer [58].

CHAPTER 3. EVENT PRESELECTIONS

3.1 Analysis strategy overview

The D^0 production rate is not precisely known in the e^+e^- collisions. Therefore, the signal branching fractions and limits are calculated relative to a normalization mode. We use the decay $D^0 \to K^-\pi^+\pi^-\pi^+$ for normalization. The mode is well known, has a large branching fraction of $8.22 \pm 0.14\%$, and has the same number of tracks as the signal decays. The signal branching fractions are measured with respect to the decay $D^0 \to K^-\pi^+\pi^-\pi^+$ through the equation

$$\mathcal{B}(D^0 \to h^-h^{(\prime)+}e^+e^-) = \frac{N_{h^-h^{(\prime)+}e^+e^-}}{N_{K^-\pi^+\pi^-\pi^+}} \frac{\epsilon_{K^-\pi^+\pi^-\pi^+}}{\epsilon_{h^-h^{(\prime)+}e^+e^-}} \frac{\mathcal{L}_{K^-\pi^+\pi^-\pi^+}}{\mathcal{L}_{h^-h^{(\prime)+}e^+e^-}} \mathcal{B}(D^0 \to K^-\pi^+\pi^-\pi^+) \tag{3.1}$$

where N are the yields obtained from 1D fitting (details in Section 4.2), ϵ are the reconstruction efficiencies (details in Section 3.4.2) and $\mathcal{L}$ are the luminosities. To suppress combinatorial background from fake D^0, the signal D^0 is selected from the D^{*+} decay $D^{*+} \to D^0\pi_s^+$. Since the value of $\Delta m = (m_{D^*} - m_{D^0})$ is close to the m_{π^+}, the π_s^+ has a low momentum and is referred to as the soft or slow π. The Monte Carlo (MC) simulation is used in this analysis to study the signal and background distributions and determine the selection criteria. To avoid potential bias, which may unconsciously influence the research outcomes, the signal mode variable distributions are kept hidden until the selection has been finalized.

An overview of the data samples and the event selection are given in this chapter. The distributions of variables for signal and background and data and MC simulations of the decay channels in Sections 3.3.3 - 3.3.4. In the following chapters, the optimized selection criteria and the corresponding cut efficiencies are given in Chapter 3.4. The analysis results are given in Chapter 4, which includes the signal and normalization mode MC and data m_{D^0} distributions, the systematic uncertainties estimation, and the measured branching fractions and branching fraction upper limits. The conclusions are given in Chapter 5.

3.2 Data and MC samples

3.2.1 Data samples

The events collected by Belle are classified into several categories. The data are skimmed to produce subsets of selected events, designed for a specific area of analysis. The skimming is done by requiring the event passing a set of loose selection criteria, i.e., the number of tracks, the fraction of missing energy to the total energy, the tracks momenta and vertex positions. Using the skim helps analyzers efficiently analyze a specific amount of data based on the interest. For example, the QED processes $e^+e^- \to e^+e^-$ and $e^+e^- \to \mu^+\mu^-$ are used for detector calibration. Belle developed the hadronic skim `HadronB(J)` [57], which is used for analyses of B and charm mesons. The analysis is performed on a total of 942 fb^{-1} of $\Upsilon(4S)$ and $\Upsilon(5S)$ on and near resonance data, corresponding to about 583 millions of D^{*+} (D^{*-}). We use events selected by the `HadronB(J)` skim and analyze them using the `basf2` [61] framework developed by Belle II. Table 3.1 shows the integrated luminosity and number of events that pass the `HadronB(J)` skim criteria of the datasets with their corresponding center-of-mass energies.

Table 3.1: Integrated Luminosity (fb^{-1}) and number of events for `HadronB(J)` skim reprocessed data. The silicon vertex detector SVD1 was used for the first three years of data taking and then replaced by SVD2 (see details in Section 2.3.0.1).

Experiment	$E \sim m(\Upsilon(4S))$	$E \sim m(\Upsilon(5S))$	Total $\mathcal{L}$	No. of events after `HadronB(J)` skim
7-27 (SVD1)	140.747/15.621	0/0/0	156.099	628,939k
31-73 (SVD2)	562.615/73.833	121.061/1.73/27.574	786.889	3,186,011k
7-73 (Total)	702.623/89.454	121.061/1.73/27.574	942.462	3,814,950k

3.2.2 MC samples

Large samples of the processes $e^+e^- \to q\bar{q}$ ($q\bar{q} = u\bar{u}, d\bar{d}, s\bar{s}, c\bar{c}, b\bar{b}$) are centrally produced by Belle, called Belle generic MC-simulated events, are used for the studies of backgrounds. The events undergo fragmentation and hadronization to reproduce the known production rates and branching fractions obtained from PDG. Six streams [1] of Belle generic MC-simulated events are used to study the background for the rare D^0 signal modes. Only stream No.0 is used to study the efficiency and background of the $D^0 \to K^-\pi^+\pi^-\pi^+$ normalization mode. The numbers of simulated events for each event type in each stream are listed in Table 3.2. In order to study the $D^0 \to K^-\pi^+e^+e^-$, $D^0 \to \pi^-\pi^+e^+e^-$, and $D^0 \to K^-K^+e^+e^-$ in different m_{ee} mass regions, we use *EvtGen* [62] to generate the corresponding MC-simulated events of signal decays (Table 3.3). The number of generated samples processing through the skim is given in Table 3.4.

Table 3.2: Belle generic MC-simulated events.

Event type	Energy	$\mathcal{L}$ per stream [fb^{-1}]	No. events per stream
charged (B^+B^-) / mixed ($B^0\overline{B}^0$)	$m(\Upsilon(4S))$	692.5	377,426k
charm ($c\bar{c}$)	$m(\Upsilon(4S), \Upsilon(5S))$	911.1	1,184,484k
uds ($u\bar{u}$, $d\bar{d}$, $s\bar{s}$)	$m(\Upsilon(4S), \Upsilon(5S))$	911.1	1,904,275k
BsBs ($B^*_{(s)}\overline{B}^*_{(s)}$)	$m(\Upsilon(5S))$	122.4	7,133k
non-BsBs ($B^{(*)}\overline{B}^{(*)}, \Upsilon(4S)\gamma$)	$m(\Upsilon(5S))$	122.4	29,819k

[1] One stream corresponds approximately to the integrated luminosity of the full Belle dataset.

Table 3.3: Belle signal MC-simulated channels with e^+e^- final states. The PHSP represents the phase-space decay *EvtGen* mode where the MC-simulated events are generated with no intermediate resonance under kinematic constraints. The SVS represents the scalar to pseudoscalar and scalar decay mode. The VSS represents the vector to two pseudoscalar decay mode. The VLL represents the vector to two leptons decay mode. The SVV_HELAMP represents the scalar to two vector decays with generic helicity amplitude model.

m_{ee} regions [MeV/c^2] Modes	Excluding potential ee resonances	η $520 < m_{ee} < 560$	ρ^0 $675 < m_{ee} < 875$	ϕ $990 < m_{ee} < 1034$
$K^-K^+e^+e^-$	$D^0 \to K^-K^+e^+e^-$ PHSP	$D^0 \to \phi\eta$ SVS $\phi \to K^-K^+$ VSS $\eta \to e^-e^+$ PHSP	$D^0 \to \phi\rho^0$ SVV_HELAMP $\phi \to K^-K^+$ VSS $\rho^0 \to e^-e^+$ VLL	-
$\pi^-\pi^+e^+e^-$	$D^0 \to \pi^-\pi^+e^+e^-$ PHSP	$D^0 \to \pi^-\pi^+\eta$ PHSP $\eta \to e^-e^+$ PHSP	$D^0 \to \rho^0\rho^0$ PHSP $\rho^0 \to \pi^-\pi^+$ VSS $\rho^0 \to e^-e^+$ VLL	$D^0 \to \pi^-\pi^+\phi$ PHSP $\phi \to e^-e^+$ VLL
$K^-\pi^+e^+e^-$	$D^0 \to K^-\pi^+e^+e^-$ PHSP	$D^0 \to K^-\pi^+\eta$ PHSP $\eta \to e^-e^+$ PHSP	$D^0 \to \overline{K}^{*0}\rho^0$ SVV_HELAMP $\overline{K}^{*0} \to K^-\pi^+$ VSS $\rho^0 \to e^-e^+$ VLL	$D^0 \to K^-\pi^+\phi$ PHSP $\phi \to e^-e^+$ VLL

Table 3.4: Belle signal MC-simulated events generated in m_{ee} regions with corresponding *EvtGen* modes affect the decay angular distributions and selection efficiencies.

Modes $D^0 \to$	m_{ee} regions	Total No. events	No. events passed HadronB(J) skim	efficiency (%)
$K^-K^+e^+e^-$	phase-space	398,616	378,711	95.01 $\pm$ 0.03
	η	398,696	377,901	94.78 $\pm$ 0.04
	ρ/ω	398,511	377,296	94.68 $\pm$ 0.04
$\pi^-\pi^+e^+e^-$	phase-space	399,531	387,976	97.11 $\pm$ 0.03
	η	399,507	387,637	97.03 $\pm$ 0.03
	ρ/ω	399,367	388,389	97.25 $\pm$ 0.03
	ϕ	398,553	388,022	97.11 $\pm$ 0.03
$K^-\pi^+e^+e^-$	phase-space	399,198	384,391	96.29 $\pm$ 0.03
	η	399,243	384,858	96.40 $\pm$ 0.03
	ρ/ω	399,319	385,422	96.52 $\pm$ 0.03
	ϕ	399,187	383,740	96.13 $\pm$ 0.03

3.3 Preselections

3.3.1 Particle selections

In Belle, the sub-detector information from TOF, ACC, and CDC contributes to hadron identifications, i.e., the identifications of charged π and K. The electron identification is based on the sub-detector information from the CDC, ACC, and ECL. The particle identification (PID) in Belle is based on likelihood ratios. For hadron PID, the likelihoods for a candidate particle α are constructed from the information of CDC dE/dx L_α^{CDC}, time of flight from the TOF L_α^{TOF}, and the number of photons from ACC L_α^{ACC}. The likelihood ratios are [57]:

$$L(\alpha : \beta) = \frac{L_\alpha^{CDC} L_\alpha^{TOF} L_\alpha^{ACC}}{L_\alpha^{CDC} L_\alpha^{TOF} L_\alpha^{ACC} + L_\beta^{CDC} L_\beta^{TOF} L_\beta^{ACC}} \tag{3.2}$$

The likelihood L_α^{ECL} based on information from ECL like E/p, shower shape, and matching of the positions of the track and the energy cluster is used for electron identification besides the likelihoods from L_α^{CDC} and L_α^{ACC}. The information from KLM is used for the μ identification. The ΔR, representing the difference between the measured and expected range of the track from CDC, and the statistic χ_r^2, constructed from the transverse deviations of all hits associated with the track normalized by the number of hits, is used to form the L_α^{KLM}.

3.3.2 Preselections

We apply several loose selections to reduce the number of selected background events and the computation time. At least five charged tracks are required in the event, which greatly suppresses the background from QED processes. Each track must have momentum $p > 0.1$ GeV/c. The track transverse and longitudinal projection of the distance of the closest approach to the origin must be less than 0.25 cm and 4.5 cm to reduce beam-induced background and background from K_S^0 mesons. Tracks used to reconstruct $D^0 \to K^- K^+ e^+ e^-$, $\pi^-\pi^+e^+e^-$, and $K^-\pi^+e^+e^-$ candidates are required to pass loose PID criteria. No kaon ID (KID) $\mathcal{R}_K = \mathcal{L}_K/(\mathcal{L}_K + \mathcal{L}_\pi)$ requirement is imposed on pion or kaon candidates in the preselection. Electron candidates must have electron ID (eID) $\mathcal{R}_e = \mathcal{L}_e/(\mathcal{L}_e + \mathcal{L}_{non-e}) > 0.5$, where $\mathcal{L}_{non-e} = \mathcal{L}_\pi + \mathcal{L}_K + \mathcal{L}_p$. The electrons lose kinetic energy by radiating photons if they are deflected in the electric field of an atomic nucleus, which is a process called bremsstrahlung. The electron bremsstrahlung recovery is applied in this analysis, and photons having an angle within 5 degrees of an electron candidate and a minimum energy ($\min_{E(\gamma)}$) of 20 MeV are added to the four-momentum of electron candidate.

The D^0 signal candidates are reconstructed from the selected kaon, pion, and electron candidates. The mass of the D^0 candidate is calculated using the four momenta of the tracks. As an example, the D^0 candidate mass obtained from reconstruction of $D^0 \to K^-\pi^+e^+e^-$ decays are given by:

$$m_{D^0} = m(K^-\pi^+e^+e^-) = \sqrt{(p(E_{K^-}, \vec{p}_{K^-}) + p(E_{\pi^+}, \vec{p}_{\pi^+}) + p(E_{e^+}, \vec{p}_{e^+}) + p(E_{e^-}, \vec{p}_{e^-}))^2} \quad (3.3)$$

where the track momentum $\vec{p}$ is reconstructed from SVD and CDC. The reconstructed m_{D^0} will peak at the nominal D^0 mass ($\sim$1.865 GeV/c^2) if all the tracks from $D^0 \to h^-h^{(\prime)+}e^+e^-$ decay are correctly identified. For preselections, the D^0 candidates with m_{D^0} in the range 1.75 $< m_{D^0} < 1.98\,\text{GeV}/c^2$ are combined with each π^+ to form a D^{*+} ($m(D^{*+})$ $\sim$2.010 GeV/c^2) candidate [2]. Candidates must have a $D^{*+} - D^0$ mass difference Δm ($\sim$0.1454 GeV/c^2) consistent with the decay $D^{*+} \to D^0\pi_s^+$. A $\Delta m < 0.16$ GeV/c^2 cut is required for all three D^0 decay modes. Background from random track combinations at low D^{*+} momentum is reduced with a cut on the D^{*+} momentum in the center-of-mass frame at $p^*(D^{*+}) > 2.0\,\text{GeV}/c$, where p^* represents the momentum in the e^+e^- center-of-mass frame. Lastly, a vertex fit is applied to each reconstructed D^0 candidate. The χ^2 of the goodness of the vertex fit will be larger if the combined tracks are not originally from the same decay vertex. An interaction point constrained vertex fit to the decay chain $D^{*+} \to D^0\pi_s^+$, $D^0 \to h^-h^{(\prime)+}e^+e^-$ is applied, and candidates that fail the fit are discarded (Belle use negative $P(\chi^2_{D^{*+}})$ to represent the failed fit).

The electron bremsstrahlung recovery may mistakenly add the photons from $\pi^0/\eta \to e^+e^-\gamma$ decays. For example, if the electrons and photon from $D^0 \to K^-\pi^+\pi^0(e^+e^-\gamma)$ decays are picked, the reconstructed D^0 candidates will peak at 1.865 GeV/c^2 faking signal D^0 candidates. Additionally, the mass of D^0 candidates will peak at low m_{D^0} region if the $\pi^0/\eta \to e^+e^-\gamma$ decays

[2] The D^0 charge conjugated decay channels are also reconstructed in this analysis.

are partially reconstructed. To suppress the background from the $\pi^0/\eta \to e^+e^-\gamma$ decays, an $m_{ee} > 200$ MeV/c^2 cut is required for the signal modes [3]. This cut suppresses the low m_{ee} background from these decays as the γ is not reconstructed, as shown in Figure A.1 (in appendix) of the $D^0 \to K^-\pi^+e^+e^-$ mode m_{D^0} distributions distributions before and after the $m_{ee} > 200$ MeV/c^2 is applied. Because the Cabibbo favored decay $\mathcal{B}(D^0 \to K^-\pi^+\eta) \sim 1.88\%$ [2], an $m_{ee} > 560$ MeV/c^2 is applied to the non-resonant $K^-\pi^+e^+e^-$ region to reduce the $\eta \to e^+e^-\gamma$ background. The $m_{ee} > 560$ MeV/c^2 cut is also applied to the $K^-\pi^+e^+e^-$ mode after the preselection shown in Figure 3.1 (c).

The following two sections show the variable distributions obtained from generic MC and signal MC. The truth-matched [4] generic charm MC and generated signal MC m_{D^0}, Δm, and $p^*(D^{*+})$ variables are plotted as a cross-check for consistent shapes of the distributions (Section 3.3.3). To study the signal and background distributions and identify potential peaking background in the m_{D^0} region, the truth-matched signal MC and the generic MC variables after the preselection are plotted (Section 3.3.4).

3.3.3 Truth-matched MC distributions after preselections

Distributions of several variables after the preselection are shown (Figures 3.1 - 3.3) for the signal candidates in truth-matched phase-space signal MC ($\sim$400k events for each $h^-h^{(\prime)+}e^+e^-$ mode) and truth-matched generic charm MC (6 streams). The distributions of m_{D^0}, Δm, $p^*(D^{*+})$ obtained from the signal MC (red curve) are overlaid with the corresponding distributions generic charm MC (black curve). As expected, the shapes of the distributions agree between the generic charm MC and signal MC. However, there are fewer candidates in the generic charm MC, especially for the $K^-K^+e^+e^-$ modes.

[3] See details at Section 3.3.4.2 .

[4] The truth-matched candidates refers to the correctly reconstructed candidates (signal). The MC truth information is used to identify the correctly reconstructed candidates.

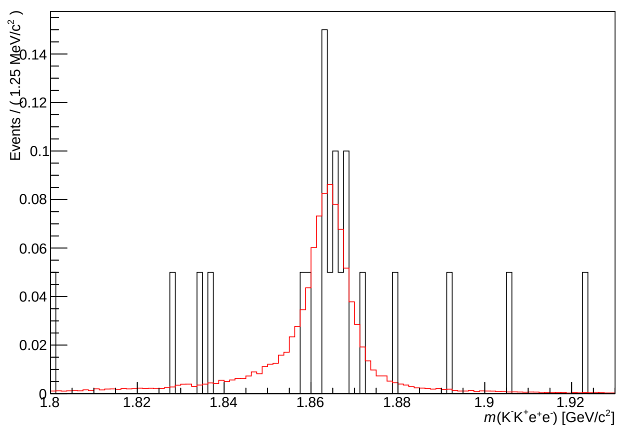

(a) $K^- K^+ e^+ e^-$

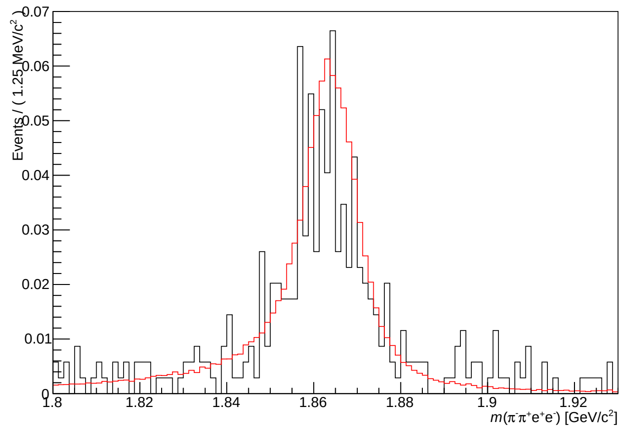

(b) $\pi^- \pi^+ e^+ e^-$

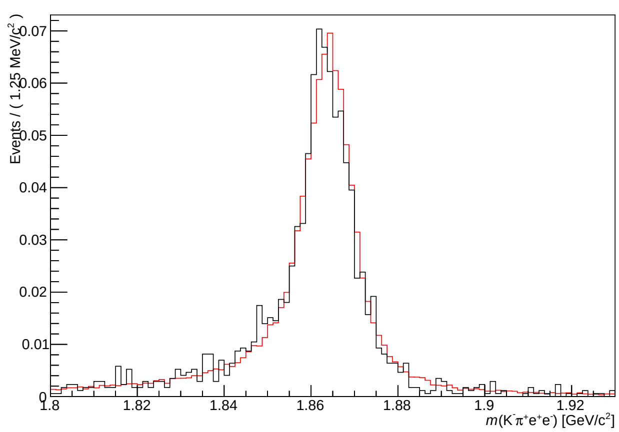

(c) $K^- \pi^+ e^+ e^-$

Figure 3.1: m_{D^0} distributions of truth-matched phase-space signal MC with truth-matched generic charm MC overlaid after preselections. Due to electron bremsstrahlung, the m_{D^0} signal distributions are asymmetric with a low-mass tail. The distributions are scaled to the unit area. The number of generic MC events in the plots for single Cabibbo suppressed decays is $D^0 \to K^- K^+ e^+ e^-$ (20 events) and $D^0 \to \pi^- \pi^+ e^+ e^-$ (230 events), resulting in large uncertainties. The $K^- \pi^+ e^+ e^-$ distribution from generic MC is shifted compared to the signal MC which is due to the $D^0 \to K^- \pi^+ \eta\,(\to e^+ e^- \gamma)$ background. The $m_{ee} > 560$ MeV/c^2 is applied to suppress it and the fitted signal probability density function (PDF) parameters (signal PDF functions are described in Section 4.2) are consistent.

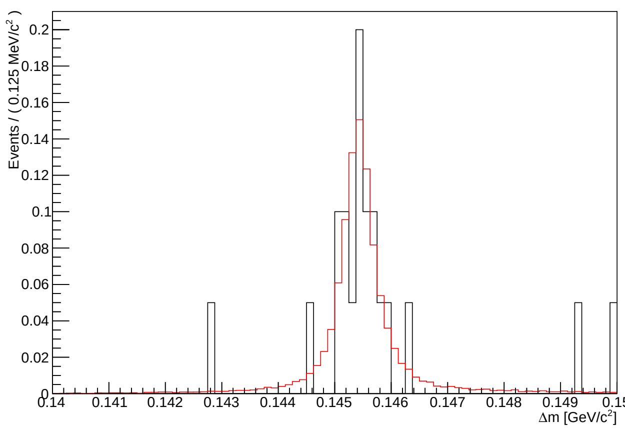

(a) $K^-K^+e^+e^-$

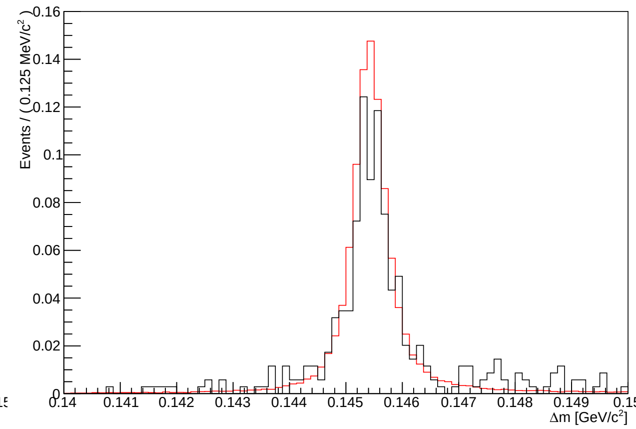

(b) $\pi^-\pi^+e^+e^-$

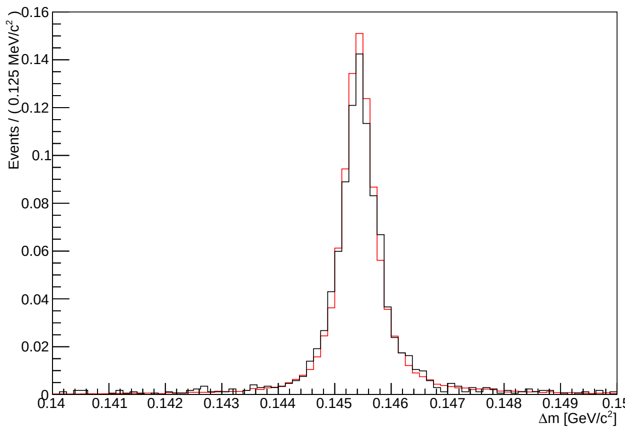

(c) $K^-\pi^+e^+e^-$

Figure 3.2: Δm distributions of truth-matched phase-space signal MC with truth-matched generic charm MC overlaid after preselection. The distributions are scaled to the unit area. The number of generic MC events in the plots for single Cabibbo suppressed decays is $D^0 \to K^-K^+e^+e^-$ (20 events) and $D^0 \to \pi^-\pi^+e^+e^-$ (230 events), resulting in large uncertainties. The fitted signal MC and generic charm MC Δm distributions are within the statistical uncertainty.

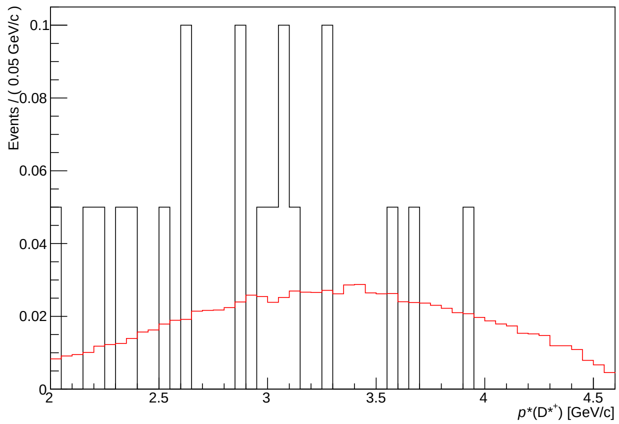

(a) $K^- K^+ e^+ e^-$

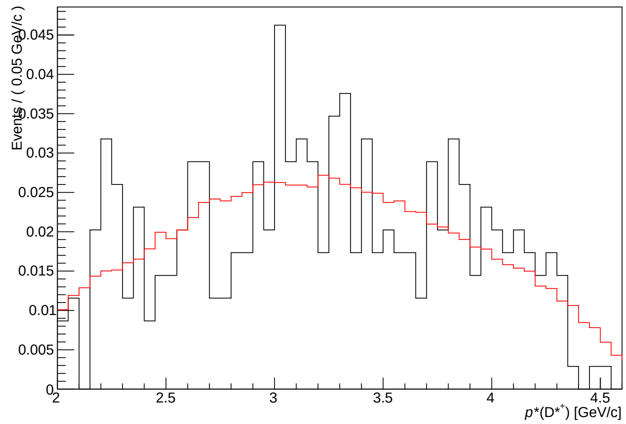

(b) $\pi^- \pi^+ e^+ e^-$

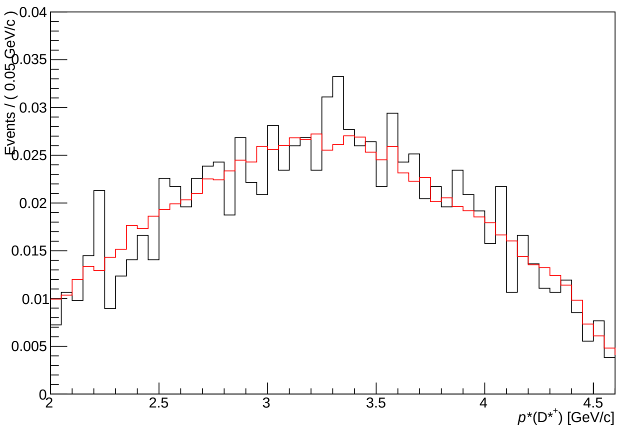

(c) $K^- \pi^+ e^+ e^-$

Figure 3.3: $p^*(D^{*+})$ distributions of truth-matched phase-space signal MC with truth-matched generic charm MC overlaid after preselection. The distributions are scaled to the unit area. The number of generic MC events in the plots for single Cabibbo suppressed decays is $D^0 \to K^- K^+ e^+ e^-$ (20 events) and $D^0 \to \pi^- \pi^+ e^+ e^-$ (230 events), resulting in large uncertainties.

The distributions of the PID variables for signal $D^0 \to K^- \pi^+ e^+ e^-$ (Figure 3.4) are given below using the corresponding phase-space signal MC. The PID responses of $D^0 \to \pi^+ \ \pi^- \ \eta \ [ee]$ are given in appendix A.1.1 for checking the PID distributions for the corresponding correct particles should populate close to one, whereas the others are not.

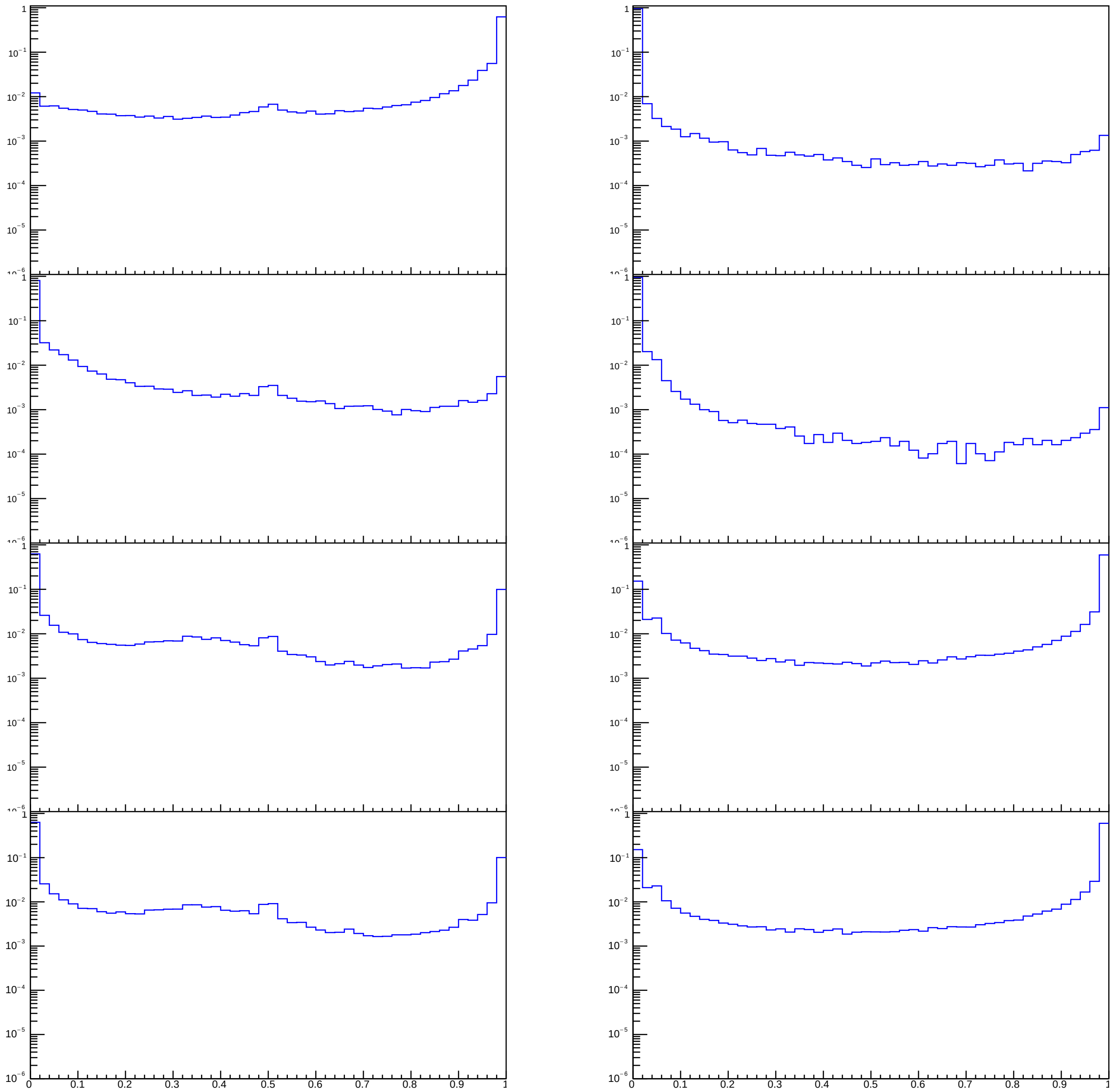

(a) KID (b) eID

Figure 3.4: $D^0 \to K^-\pi^+e^+e^-$ phase-space truth-matched signal MC PID responses. Each row gives the PID response for the four tracks from D^0 (from top to bottom: K^-, π^+, e^+, e^-). Each column gives the PID output for that track (left: KPID, right: e PID). The PID responses for the corresponding correct particle are populated close to one, whereas the others are not.

We first show the non-resonant signal modes $m_{hh^{(\prime)}}$ and m_{ee} distributions using truth-matched $D^0 \to K^-\pi^+e^+e^-$ phase-space signal MC as an example. Figures 3.5 give the $m_{K^-\pi^+}$ and m_{ee} distributions with m_{ee} in $m_{\rho/\omega}$ and mass regions with $\eta(520, 560)$, $\rho/\omega(675, 875)$, $\phi(990, 1034)[\,\mathrm{MeV}/c^2]$ excluded.

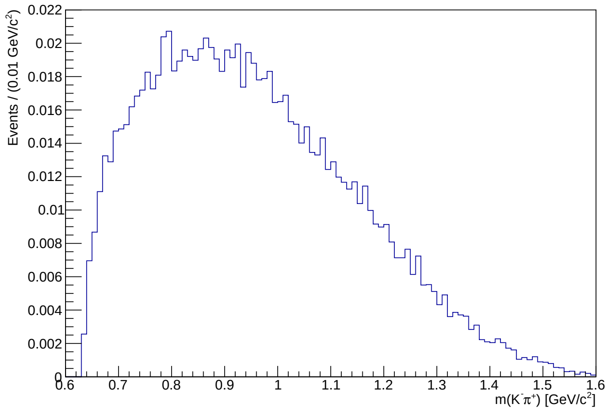

(a) $m_{K^-\pi^+}$

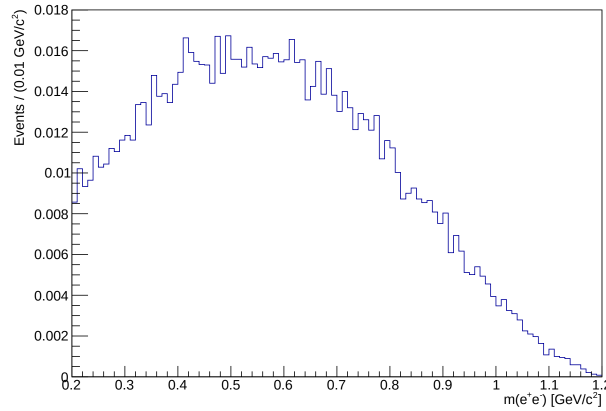

(b) m_{ee}

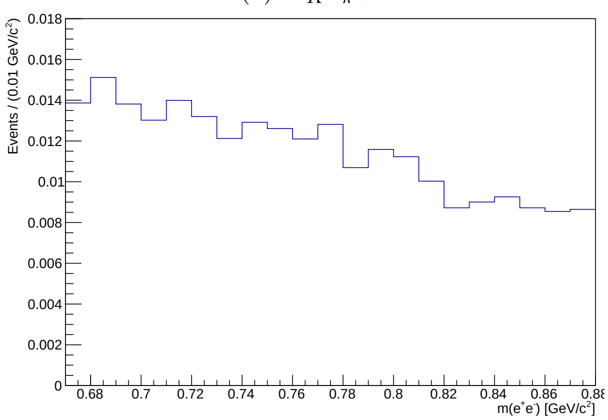

(c) $m_{ee} \in m(\rho/\omega)$

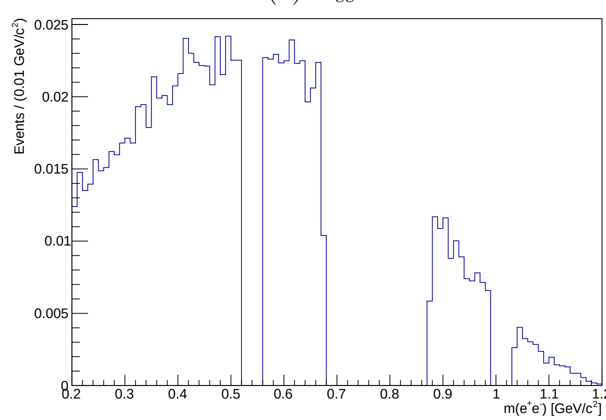

(d) $m_{ee} \notin m(\eta\,,\rho/\omega\,,\phi)$

Figure 3.5: Distributions of $m_{K^-\pi^+}$ and m_{ee} for truth-matched $D^0 \to K^-\pi^+e^+e^-$ phase-space decay signal MC. The distributions are scaled to the unit area.

The signal modes at the $hh^{(\prime)}$ and ee potential resonances are shown for checking the $D^0 \to h^- h^{(\prime)+} e^+ e^-$ resonance decay signal MC. We use the $D^0 \to K^{*0}$ $[K^-\pi^+]$ ρ^0 $[e^+e^-]$ signal MC as an example for showing the reconstructed $D^0 \to K^-\pi^+e^+e^-$ resonance decay candidates (truth-matched) $m_{K^-\pi^+}$ and m_{ee} distributions (Figure 3.6). In the appendix A.1.1 we give the m_{ee} distributions of ee at η and ϕ resonance regions using the $D^0 \to \pi^+$ π^- η/ϕ $[ee]$ signal MC as an example.

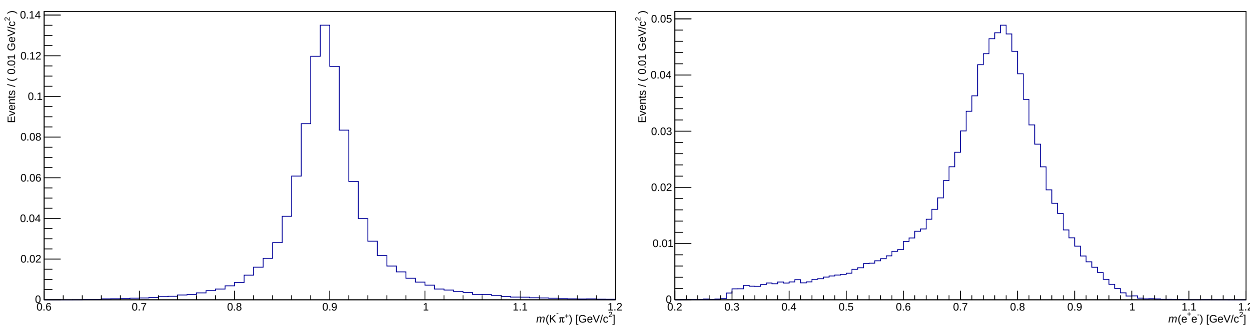

(a) $m_{K^-\pi^+}$

(b) m_{ee}

Figure 3.6: MC distributions of $m_{K^-\pi^+}$ (left) and m_{ee} (right) for truth-matched $D^0 \to K^{*0}$ $[K^-\pi^+]$ ρ^0 $[e^+e^-]$ events. The resonance peaks at the K^{*0} ($m(K^{*0}) \sim 0.895$ GeV/c^2 [2]) and ρ^0 ($m(\rho^0) \sim 0.775$ GeV/c^2 [2]) can be seen at $m_{K^-\pi^+} \sim 0.89$ GeV/c^2 and $m_{ee} \sim 0.78$ GeV/c^2, respectively. The natural widths (Γ) of the K^{*0} and ρ^0 are $\Gamma(K^{*0}) \sim 47$ MeV [2] and $\Gamma(\rho^0) \sim 147$ MeV [2], so their mass peaks are much wider than the D^0 ($\Gamma \sim \mathcal{O}(10^{-3})$ eV [2]) mass peak, which is limited by the detector resolution.

3.3.4 Generic MC distributions after preselections

The generic MC is used for studying the background and comparing it with the generated signal MC as a cross-check. Section 3.3.4.1 gives the generic MC background m_{D^0}, Δm, and $p^*(D^{*+})$ distributions with signal MC overlay. Section 3.3.4.2 gives the distributions of $m(hh)$, $m(ee)$, and PID outputs for signal modes from truth-matched generic MC.

3.3.4.1 Generic MC background distributions with signal MC overlay

The distributions of several variables for the signal (signal MC) and background (generic MC) are compared after preselection. We specifically check for potentially peaking background shapes near the signal regions in the distributions of m_{D^0} and Δm. The m_{D^0}, Δm, and $p^*(D^{*+})$ variable distributions are below in Figures 3.7 - 3.9.

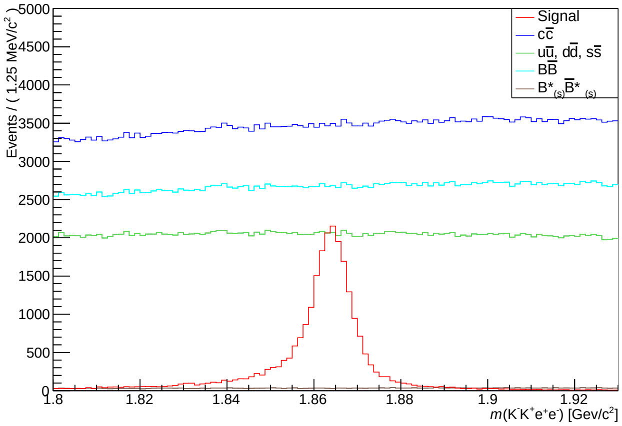

(a) $K^-K^+e^+e^-$

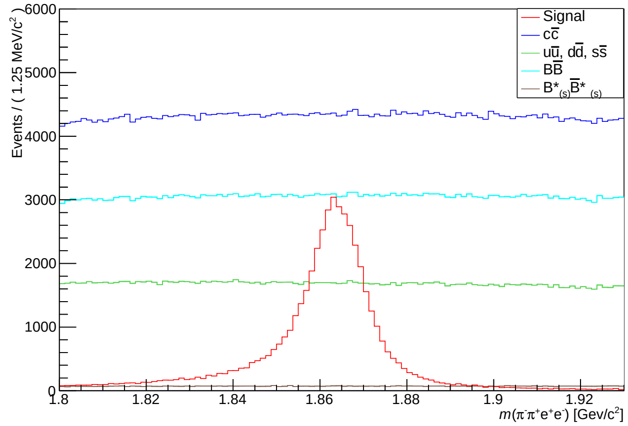

(b) $\pi^-\pi^+e^+e^-$

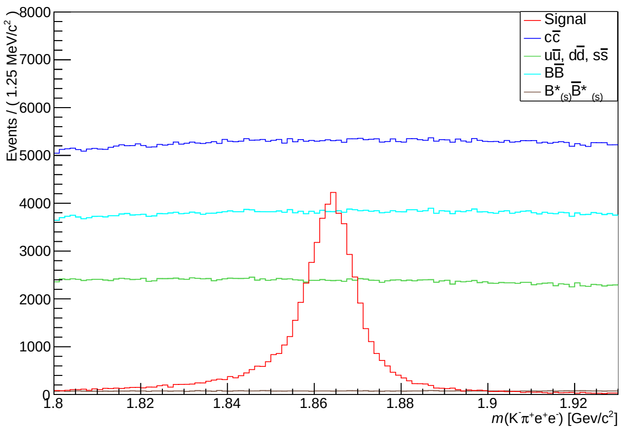

(c) $K^-\pi^+e^+e^-$

Figure 3.7: m_{D^0} distributions of generic MC background with truth-matched phase-space signal MC overlay after preselection. The distributions are obtained from six streams of generic MC and $\sim$ 400k signal MC, all scaled to data luminosity (same for the Δm and $p^*(D^{*+})$ distributions below). The signal (red) curves are scaled to 2000 times of data $\mathcal{L}$ for better visualization (also for the distributions below). The background from $B^*_{(s)}\ \overline{B}^*_{(s)}$ and $B^{(*)}\overline{B}^{(*)}X$ event samples are produced at e^+e^- center-of-mass energy of 10.89 GeV is negligible. The dominant background comes from the $B\overline{B}$ and "continuum" ($e^+e^- \to c\bar{c}, u\bar{u}, d\bar{d}$ and $s\bar{s}$) events. No peaking background is identified. The m_{D^0} signal distributions for the $h^-h^{(\prime)+}e^+e^-$ modes are asymmetric with a low-mass tail due to electron bremsstrahlung.

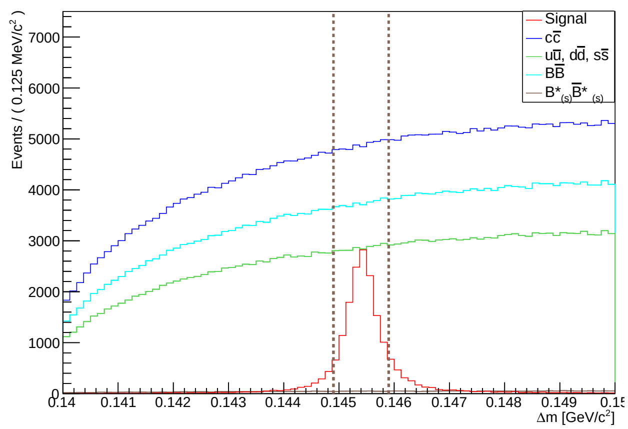

(a) $K^-K^+e^+e^-$

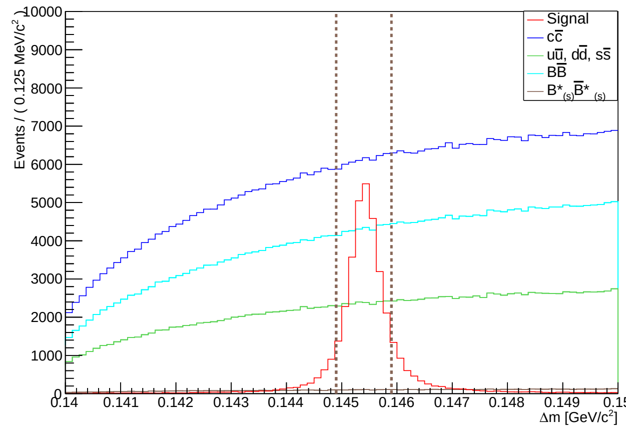

(b) $\pi^-\pi^+e^+e^-$

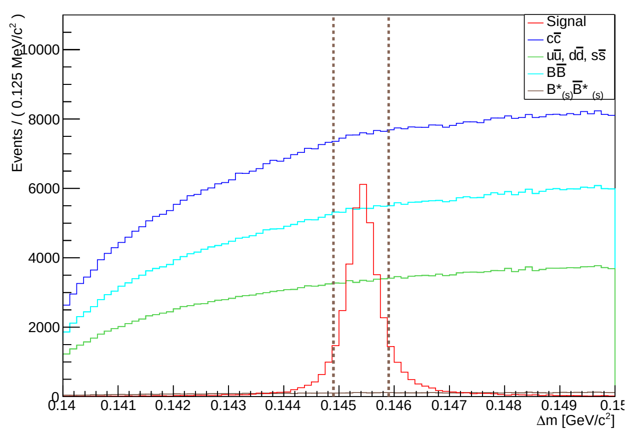

(c) $K^-\pi^+e^+e^-$

Figure 3.8: Δm distributions of generic MC background with truth-matched phase-space signal MC overlay after preselection. The distributions are obtained from six streams of generic MC and $\sim$ 400k signal MC, all scaled to data luminosity. The signal (red) curves are scaled to 2000 times of data $\mathcal{L}$ for better visualization. The $\Delta m(m_{D^{*+}} - m_{D^0})$ curves converge at 0.1396 GeV/c^2 which is the mass of $\pi^{\pm}$, because the each of the D^0 candidates are added with a π^+ candidate (π^+ mass is added to the track four-momentum) to reconstruct a D^{*+} candidate. The background from $B^*_{(s)}$ $\overline{B}^*_{(s)}$ and $B^{(*)}\overline{B}^{(*)}X$ event samples is negligible. The dominant background comes from the $B\overline{B}$ and "continuum" events. No peaking background is identified. The dashed lines indicate the final cut position (final selections discussed in Section 3.4).

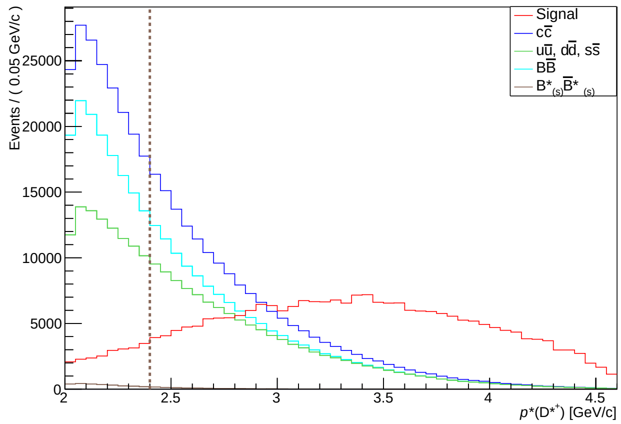

(a) $K^-K^+e^+e^-$

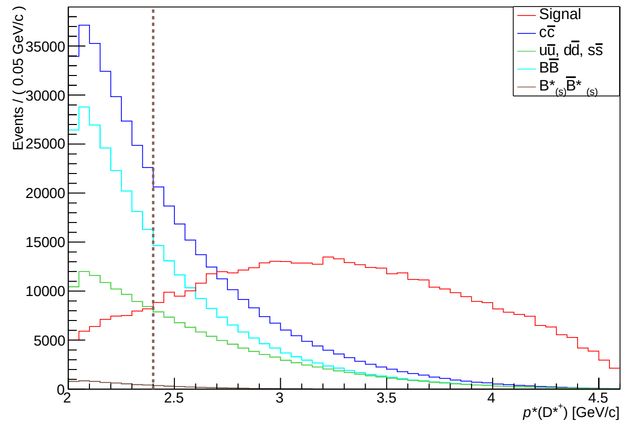

(b) $\pi^-\pi^+e^+e^-$

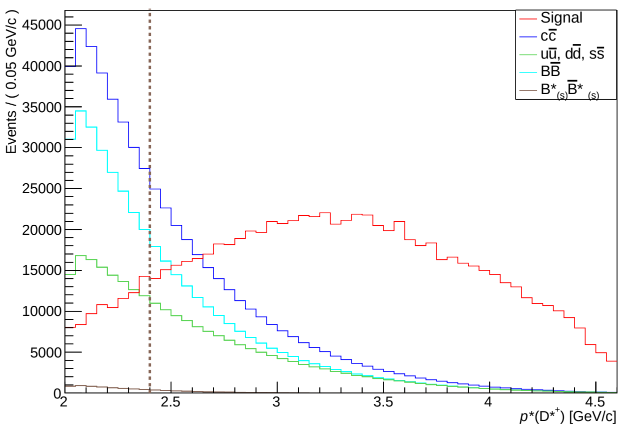

(c) $K^-\pi^+e^+e^-$

Figure 3.9: $p^*(D^{*+})$ distributions of generic MC background with truth-matched phase-space signal MC overlay after preselection. The distributions are obtained from six streams of generic MC and $\sim$ 400k signal MC, all scaled to data luminosity. The signal (red) curves are scaled to 2000 times of data $\mathcal{L}$ for better visualization. The $p^*(D^{*+})$ has a relatively larger value when D^{*+} is directly fragmented from a c quark, compared to coming from the b where firstly fragments to B then decays to D^*. The maximum value of $p^*(D^{*+})$ when D^{*+} fragmented from a c quark is around 4.9 GeV/c with e^+e^- center-of-mass energy at 10.6 GeV. The background D^{*+} peaks around 2 GeV/c. The background from $B^*_{(s)}$ $\overline{B}^*_{(s)}$ and $B^{(*)}\overline{B}^{(*)}X$ event samples is negligible. The dominant background comes from the $B\overline{B}$ and "continuum" events. The dashed lines indicate the cut position.

3.3.4.2 Generic MC truth-matched $D^0 \to K^-\pi^+e^+e^-$ distributions

Here, we check the potential $hh^{(\prime)}$ and ee resonances using the truth-matched generic MC for cross-checking the expected resonances for $K^{*0}(K^-\pi^+)$, $\rho^0(\pi^+\pi^+, e^+e^-)$, $\eta(e^+e^-\gamma)$ and $\phi(K^-K^+, e^+e^-)$. The peaks in the truth-matched generic MC m_{ee} and $m_{hh^{(\prime)}}$distributions are from the corresponding resonance decays generated from the Belle decay table. The distributions for the remaining modes are given in the appendix A.1.2 ($K^-K^+e^+e^-$: A.1.2.2, $\pi^-\pi^+e^+e^-$: A.1.2.3).

Besides the mass peak at $K^{*0} \sim 0.89\,\text{GeV}/c^2$ in the Figure 3.10 a, there is another peak at $\sim$1.6 GeV/c^2 from the decay $D^0 \to \rho^+ [\to \pi^+\pi^0(e^+e^-\gamma)]\, K^-$ and $D^0 \to K^{*-} [\to K^-\pi^0(e^+e^-\gamma)]\, \pi^+$. The distributions of so called helicity angle of vector decays to and a scalar and a vector (i.e. $D^0 \to K^{*-}[\to K^-\pi^0]\, \pi^+$) follows $\cos^2\theta$, where θ is the angle between the $\vec{p}(K)$ measured in the K^{*-} rest frame and $\vec{p}(K^{*-})$ measured in the D^0 rest frame. The $m_{K^-\pi^+}$ peaks occur when K and π have a small or large angle, as the preferred directions are either close to the mother particle or the opposite. The peak at low invariant mass region ($m_{ee} \sim 0$) is shown in Figure 3.10 b. (also contribute to the small bump ~ 0.2 GeV/c^2 in Figure 3.10 c) comes from the (partially) reconstructed $\pi^0 \to e^+e^-\gamma$ decays. The peaks at $\eta \sim 0.5\,\text{GeV}/c^2$ and $\rho/\omega \sim 0.78$ GeV/c^2 can be seen in Figure 3.10 c. The reconstructed η width is larger than the detector resolution (also $> \Gamma(\eta)$) due to the $\eta \to e^+e^-\gamma$ where the γ is not reconstructed.

As mentioned in the preselection, the $m_{ee} > 200\,\text{MeV}/c^2$ selection suppresses the photon pole mode and π^0 decays background. Additionally, for suppressing the $\eta \to e^+e^-\gamma$ decays, we do not apply bremsstrahlung recovery for m_{ee} in m_η region as described in the following Section 3.4. The PID responses are shown in appendix A.6 for checking the PID distributions for the corresponding correct particles should populate close to one, whereas the others are not.

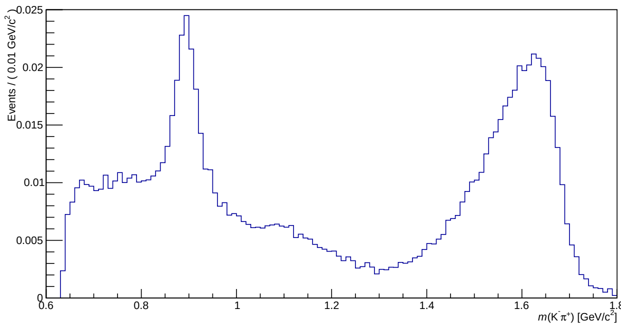

(a) $m_{K^-\pi^+}$

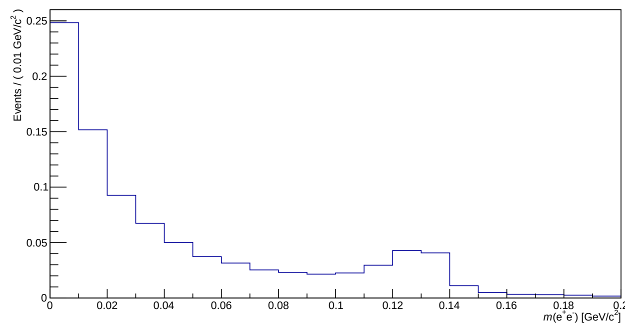

(b) m_{ee}

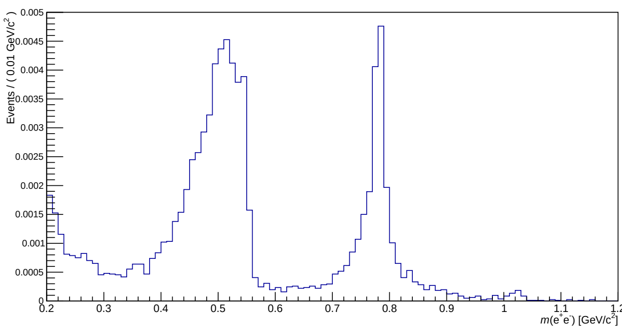

(c) m_{ee}

Figure 3.10: $D^0 \to K^-\pi^+e^+e^-$ (γ) truth-matched generic charm MC distribution. The distributions are scaled to the unit area, and the same is applied for the other signal modes shown in the appendix 11.2.1 - 11.2.2.

3.4 Optimized selections

New physics contributions are easier to detect in m_{ee} regions away from the resonances, where the predicted SM decay rate is small. In order to obtain the smallest possible upper limits on potential NP contributions, we optimize the selection criteria in the m_{ee} regions (combined to one m_{ee} mass region for each signal mode) excluding η, ρ/ω, and ϕ mass regions, and we call them non-resonant m_{ee} regions here. On the other hand, the cuts are optimized at η, ρ/ω, and ϕ mass regions [5] for each signal mode to search the potential ee resonance decays. The cuts are optimized based on the figure of merit (FOM) $\frac{S}{\sqrt{S+B}}$, where B is the background yield estimated from the generic MC samples, and S is the expected number of signal candidates in data estimated using signal MC. The final selections are based on the best significance obtained from the fit (described below in Section 4.2). The signal MC normalization factors are calculated based on the $\mathcal{B}$ from PDG, LHCb $K^-K^+\mu^+\mu^-$, and $\pi^-\pi^+\mu^+\mu^-$ results, under the assumption of lepton flavor university for the corresponding electron final states. For cross-checking, the *BABAR* measured $\mathcal{B}(K^-\pi^+e^+e^-$ with $m_{ee} \in m_{\rho/\omega})$ is $(4.0 \pm 0.6) \times 10^{-6}$ which is in agreement with the calculated $\mathcal{B}(4.6 \pm 0.2) \times 10^{-6}$ obtained from PDG [2] $\mathcal{B}(D^0 \to K^-\pi^+\rho^0 \times \rho^0 \to e^+e^- \times f +$ $D^0 \to K^-\pi^+\omega \times \omega \to e^+e^-)$, where potential $K^-\pi^+$ resonances are included and f is the fraction of the searched m_{ee} mass window ($675 < m_{ee} < 875$ MeV/c^2) to the ρ mass window. The $D^0 \to K^-\pi^+e^+e^-$ with $m_{ee} \in m_{\rho/\omega}$ FOM curves are given in appendix A.1.3 with the indication of optimized selections.

The additional selections beside the kinematic cuts applied to signal modes are described below (Section 3.4.1). The signal modes optimized selections for m_{ee} in the η, ρ/ω, ϕ and non-resonant m_{ee} mass regions[6] are given in Tables 3.5 - A.3. The normalization mode $D^0 \to K^-\pi^+\pi^-\pi^+$ selections are given in Table 3.5 (last column) and are set using the signal $K^-\pi^+e^+e^-$ mode optimized selections to minimize the systematics. The KID selection is the same for the signal modes $K^-\pi^+e^+e^-$, $K^-K^+e^+e^-$ and the normalization mode $K^-\pi^+\pi^-\pi^+$, so

[5] The m_{ee} mass window around the ρ/ω resonance is chosen as the same mass region as *BABAR*. For m_{ee} in the m_η and m_ϕ regions, the m_{ee} mass window is set to cover $\sim 85\%$ of the corresponding resonances regions.

[6] The optimized selections for m_{ee} in ρ/ω, ϕ and non-resonant m_{ee} regions are given in appendix A.1.4.

that the KID systematic uncertainty is expected to be fully (partially) canceled, assuming the K tracks have the same $(p, \cos\theta)$ distribution (See Section 4.5 for systematic uncertainties estimation). Appendix A.1.5 gives the background compositions after the final selections. The dominant background comes from the semi-leptonic B and D decays ($B/D \to X\, e\, \nu_e$).

3.4.1 Additional selections applied to signal modes

To further increase the sensitivity, additional selections are applied to address the background coming from a specific type of event. These backgrounds include photon conversions in the detector material (γ + nucleus $\to e^+e^-$ + nucleus), hadronic four-boday D^0 decays ($D^0 \to K^-\pi^+\pi^-\pi^+$, $K^+K^-\pi^-\pi^-$ and $\pi^+\pi^+\pi^-\pi^-$), and decays of $D^0 \to hh^{(\prime)}\eta/\pi^0(\to e^+e^-\gamma)$.

In some semileptonic $\overline{D} \to X$ decays the $\overline{D}$ daughters are combined with an e^+ from a photon conversion. The ee pair from photon conversion has an opening angle in the lab frame $\theta_{ee} \sim 0$ and $m_{ee} \sim 0$. We apply a photon conversion veto by picking the $e^\pm$ from the signal (D^0) candidate and another track with an opposite charge from the rest of the event to form a ee pair and discard the corresponding D^0 candidate based on the θ_{ee}, m_{ee}, and the two electron tracks vertex fit result. The distributions of these variables are given below in Figure 3.11.

The performance of photon conversion veto based on the selections optimized for m_{ee} in $m_{\rho/\omega}$ regions is studied. For the $K^-\pi^+e^+e^-$ mode, the photon conversion veto removes about 20 of 31 expected photon conversions[7] fall into the m_{D^0} and Δm fit region[8] at a negligible cost of signal events. The veto also rejects ∼13.2% of the remaining background (background not from photon conversion, i.e., combinatorial) compared to only applying other kinematic cuts. When applied to the $\pi^-\pi^+e^+e^-$ mode, the veto removes about 16 of 28 expected photon conversions and ∼7.1% of the remaining background. The signal mode efficiencies loss about 0.1% after the photon conversion veto.

Another background comes from hadronic D^0 decays where two or more of the D^0 daughters are misidentified. The pions from the hadronic D^0 decays can be misidentified as electrons so that

[7] The values are from counting with the help of truth-matching. This also applies to other vetoes mentioned below.
[8] Also apply to other veto mentioned below. $1.80 < m_{D^0} < 1.93$ GeV/c^2, $\Delta m < 0.15$ GeV/c^2.

the reconstructed m_{D^0} will peak in the low D^0 mass region. The $D^{*+} \to D^0\pi_s^+$ with $D^0 \to K^-\pi^+\pi^-\pi^+$, $D^0 \to \pi^+\pi^+\pi^-\pi^-$, and $D^0 \to K^+K^-\pi^-\pi^-$ decays are also reconstructed besides the signal $h^-h^{(\prime)+}e^+e^-$ modes reconstruction in each of the events. If a D^{*+} candidate in these modes with m_{D^0} and Δm have distances within the optimized threshold values to the corresponding nominal values is found, this signal candidate is discarded.

The performance of hadronic D^0 decays veto is studied based on the selections optimized for m_{ee} in $m_{\rho/\omega}$ regions. For the $K^-\pi^+e^+e^-$ mode, applying the hadronic D^0 decay veto after the photon conversion veto reduces the expected background contributed by hadronic D^0 decay from about 6 to 4 and also rejects $\sim 4.6\%$ of the remaining background (background other than hadronic D^0 decays) while maintaining the signal efficiency with a slight loss $\sim 0.1\%$. The veto reduces ~ 1.6 expected background events (~ 2 in total) and $\sim 15\%$ of the remaining background with a signal loss $\sim 0.3\%$ for the $\pi^-\pi^+e^+e^-$ mode. For the $K^-K^+e^+e^-$ mode, the veto reduces in total ~ 0.3 of the remaining background events (~ 3 in total) after applying photon conversion veto with a signal loss $\sim 0.5\%$.

The photons coming from the $D^0 \to hh^{(\prime)}\pi^0/\eta(\pi^0/\eta \to e^+e^-\gamma)$ decays can be misidentified as bremsstrahlung photons so that $D^0 \to h^-h^{(\prime)+}e^+e^-\gamma$ events are fully reconstructed (peaking in signal m_{D^0} region) faking signal $D^0 \to h^-h^{(\prime)+}e^+e^-$. On the other hand, picking the electrons from $\pi^0/\eta \to e^+e^-\gamma$ decay can also cause the m_{D^0} distribution peaking in the low m_{D^0} region when the γ is not added. To reduce the $\pi^0 \to e^+e^-\gamma$ background from the $D^0 \to hh^{(\prime)}\pi^0$ decays, a minimum of 200 MeV/c^2 is set for all the signal modes studied in different ee mass regions. To suppress the background from the $D^0 \to hh^{(\prime)}\eta\,(\to e^+e^-\gamma)$ decays, the electron bremsstrahlung recovery for m_{ee} in m_η region ($520 < m_{ee} < 560$ MeV/c^2) is not applied. A background PDF is used to fit (shown in Figure 4.1) the m_{D^0} peak in low m_{D^0} region originated from partially reconstructed $\eta \to e^-e^-\gamma$ decays. This background PDF is only used fitting the m_{D^0} distribution for the Caibbbo favored $D^0 \to K^-\pi^+e^+e^-$ with m_{ee} in m_η region, where no peaking background in the low m_{D^0} region found for the single Cabibbo suppressed $K^-K^+e^+e^-$ and $\pi^-\pi^+e^+e^-$ channels.

The number of reconstructed candidates in events with at least one signal candidate is approximately 1.01 for $K^-\pi^+e^+e^-$ and $K^-K^+e^+e^-$, and 1.02 for $\pi^-\pi^+e^+e^-$ with m_{ee} in $m_{\rho/\omega}$ region. For events with more than one signal candidate, the candidate with Δm closest to the nominal value is selected. The best candidate secection (BCS) efficiency ($\frac{\text{No. truth-matched events after BCS}}{\text{No. truth-matched events after final selection without BCS}}$) is $(81 \pm 7)\%$, studied from MC samples of $D^0 \to \overline{K}^{*0}\,(K^-\pi^+)\rho^0\,(e^+e^-)$ decays.

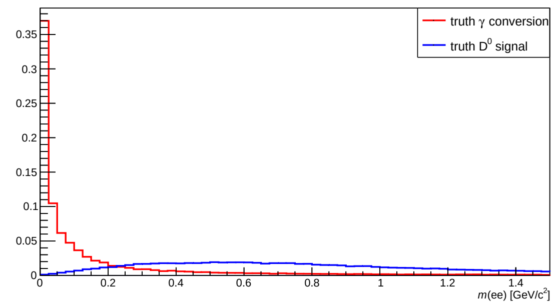

(a) m_{ee}

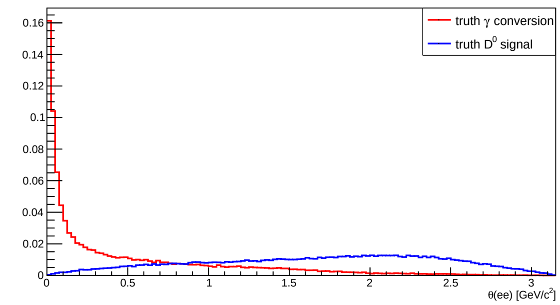

(b) θ_{ee}

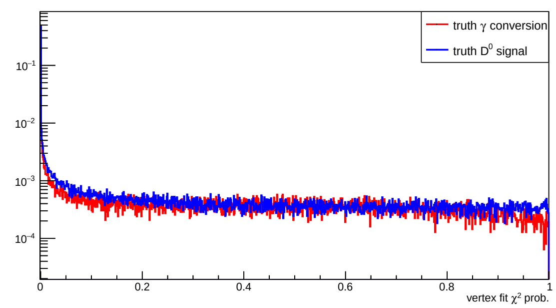

(c) $P(\chi^2_{\gamma^*})$

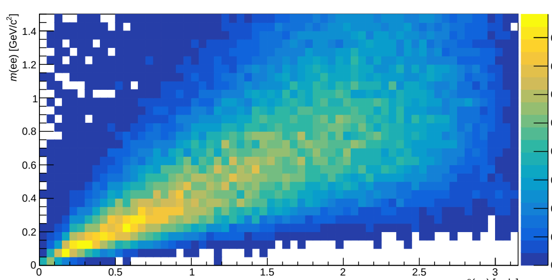

(d) Background m_{ee} vs θ_{ee}

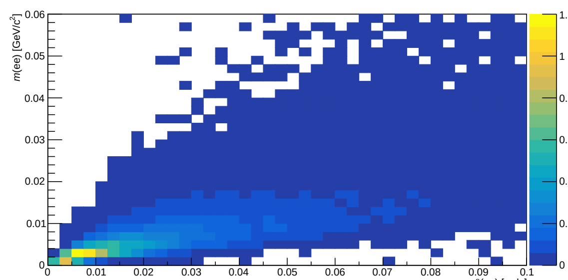

(e) Photon conversion m_{ee} vs θ_{ee}

Figure 3.11: The distributions of the two electron candidates invariant mass m_{ee}, the angle between them θ_{ee}, and their vertex fit χ^2 probability $P(\chi^2_\gamma)$. It can be seen from truth-matched generic MC-simulated events (red curve) that θ_{ee} and m_{ee} peaks near zero photon conversion. The blue curve represents the background where one of the e tracks comes from the truth-matched $D^0 \to K^-\pi^+e^+e^-$ signal MC-simulated events and the other from the tracks in the event that not used to reconstruct the $K^-\pi^+e^+e^-$. There is no apparent difference between the photon conversion and background in their vertex fit probability distributions. The candidates with failed fit are not chosen for photon conversion veto. For the θ_{ee} vs m_{ee} plot, the distribution peaks near zero for the photon conversion, and m_{ee} increases with θ_{ee} increases, as expected. The color bar in the correlation plots (Background m_{ee} vs θ_{ee}, Photon conversion m_{ee} vs θ_{ee}) is in percentage.

Table 3.5: Optimized selection criteria of signal modes for m_{ee} in η mass region ($520 < m_{ee} < 560$ MeV/c^2, $\delta(m_{D^0}) \equiv m_{D^0} - m_{D^0}^{\mathrm{PDG}}$, $\delta(\Delta m) \equiv \Delta m - \Delta m^{\mathrm{PDG}}$) and the selection criteria of normalization mode (last column). The normalization mode selections are set using the signal modes optimized selections to minimize the systematics.

Modes $D^0 \to$	$K^-\pi^+e^+e^-$	$K^-K^+e^+e^-$	$\pi^-\pi^+e^+e^-$	$K^-\pi^+\pi^-\pi^+$
Impact parameter selection:				
d_0 [cm]	< 0.25			
z_0 [cm]	< 4.5			
K selection:				
KID	> 0.1		-	> 0.1
eID	< 0.2		-	
π selection:				
KID	-		< 0.4	-
eID	< 0.2		< 0.1	-
e selection:				
p_e [GeV/c]	> 0.3	> 0.35	> 0.3	-
eID	> 0.9	> 0.8	> 0.9	-
$p^*(D^{*+})$ [GeV/c]	> 2.4		> 2.5	> 2.4
$P(\chi^2_{D^{*+}})$	> 0 (Converged fit)			
$\delta(\Delta m)$ [MeV/c^2]	< 0.5			
Photon conversion veto:				
$P(\chi^2_{\gamma^*})$	> 0			-
θ_{ee} [rads]	< 0.08 or	< 0.04 or		-
m_{ee} [GeV/c^2]	< 0.1	< 0.04		-
Hadronic D^0 decay veto:				
$P(\chi^2_{D^{*+}})$	> 0			-
$\delta(\Delta m)$ [MeV/c^2]	< 0.8			-
$\delta(m_{D^0})$ [MeV/c^2]	< 10			-
Best candidate selection:	closest to the nominal value of Δm			

3.4.2 Reconstruction efficiencies

The signal ($D^0 \to h^- h^{(\prime)+} e^+ e^-$) and normalization ($D^0 \to K^- \pi^+ \pi^- \pi^+$) channel reconstruction efficiencies are calculated from MC-simulated events. The signal yield is obtained from a 1D fit to m_{D^0} described by a Gaussian-like function with different left and right resolutions and tails (signal PDF function described in Section 4.2). The efficiencies obtained by counting the number of signal events are also studied for cross-checking. The mass of D^0 candidates can peak in the signal m_{D^0} region if the four tracks from the same $h^- h^{(\prime)+} e^+ e^-$ decays are used with wrongly assigned particle type, i.e. the swap of a pion and an electron track. Mis-reconstructed soft pion tracks added to D^0 candidates will pass the loose Δm selection and will peak in the signal m_{D^0} region if the D^0 candidate is correctly reconstructed. So multiple signal D^0 candidates will pass the preselection (no PID cut) in an event. As a result, the signal efficiencies obtained from fitting are larger than the truth-matched at the preselection stage. The signal efficiencies obtained from truth-matching and fitting are consistent after applying final selections.

The normalization mode $D^0 \to K^- \pi^+ \pi^- \pi^+$ efficiency after final selections with BCS of Δm is $(17.22 \pm 0.04)\%$, based on analyzing $\sim$ 4.3M D^{*+} tagged $D^0 \to K^- \pi^+ \pi^- \pi^+$ events. The $D^0 \to K^- \pi^+ \pi^- \pi^+$ events are identified using the `findMCdecay` module from the `basf2` [61] framework. For cross-checking, the efficiencies obtained by counting the number of truth-matched events give $(17.10 \pm 0.03)\%$.

Signal modes reconstruction efficiencies obtained using the resonance decay signal MC-simulated events (m_{ee} in m_η, $m_{\rho/\omega}$, m_ϕ regions) and phase-space signal MC-simulated events (for non-resonant m_{ee} regions) are given in Table 3.6.

Table 3.6: Signal modes efficiencies at different m_{ee} regions. The m_{ee} efficiencies in η, ρ/ω, and ϕ mass regions are obtained using the corresponding resonance signal MC-simulated events. (The efficiencies are $\epsilon = \frac{\text{No. yields after final selection}}{\text{No. events generated in } m_{ee} \text{ region}}$) [%]. The signal efficiencies of $K^-K^+e^+e^-$ channels in different m_{ee} regions are less than the corresponding $K^-\pi^+e^+e^-$ mode because $K\text{ID} > 0.1$ is applied to both of the K candidates resulting in relatively larger signal efficiencies loss, besides the larger branching fraction of the Cabibbo favored mode $K^-\pi^+e^+e^-$. More background populated in the low m_{ee} region because of low momentum tracks, the m_{ee} mass region cut is less effective when applying at low m_{ee} regions so that other tighter selections are needed (low signal efficiencies) to reach the same FOM compared to the high m_{ee} region.)

Modes $D^0 \to$	$K^-K^+e^+e^-$	$\pi^-\pi^+e^+e^-$	$K^-\pi^+e^+e^-$
η: $520 < m_{ee} < 560$	3.37 ± 0.04	5.31 ± 0.05	5.09 ± 0.05
ρ, ω: $675 < m_{ee} < 875$	6.00 ± 0.06	5.69 ± 0.05	8.01 ± 0.06
ϕ: $990 < m_{ee} < 1034$	-	9.41 ± 0.06	9.19 ± 0.06
Non-resonant: m_{ee} excluding η, ρ/ω, ϕ mass regions. $m_{ee} > 560$ MeV/c^2 is applied to the $K^-\pi^+e^+e^-$.	3.19 ± 0.04	3.69 ± 0.04	4.89 ± 0.09

CHAPTER 4. RESULTS

In this chapter, the statistical methods used for obtaining the results are introduced first in Section 4.1. The fit to m_{D^0} obtained from MC-simulated events and data are shown in Sections 4.2 and 4.4 for the signal channels, and Section 4.3 for the normalization mode. The systematic uncertainties are discussed in Section 4.5. The measured branching fractions and upper limits of the signal modes are given at last in Section 4.6.

4.1 Statistical interpretation

4.1.1 Unbinned maximum likelihood fit

Extended unbinned maximum likelihood fits to m_{D^0} distributions are used to extract the signal yields in this analysis. The purpose of the maximum likelihood method is to find the number of signal and background events in a given data sample that maximizes the likelihood functions defined as [63]:

$$\mathcal{L} = \frac{e^{-N}}{N!} \prod_{i=1}^{N} (N_{sig}\mathcal{P}_{sig} + N_{bkg}\mathcal{P}_{bkg}) \tag{4.1}$$

, where $N = N_{sig} + N_{bkg}$ is the number of total events, $N_{sig}(N_{bkg})$ is the number of signal (background) events, $\mathcal{P}_{sig}(\mathcal{P}_{bkg})$ is the signal (background) PDF, and they are defined in Section 4.2. The data fitting and yield extraction are performed through the RooFit framework [64].

4.1.2 Likelihood ratio based statistical test

In some experimental particle physics analysis one searches for the processes that have been predicted but have not seen. A general procedure used to such search is based on the frequentist approach. The frequentist approach begins by setting up a null hypothesis. For example, the null hypothesis is the background only model when searching for a signal. A test statistic $\tilde{t_{\mu}}$ is defined based on the profile likelihood ratio $\lambda(\mu)$. The test statistic is defined as [65]:

$$\tilde{t_{\mu}} = -2\ln\tilde{\lambda}(\mu) = \begin{cases} -2\ln\frac{L(\mu,\hat{\hat{\theta}}(\mu))}{L(\hat{\mu},\hat{\theta})}, & \text{when } \hat{\mu} \geq 0 \\ -2\ln\frac{L(\mu,\hat{\hat{\theta}}(\mu))}{L(0,\hat{\hat{\theta}})}, & \text{when } \hat{\mu} < 0 \end{cases} \tag{4.2}$$

, where μ is the parameter of interest, θ are one ore more nuisance parameters, $L(\mu, \hat{\hat{\theta}}(\mu))$ is the conditional maximized likelihood for a given value of parameter of interest (POI) μ with the corresponding nuisance parameter $\hat{\hat{\theta}}(\mu)$, and $\hat{\mu}$ and $\hat{\theta}$ are the values to maximize the likelihood $L(\hat{\mu}, \hat{\theta})$. The test statistic is reconstructed such that the higher the $\tilde{t_{\mu}}$ value, the larger the incompatibility between data and the hypothesis. When searching for a signal, the μ is set to zero, where the null hypothesis is the background only model. To quantify the level of agreement of the observed data with a given hypothesis, p-values are defined as [65]:

$$p_{\mu} = \int_{\tilde{t}_{\mu,obs}}^{\infty} f(\tilde{t_{\mu}}|\mu)\ d\tilde{t_{\mu}} \tag{4.3}$$

where $\tilde{t}_{\mu,obs}$ is the test statistic value observed from data, and $f(\tilde{t_{\mu}}|\mu)$ is the PDF of the test static for corresponding POI μ. The smaller the p-value is, the larger the inconsistency between the data and the hypothesis. For convenience, the p-value is usually converted into a significance Z defined as:

$$Z = \Phi^{-1}(1-p) \tag{4.4}$$

where Φ is the cumulative distribution of the standard Gaussian distribution. In high energy physics, the significance of $Z > 5\sigma$, corresponding to a p-value of $p < 2.8 \times 10^{-7}$, is required to claim a discovery. Strong evidence for a discovery requires significance to be greater than 3σ.

4.1.3 CL_s method

A branching fraction upper limit is set when there is no large deviation from the background only model, i.e., $Z < 3\sigma$. We use the CL_s method [65] to obtain the branching fraction upper limits. The CL_s p-values are given by:

$$p'_{\mu} = p_{\mu}/(1-p_0), \tag{4.5}$$

where the p_μ is the p-value of the signal plus background $(s + b)$ hypothesis under the parameter of interest μ and the p_0 is the p-value of the background only $(\mu = 0)$ hypothesis. The branching fraction upper limits at 90% confidence level (C.L.) are obtained. The upper limit at 90% C.L. is the largest μ where the $s + b$ hypothesis is not excluded. Toy MC experiments are generated to obtain the PDF of the test statistic described in 4.3. The RooStats framework is used to generate ~20k Toy MC experiments for each POI $N_{\text{signal}}\,(\mathcal{B})$ and obtain the p-values. The upper limit at 90% CL is obtained by finding the μ when $p'_\mu = 0.1$.

4.2 Fit to MC m_{D^0} distributions

Extended unbinned maximum likelihood fits are used to fit the m_{D^0} and Δm distributions for each mode in the various m_{ee} regions. The 1D fit to m_{D^0} is used to extract the signal yield, and the fit to the Δm (not optimized) is for reference to the m_{D^0} fit. The 400k signal MC-simulated events and six streams of generic MC-simulated events (for background) are scaled to the data luminosity and event weight is assigned to each D^0 candidates passing the final selections. The m_{D^0} signal PDF is a Gaussian-like function with different left and right resolutions $(\sigma_{L/R})$ and non-Gaussian tails $(\alpha_{L/R}(x - m_0)^2)$

$$f(x) = \begin{cases} exp(-(x-m_0)^2/(2\sigma_L^2 + \alpha_L(x-m_0)^2)), & \text{when } x < m_0 \\ exp(-(x-m_0)^2/(2\sigma_R^2 + \alpha_R(x-m_0)^2)), & \text{when } x > m_0 \end{cases} \tag{4.6}$$

The signal PDF parameters are obtained from the fits to the signal MC distributions (in appendix A.1.1.1) and then fixed for the signal yield extraction. The background is modeled using a linear function where its shape can float. The signal PDF of Δm distributions are two Gaussians with shared mean. The signal Δm PDF parameters are obtained from fitting to the signal MC $D^0 \to K^-\pi^+e^+e^-$. The signal modes m_{D^0} and Δm distributions are grouped by m_{ee} regions, and they are shown overlaid with the fit functions in Figures 4.1 - 4.7. The final event selections are determined based on the significance calculated using $Z = \sqrt{-2\Delta L}$, where ΔL is the change of the maximized likelihoods between signal yields allowed to float and fixed to zero.

The CL_s p-value plots for each m_{ee} region are shown in Figures 4.2 - 4.8. The estimated $\mathcal{B}$ and limits obtained from MC-simulated events calculated using equation 3.1 with statistical and systematic uncertainties included (details in Section 4.5) are given in Tables 4.1 and 4.2.

Table 4.1: Estimated signal channel branching fractions from MC-simulated events (The first uncertainty is statistical and the second is systematic. The systematic uncertainties are not included for the channels having much lower signal yield as the statistical error dominates) $[10^{-7}]$.

Modes $D^0 \to$	$K^-K^+e^+e^-$	$\pi^-\pi^+e^+e^-$	$K^-\pi^+e^+e^-$
η: $520 < m_{ee} < 560$	-0.1 ± 0.1	-0.6 ± 0.9	0.4 ± 1.3
ρ, ω: $675 < m_{ee} < 875$	1.3 ± 0.9	3.8 ± 2.4	41.6 ± 4.5
ϕ: $990 < m_{ee} < 1034$	-	4.1 ± 1.4	1.0 ± 0.7
m_{ee} exclude η, ρ/ω, ϕ mass regions	-0.5 ± 2.6	0.7 ± 3.1	0.5 ± 3.6

Table 4.2: Estimated signal channel branching fraction upper limits from MC $[10^{-7}]$.

Modes $D^0 \to$	$K^-K^+e^+e^-$	$\pi^-\pi^+e^+e^-$	$K^-\pi^+e^+e^-$
η: $520 < m_{ee} < 560$	< 2.1	< 3.1	< 5.3
ρ, ω: $675 < m_{ee} < 875$	< 2.2	< 7.0	
ϕ: $990 < m_{ee} < 1034$	-	< 4.5	< 2.4
m_{ee} exclude η, ρ/ω, ϕ mass regions	< 5.0	< 7.6	< 6.8

4.2.1 $\mathbf{520} < m_{ee} < \mathbf{560}$ MeV/c^2

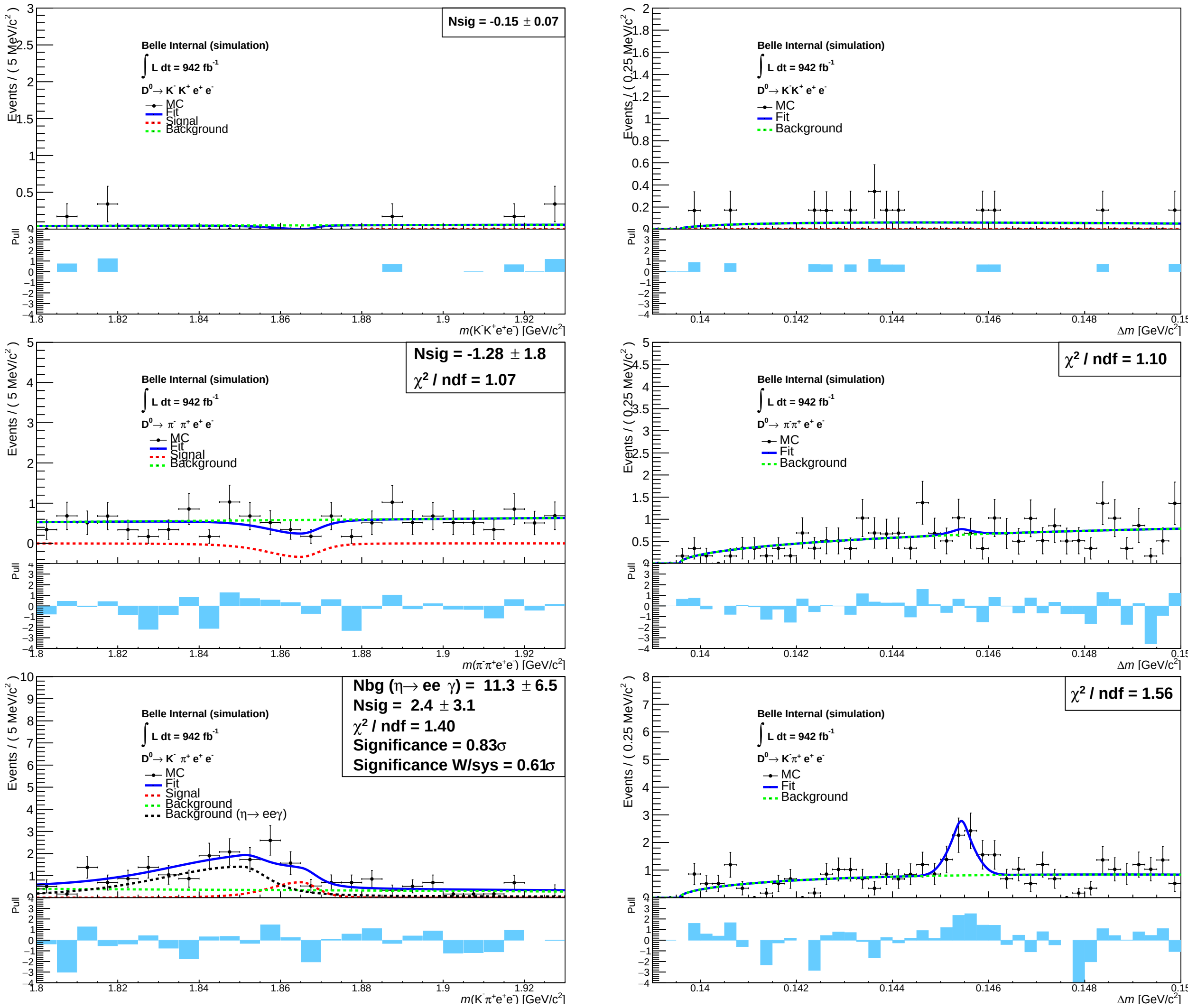

Figure 4.1: MC-simulated events of $D^0 \to h^- h^{(\prime)+} e^+ e^-$ m_{D^0} and Δm distributions with pull distributions ($520 < m_{ee} < 560$ MeV/c^2). The normalized residuals (pull) plots are shown underneath each plot, giving the fit quality. As can be seen, some of the bins have much larger uncertainty due to only a few signal MC-simulated events (event weight $<< 1$) falling into the corresponding region, resulting in a bin error of much less than 1. Such bins are removed when calculating the fitted χ^2. The m_{D^0} fit with tight Δm cut is used for the signal extraction. The Δm fit is for reference to the m_{D^0} fit and no significant amount of signal is expected among all three channels. The $\eta \to e^+ e^- \gamma$ decay background can be seen in the $D^0 \to K^- \pi^+ e^+ e^-$ m_{D^0} (black curve) and Δm distributions with a loose $1.85 < m_{D^0} < 1.88$ MeV/c^2 cut. The background m_{D^0} PDF parameters are fitted using generated $D^0 \to K^- \pi^+ \eta$ [$\to e^+ e^- \gamma$] MC while the γ is not reconstructed.

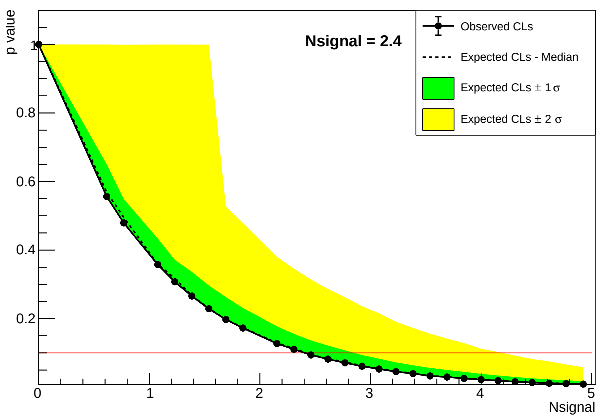

(a) $K^-K^+e^+e^-$

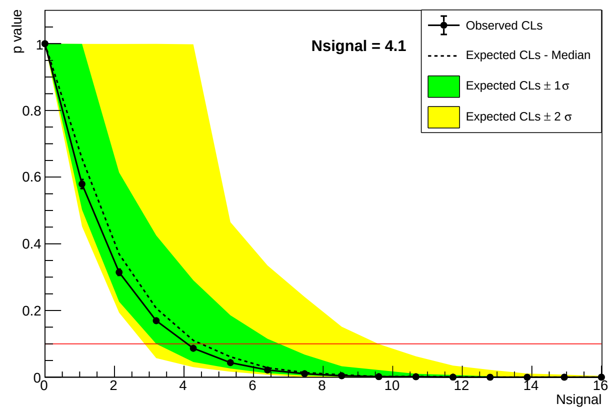

(b) $\pi^-\pi^+e^+e^-$

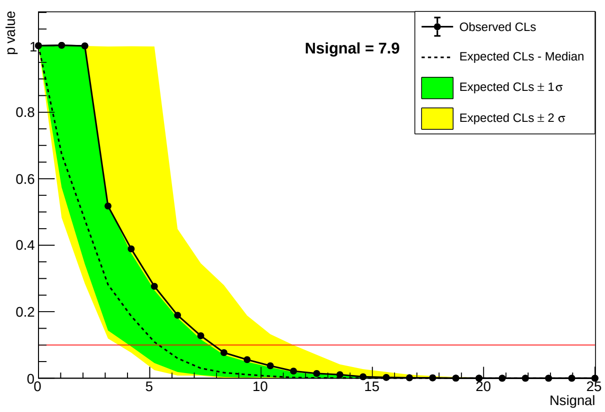

(c) $K^-\pi^+e^+e^-$

Figure 4.2: MC-simulated events of $D^0 \to h^-h^{(\prime)+}e^+e^-$ CL_s distribution ($520 < m_{ee} < 560$ MeV/c^2). The observed CL_s limits are obtained using the (signal + generic) MC-simulated events for the purpose of estimating the $\mathcal{B}$ upper limits for MC-simulated events. The N_{signal} upper limit is $N_{signal} < 2.4$ at 90 % C.L. for $D^0 \to K^-K^+e^+e^-$ ($520 < m_{ee} < 560$ MeV/c^2) channel. The expected CL_s limits are obtained from the background-only model, where the background yield is the median of the background sampling using Toy MC experiments. The unsmoothness is due to limited Toy MC generated to reduce the computation time, and a smooth curve can be obtained by generating more Toy MC experiments. The values are within the 2σ band of CL_s-expected, which suggests the background fluctuation. As expected, the signal yield upper limit becomes more conservative when the CL_s p-value decreases.

4.2.2 $675 < m_{ee} < 875$ MeV/c^2

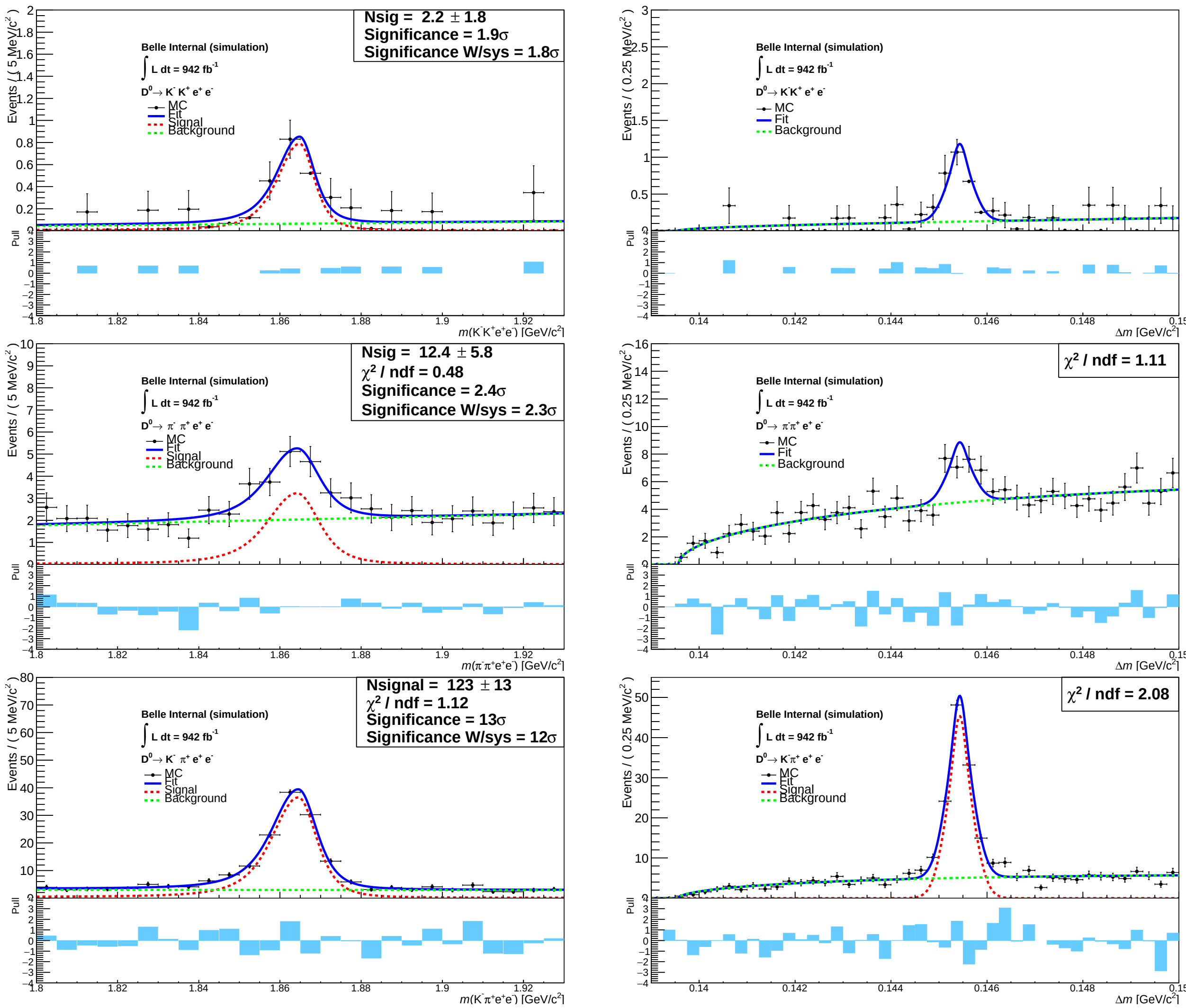

Figure 4.3: MC-simulated events of $D^0 \to h^- h^{(\prime)+} e^+ e^-$ m_{D^0} and Δm distributions ($675 < m_{ee} < 875$ MeV/c^2). The m_{D^0} fit with tight Δm cut is used for the signal extraction. The Δm fit is for reference to the m_{D^0} fit and a significance of 12σ is expected based on MC-simulated events for the $D^0 \to K^- \pi^+ e^+ e^-$ channel ($675 < m_{ee} < 875$ MeV/c^2).

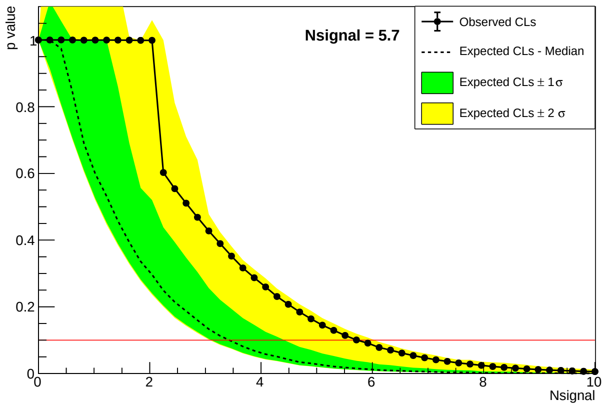

(a) $K^-K^+e^+e^-$

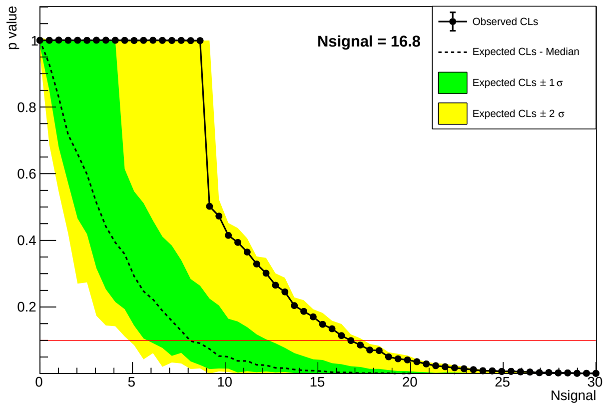

(b) $\pi^-\pi^+e^+e^-$

Figure 4.4: MC-simulated events of $D^0 \to h^-h^{(\prime)+}e^+e^-$ CL_s distribution ($675 < m_{ee} < 875$ MeV/c^2).

4.2.3 $990 < m_{ee} < 1034$ MeV/c^2

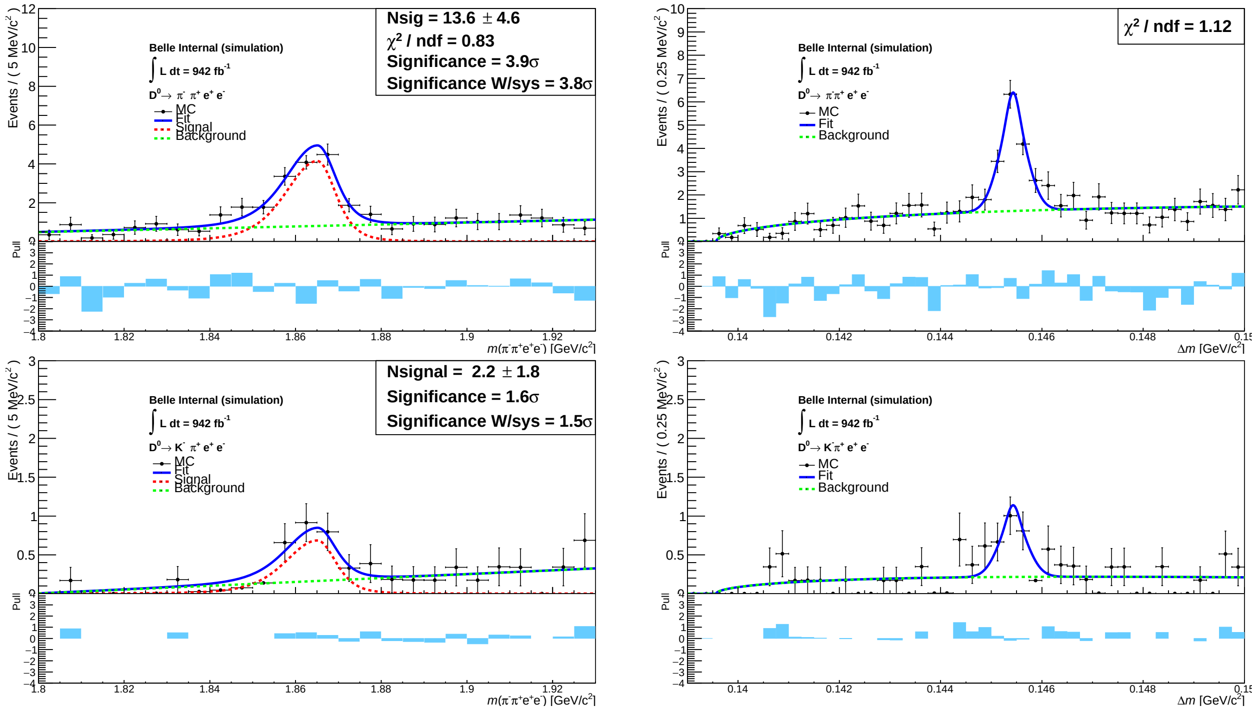

Figure 4.5: $D^0 \to h^- h^{(\prime)+} e^+ e^-$ m_{D^0} and Δm distributions ($990 < m_{ee} < 1034$ MeV/c^2). No $K^-K^+e^+e^-$ mode in this m_{ee} mass region because it is kinematically limited at 877 MeV/c^2 for the $K^-K^+e^+e^-$ channel. Over 3σ significance is expected based on MC-simulated events for the $D^0 \to \pi^-\pi^+e^+e^-$ channel ($995 < m_{ee} < 1035$ MeV/c^2).

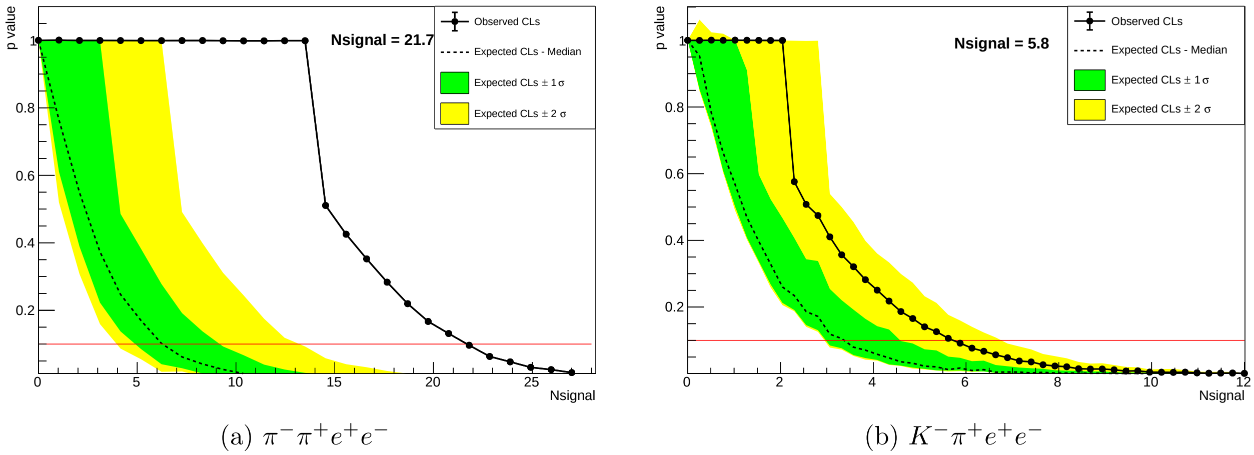

Figure 4.6: MC-simulated events of $D^0 \to h^- h^{(\prime)+} e^+ e^-$ CL_s distribution ($990 < m_{ee} < 1034$ MeV/c^2). The estimated significance from MC reaches 3σ for the $\pi^-\pi^+e^+e^-$ channel ($995 < m_{ee} < 1035$ MeV/c^2).

4.2.4 m_{ee} non-resonant region

For each signal mode we search one m_{ee} non-resonant region which is the m_{ee} regions excluding η, ρ/ω, and ϕ mass regions. The signal modes with ee resonant decays can leak into the signal non-resonant region due to the large natural width of the corresponding ee resonance, for example, the ρ resonance, which leaks to non-resonant m_{ee} region, because of its larger width than η, ω and ϕ. The expected potential resonant decay yields are estimated through $N_{D^0} \times \mathcal{B}(D^0 \rightarrow hh^{(\prime)}X) \times f$, where N_{D^0} is total number of D^0 calculated by dividing the fitted normalization mode ($K^-\pi^+\pi^-\pi^+$) yields by the normalization yield efficiency and PDG $\mathcal{B}(D^0 \rightarrow K^-\pi^+\pi^-\pi^+)$ [2], and f is the number of corresponding resonant decay signal MC passed the final selection divided by the total number of resonant signal MC generated. The total $\mathcal{B}$ (including potential $hh^{(\prime)}$ resonances) of decays $D^0 \rightarrow hh^{(\prime)}X\,[ee]$ where X is η, $\rho, \omega,$ andϕ are obtained from the PDG [2].

The signal ee resonant decays leak to other resonances as treated as systematic uncertainty. The dominant resonant decays background is from the $D^0 \rightarrow hh^{(\prime)}\rho^0$ decays[1]. As shown in the m_{D^0} distribution below, besides the signal PDF used to extract the signal yields , there is another PDF with parameters same as the signal PDF and fixed yields is used for fitting the ρ resonance decay leaks to the non-resonant region. The $D^0 \rightarrow K^-K^+e^+e^-$ mode resonant decays background is not separately fitted as its expected yield is much less than one event, and its expected value is accounted for a systematic uncertainty (Section 4.5).

[1]Other resonant decays background expected yield is negligible compared to other systematic uncertainties discussed in Section 4.5

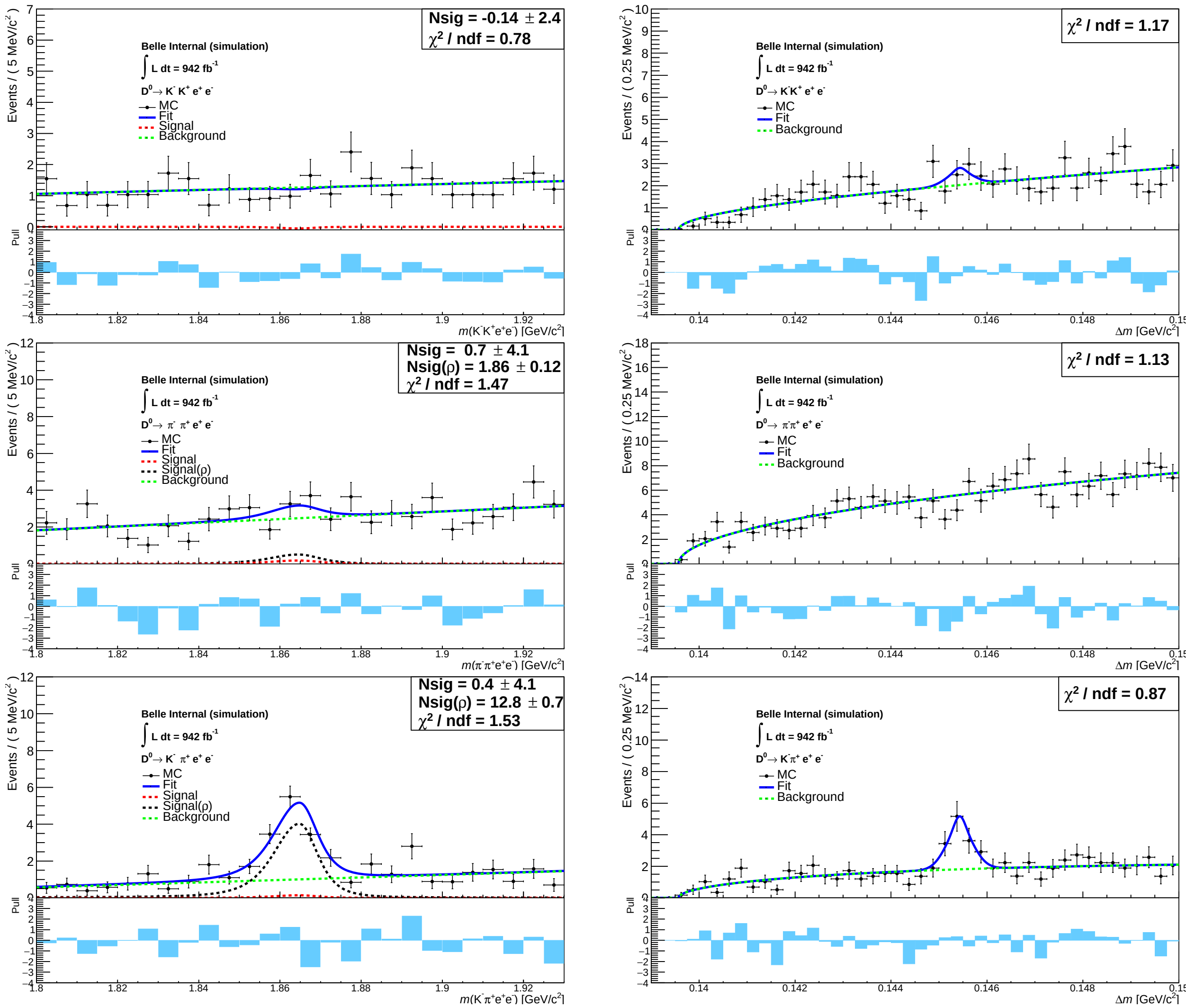

Figure 4.7: $D^0 \to h^- h^{(\prime)+} e^+ e^-$ m_{D^0} and Δm distributions (m_{ee} non-resonant regions. $m_{ee} > 560$ MeV/c^2 applied to $K^-\pi^+e^+e^-$ mode for removing $\eta \to e^+e^-\gamma$ background). The ρ resonance dominated Cabibbo favored resonance decay $D^0 \to K^-\pi^+e^+e^-$ background (black curve in m_{D^0} distribution) is separately indicated with fixed shape (same as the signal) and yields to distinguish from the signal phase-space decay (red curve).

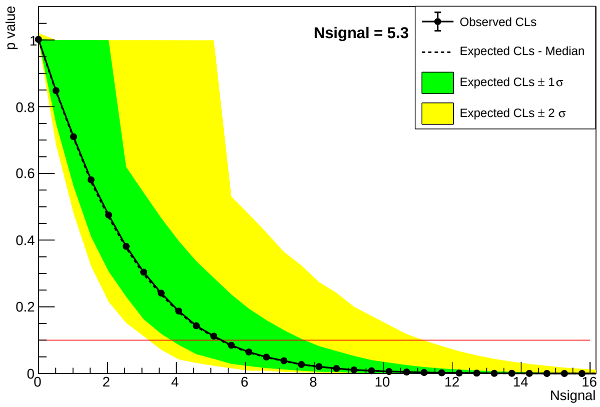

(a) $K^-K^+e^+e^-$

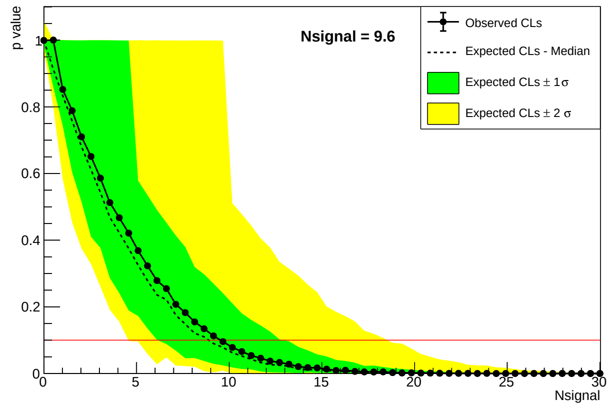

(b) $\pi^-\pi^+e^+e^-$

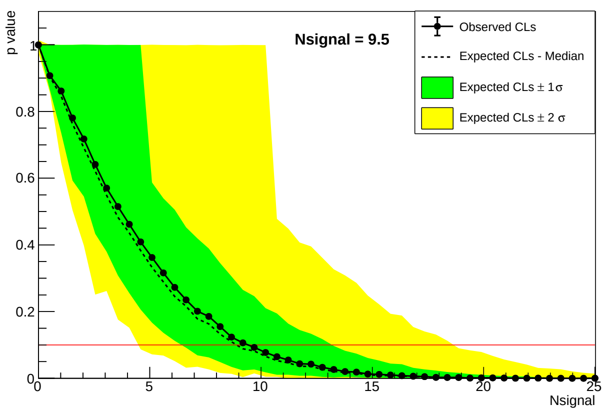

(c) $K^-\pi^+e^+e^-$

Figure 4.8: $D^0 \to h^-h^{(\prime)+}e^+e^-$ CLs distribution (m_{ee} excluding π^0, η, ρ/ω, ϕ mass regions).

4.3 Fit to normalization mode data and MC m_{D^0} distributions

We obtain the normalization channel yield by applying the same extended unbinned likelihood fit to the m_{D^0} distribution of the selected $D^0 \to K^-\pi^+\pi^-\pi^+$ events. The normalization mode Δm fit is given as a reference. The signal m_{D^0} distribution is fitted using a Gaussian like function (same as the signal modes') plus a Gaussian function where the m_{D^0} mean is shared, and the fit PDF for the data signal m_{D^0} distribution is selected by the goodness of fit (small χ^2/ndf). The signal Δm distribution is fitted using a double Gaussian with a shared Δm mean. The background is modeled using a linear function for the m_{D^0} distribution and a threshold function for the Δm. Figure 4.9 shows the fitted PDF parameters and yields from generic MC and data for the m_{D^0} and Δm distributions. The fit resolutions are the calculated weighted Root Mean Square Error using fitted resolutions from double Gaussian signal PDF. The data m_{D^0} resolution is ~ 5.9 MeV/c^2 and ~ 5.7 MeV/c^2 for MC-simulated events. The data Δm resolution is ~ 0.37 MeV/c^2 and ~ 0.35 MeV/c^2 for MC-simulated events. Table 4.3 gives a summary of MC/data fitted yield and relative difference ($\frac{\text{No. MC - No. data}}{\text{No.data}}$).

Table 4.3: $D^0 \to K^-\pi^+\pi^-\pi^+$ decay MC-simulated events and data fitted yields comparison. The top two rows are fitted signal yields where the bottom two rows are the fitted background yields. Given that the m_{D^0} background is much suppressed after the best candidate selection, a fluctuation in signal yields will result in a large relative MC-simulated events and data background difference. The MC-simulated background events are not trivial to simulate, and the background events are not used for $\mathcal{B}$ or $\mathcal{B}$ UL calculations. The MC-simulated events and data normalization mode yield difference is $\sim 4.6\%$ and the MC-simulated events and data are in good agreement without considering the systematic uncertainties. This difference has minimal impact on the $\mathcal{B}$ or $\mathcal{B}$ UL compared to the systematic uncertainties contributed by signal modes.

	MC yield (k)	data yield (k)	relative difference (%)
m_{D^0}	5,543.1 $\pm$ 5.9	5,298.3 $\pm$ 8.0	4.6
Δm	6,372.9 $\pm$ 2.9	6,136.1 $\pm$ 2.9	3.9
m_{D^0}	843.9 $\pm$ 5.4	705.6 $\pm$ 7.7	19.6
Δm	2,453.5 $\pm$ 2.1	2,247.9 $\pm$ 2.1	9.2

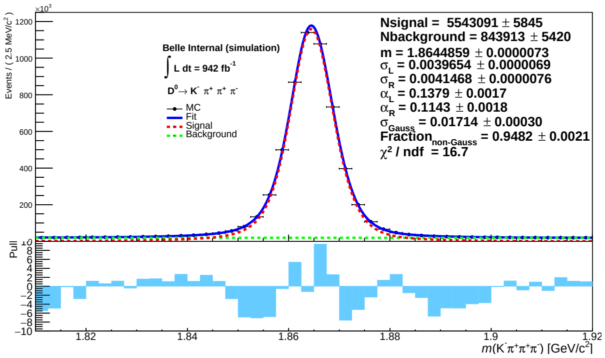

(a) m_{D^0} fit to generic MC-simulated events

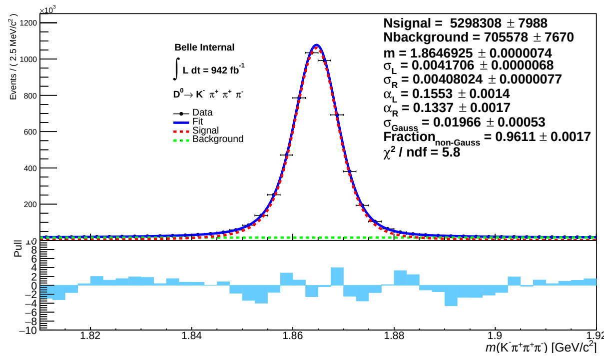

(b) m_{D^0} fit to data

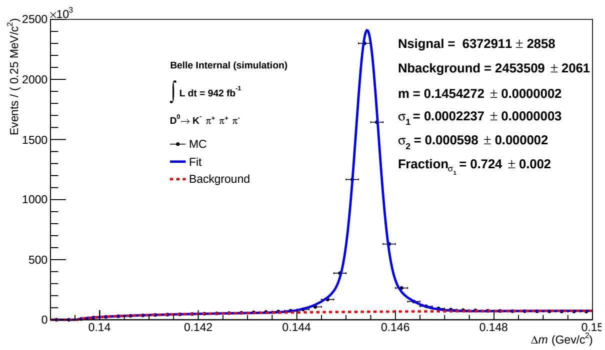

(c) Δm fit to generic MC-simulated events

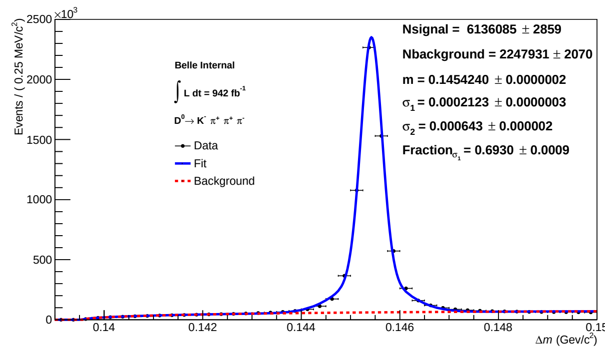

(d) Δm fit to data

Figure 4.9: $D^0 \to K^-\pi^+\pi^-\pi^+$ 1D fit to generic MC/data. The number of signal and background candidates are different for the m_{D^0} and Δm distributions because of different cuts applied. A cut on the Δm of 0.5 MeV/c^2 to the nominal value is applied to m_{D^0} distributions, and a cut on the m_{D^0} of 15 MeV/c^2 to the nominal value is applied to Δm distributions.

4.4 Fit to signal mode data m_{D^0} distributions

Here we present the results for the $D^0 \to h^- h^{(\prime)+} e^+ e^-$ signal channels using 942 fb^{-1} of Belle data. The same selections are applied to the data. The signal yield extraction is performed with an 1D unbinned maximum likelihood fit of m_{D^0}, after all final selections, vetos, and BCS based on Δm are applied. As for the MC-simulated events, we show the data m_{D^0} fit results of all the 11 signal channels (m_{ee} regions) grouped by the corresponding signal modes $K^- K^+ e^+ e^-$, $\pi^- \pi^+ e^+ e^-$ and $K^- \pi^+ e^+ e^-$. The data Δm distributions overlaid with MC are also shown. For the signal channels without significant yields observed, a 90% C.L. branching fraction upper limit is set using the CL_s method. The systematic uncertainties are described in detail in Section 4.5. The measured branching fractions and their limits are given in Table 4.10.

4.4.1 $520 < m_{ee} < 560$ MeV/c^2

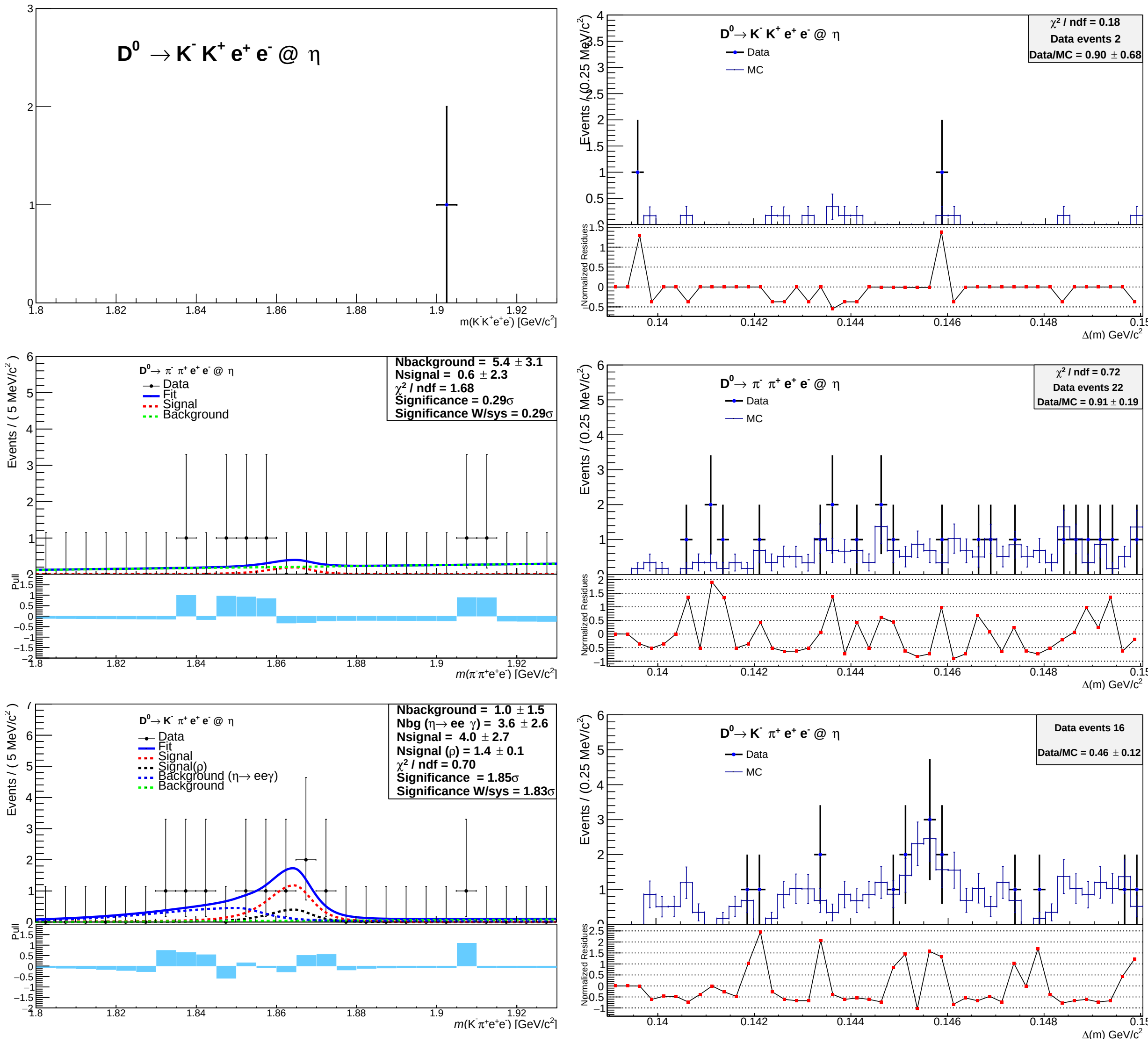

Figure 4.10: $D^0 \to h^- h^{(\prime)+} e^+ e^-$ m_{D^0} and Δm distributions with pull distributions. As can be seen, some of the bins have much larger uncertainty, which is due to only few signal MC-simulated events (event weight $<< 1$) falling into the corresponding region resulting in a bin entry much less than one event. As mentioned earlier, the m_{D^0} fit with tight Δm cut is used for the signal extraction and the Δm fit is only for reference. The $\eta \to e^+e^-\gamma$ decay background can be seen in the $D^0 \to K^-\pi^+e^+e^-$ m_{D^0} (black curve) and Δm distributions with a loose $1.85 < m_{D^0} < 1.88$ MeV/c^2 cut. The background m_{D^0} PDF parameters are fitted using ~ 400k generated $D^0 \to K^-\pi^+\eta$ $[\to e^+e^-\gamma]$ MC while the γ is not reconstructed. Fitted yield and measured branching fraction is not reported to $K^-K^+e^+e^-$ with m_{ee} at m_η region since only one event observed.

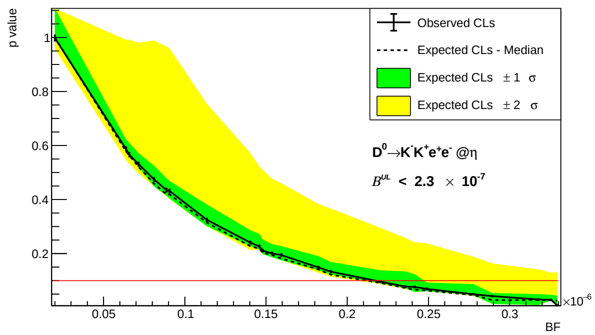

(a) $K^-K^+e^+e^-$

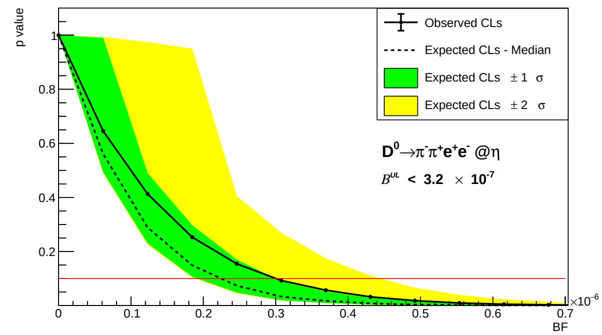

(b) $\pi^-\pi^+e^+e^-$

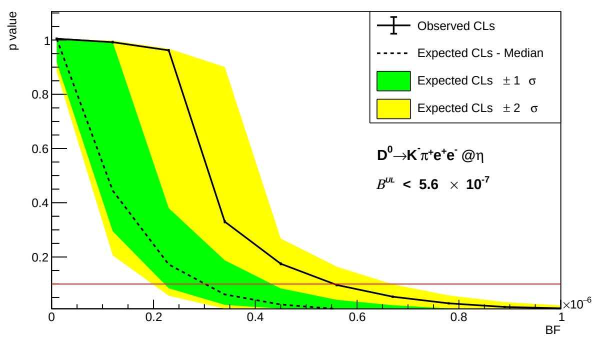

(c) $K^-\pi^+e^+e^-$

Figure 4.11: Data $D^0 \to h^-h^{(\prime)+}e^+e^-$ CL_s distribution ($520 < m_{ee} < 560$ MeV/c^2). The observed CL_s limits are obtained using data. The $\mathcal{B}$ upper limit is $\mathcal{B}^{UL} < 2.3 \times 10^{-7}$ at 90 % C.L. for $D^0 \to K^-K^+e^+e^-$ ($520 < m_{ee} < 560$ MeV/c^2) channel. The expected CL_s limits are obtained from the background-only model, where the background yield is the median of the background sampling using Toy MC experiments.

4.4.2 675 $< m_{ee} <$ 875 MeV/c^2

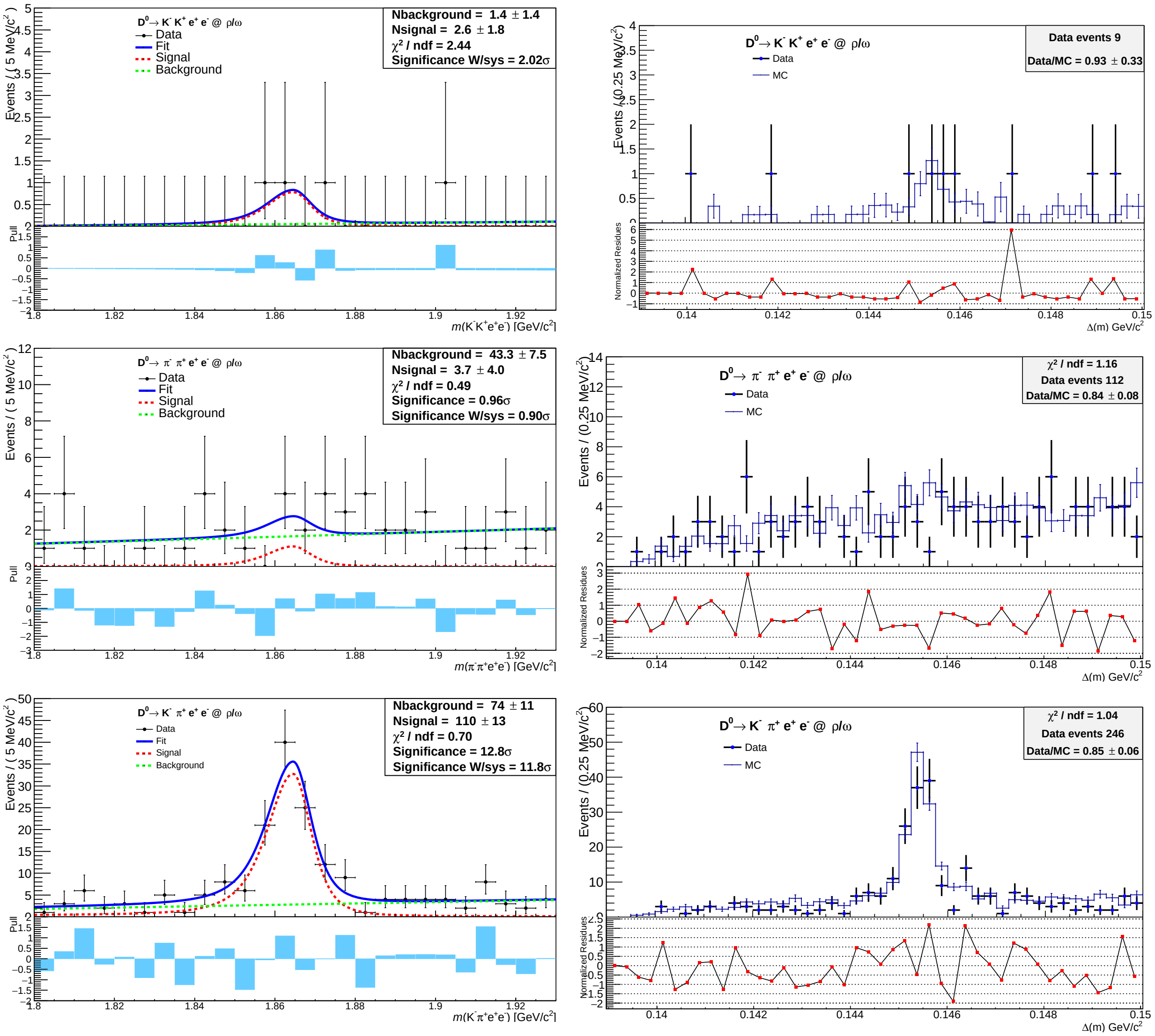

Figure 4.12: $D^0 \to h^- h^{(\prime)+} e^+ e^-$ m_{D^0} and Δm distributions (675 $< m_{ee} <$ 875 MeV/c^2). The $K^-\pi^+e^+e^-$ mode signal has a significance of 11.8 σ.

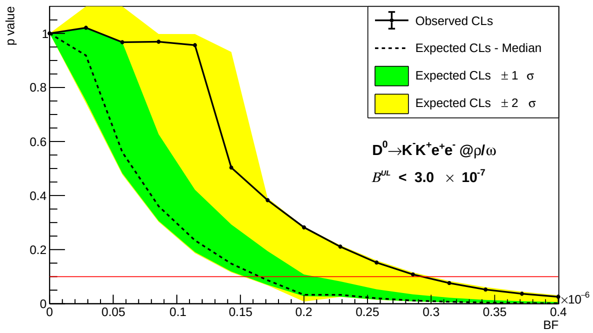

(a) $K^-K^+e^+e^-$

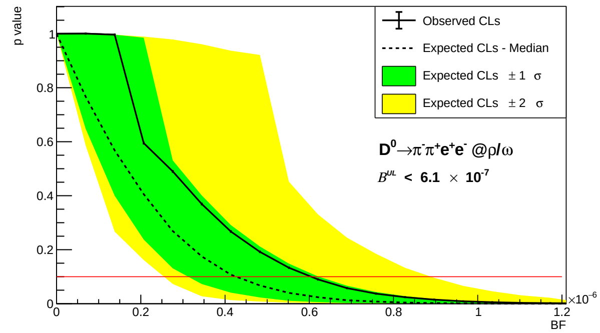

(b) $\pi^-\pi^+e^+e^-$

Figure 4.13: $D^0 \to h^- h^{(\prime)+} e^+ e^-$ CLs distribution ($675 < m_{ee} < 875$ MeV/c^2).

4.4.3 $990 < m_{ee} < 1034$ MeV/c^2

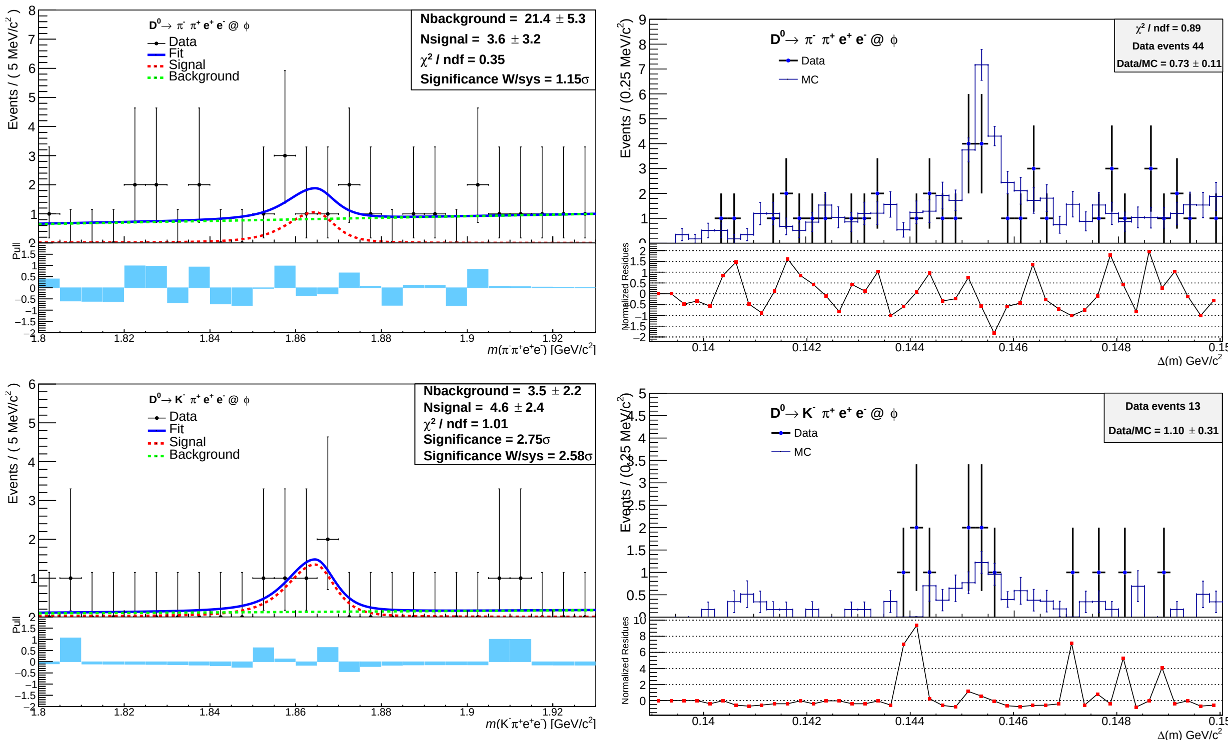

Figure 4.14: Data $D^0 \to h^- h^{(\prime)+} e^+ e^-$ m_{D^0} and Δm distributions ($990 < m_{ee} < 1034$ MeV/c^2). The large pull in the Δm comparison is due to the signal MC-simulated events having very low entries (event weight $<< 1$) resulting in some bin entries much less than one event.

4.4.4 m_{ee} non-resonant region

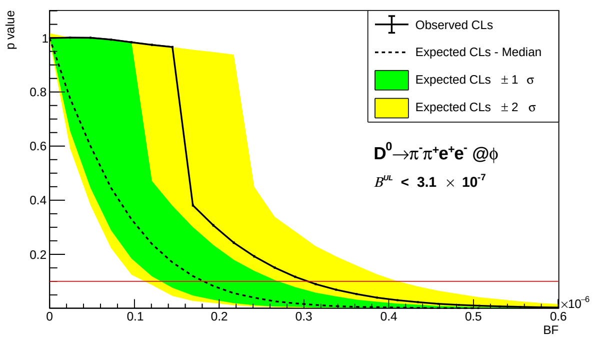

(a) $\pi^-\pi^+e^+e^-$

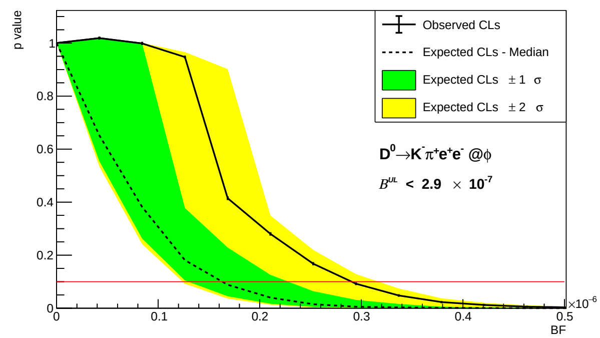

(b) $K^-\pi^+e^+e^-$

Figure 4.15: Data $D^0 \to K^-\pi^+e^+e^-$ CL_s distribution ($990 < m_{ee} < 1034$ MeV/c^2).

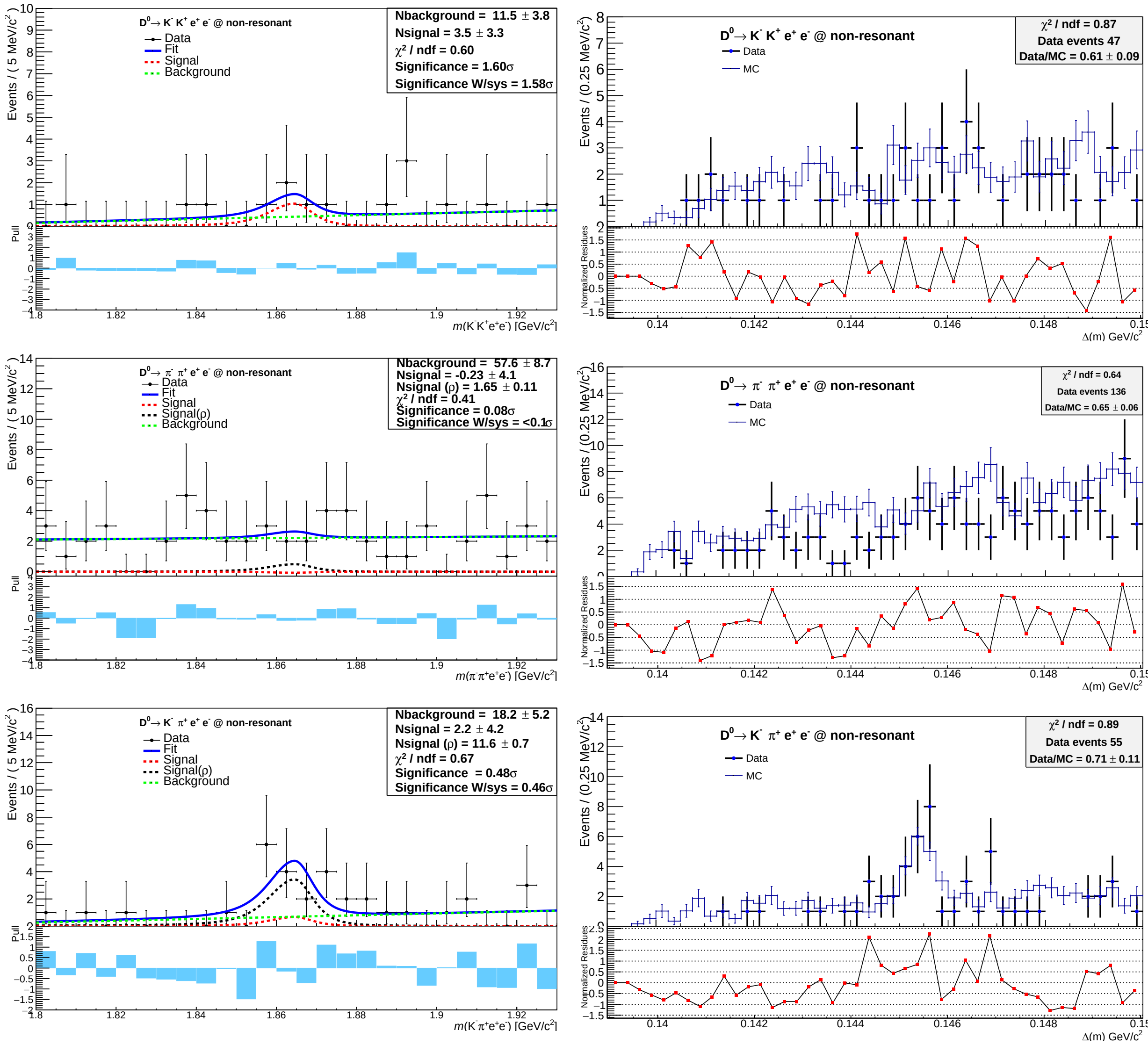

Figure 4.16: Data $D^0 \to h^- h^{(\prime)+} e^+ e^-$ m_{D^0} and Δm distributions (m_{ee} non-resonant region). The $m_{ee} > 560$ MeV/c^2 cut is applied to the $K^-\pi^+e^+e^-$ mode for removing the $\eta \to e^+e^-\gamma$ background. The calculated ρ resonance dominated Cabibbo favored resonance decay $D^0 \to K^-\pi^+e^+e^-$ background (black curve in m_{D^0} distribution) is separately indicated with fixed shape (same as the signal) and yields. The red curve shows the rest signal yields. For these NP-sensitive regions, no NP branching fraction contribution is found above the background predictions.

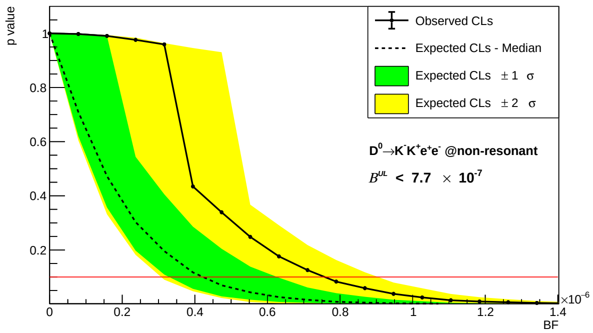

(a) $K^-K^+e^+e^-$

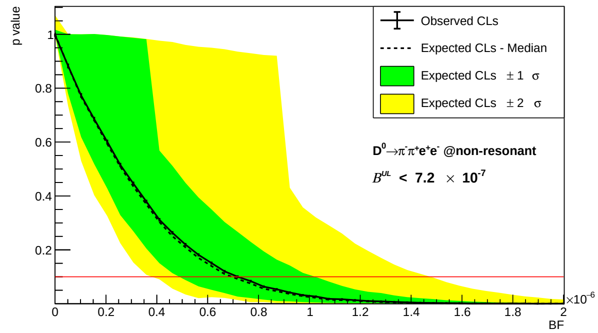

(b) $\pi^-\pi^+e^+e^-$

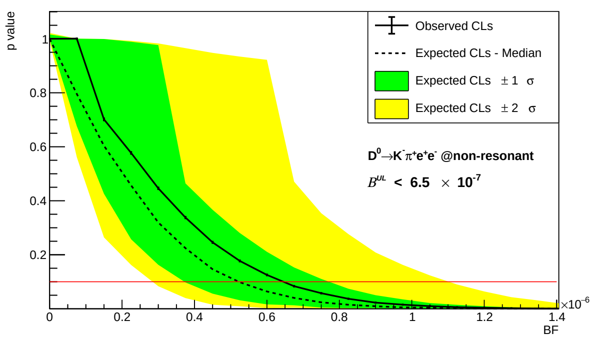

(c) $K^-\pi^+e^+e^-$

Figure 4.17: Data $D^0 \to h^-h^{(\prime)+}e^+e^-$ CL_s distribution (m_{ee} non-resonant region).

4.5 Systematic uncertainty

Systematic uncertainties need to be considered if they affect the signal yield or the branching fraction upper limits. They can be characterized by additive (affect significance) and multiplicative systematic (not affect significance) uncertainties.

4.5.1 Additive systematic uncertainty

The signal and background PDFs variations change the fit model, which affects the fit significances and contribute to the additive systematic uncertainty. The PDF related uncertainties are obtained by changing the PDF shapes and parameters for both signal and background. Table 4.5 gives the PDF functions we vary for the signal and normalization ($K^-\pi^+\pi^-\pi^+$) modes. The signal yields with different PDF shapes (parameters) are obtained using the same fitting method described in Section 6.2 with the substitution of corresponding PDF functions (parameters). The PDF related systematics are reevaluated using data after unblinding. The data fitted signal yield differences (ΔN_{sig}) are given in the tables below. Each PDF related uncertainty is assumed to be uncorrelated and summed in quadrature to calculate overall additive systematics.

Another source of additive systematic comes from the potential signal resonances (ρ dominated) decay to the non-resonan m_{ee} regions. Their uncertainties contribute mainly through the error related to the PDG $\mathcal{B}$s and the control mode ($K^-\pi^+\pi^-\pi^+$). A 5% PID systematic uncertainty is assigned based on the study of m_{ee} regions PID systematic uncertainty to the signal resonances decay uncertainties.

4.5.2 Multiplicative systematic uncertainty

The multiplicative uncertainties scale the fit results and will not affect the significance of the branching fraction measurement. The discrepancy between data and MC simulation needs to be considered when calculating the signal efficiency for data. The track finding efficiency deviation is expected to cancel since the signal modes branching fraction are measured relative to the $D^0 \to K^-\pi^+\pi^-\pi^+$, and both have the same number of tracks. The correction of signal efficiency for data is then expected to be dominated by the PID, which is $\epsilon_{data} = \epsilon_{MC} \times \frac{\epsilon^{PID}_{data}}{\epsilon^{PID}_{MC}}$. The PID efficiencies corrections are studied by Belle PID joint group. The PID efficiencies corrections are calculated by $R = \frac{1}{N}\sum_l n_l R_l$, and the uncertainty is $\Delta R = \frac{1}{N}(\sqrt{\sum_l (n_l \Delta R^{stat}_l)^2} + \sum_l n_l \Delta R^{syst}_l)$, where $R_l = \epsilon^{data}_l / \epsilon^{MC}_l$, ΔR_l is the error of R_l, n_l is the number of tracks in bin $l(p, cos\theta)$ and $N = \sum n_l$. The PID corrections are the weighted average of separately calculated corrections for SVD1 (exp 7-29) and SVD2 (exp31-71) data taking periods. After error propagation, the branching fraction systematics (in percentage) from PID is $\Delta R/R$. The branching fraction systematics from the same PID are added linearly, and the KID corrections partially cancel the $K^- K^+ e^+ e^-$ and $K^- \pi^+ e^+ e^-$ modes. The normalization mode $D^0 \to K^- \pi^+ \pi^- \pi^+$ $\mathcal{B}$ from PDG [2] is $(8.22 \pm 0.14)\%$ and its $\sim 1.7\%$ systematic uncertainty is added in quadrature with the PID systematics.

Another concern is the data and MC-simulated events PID fake rates discrepancies. To check the potential effects on the signal yield due to K, π fake e, we reconstructed $h^- h^{(\prime)+} e^+ e^-$ modes only using corresponding D^0 hadronic decay events. After applying the final selections, no peak structure is found in the m_{D^0} signal region. The PID fake rates systematic uncertainty is negligible to other systematic uncertainties.

The signal efficiencies discrepancies (Table 4.4) from the phase-space decay and potential ee resonance decay signal MC are included in the systematics. The signal efficiencies obtained using the corresponding resonance decay signal MC for branching fraction measurement and limits, the relative signal efficiencies differences are added in quadrature with the PID systematics.

Table 4.4: Signal modes reconstruction efficiencies in potential ee resonance regions using phase-space signal MC [%] ($\epsilon = \frac{\text{No. yield after final selection}}{\text{No. events generated in } m_{ee} \text{ region}}$). The relative difference is calculated using $\frac{\epsilon(\text{resonant signal MC}) - \epsilon(\text{phase-space signal MC})}{\epsilon(\text{resonant signal MC})}$ [%].

Modes $D^0 \rightarrow$	$K^-K^+e^+e^-$	$\pi^-\pi^+e^+e^-$	$K^-\pi^+e^+e^-$
η:			
Resonance	3.53 ± 0.04	5.31 ± 0.05	5.29 ± 0.04
Phase-space	3.16 ± 0.13	4.96 ± 0.17	4.53 ± 0.15
Relative difference	10.4 ± 3.9	6.6 ± 3.3	14.5 ± 3.0
ρ, ω:			
Resonance	6.00 ± 0.06	5.69 ± 0.05	8.01 ± 0.06
Phase-space	6.16 ± 0.09	5.81 ± 0.04	8.27 ± 0.05
Relative difference	-2.7 ± 1.7	-2.1 ± 1.2	-3.4 ± 1.7
ϕ:			
Resonance	-	9.41 ± 0.06	9.19 ± 0.06
Phase-space	-	8.45 ± 0.14	8.95 ± 0.22
Relative difference	-	10.2 ± 1.6	2.7 ± 2.5

A summary of the systematic uncertainties for $K^-\pi^+e^+e^-$ with m_{ee} in $m_{\rho/\omega}$ region and normalization mode ($K^-\pi^+\pi^-\pi^+$) is given below in Table 4.6. The PID systematics are added in quadrature for the eID and the KID with possible cancellation depending on corresponding signal modes. The additive systematic uncertainties are added in quadrature. The significances with systematics are obtained by convoluting the fit model with one Gaussian constraint function ($\mu = 0$, $\sigma =$ total signal additive uncertainty). The branching fraction upper limits with the systematic are obtained by convoluting the fit model with three Gaussian constraint functions. There are two Gaussian constraint functions for signal systematics, one for the signal additive systematic uncertainty ($\mu = 0$, $\sigma =$ total signal additive uncertainty) and the other for the multiplicative systematic uncertainty ($\mu = 1$, $\sigma =$ total multiplicative [2]). The signal yield with systematic becomes $N'_{sig} = N_{sig} \times \epsilon + \Delta N_{sig}$ where ϵ and ΔN_{sig} are nuisance parameters. The normalization mode systematic uncertainties are also incorporated into limits using the same method as the signal systematic uncertainties through the third Gaussian constraint function ($\mu = 0$, $\sigma =$ total normalization additive uncertainty), which barely gives an increase to the limits, as expected. The signal yield is written as a product of signal $\mathcal{B}$ (parameter of interest), signal efficiency, normalization yield, normalization efficiency, and normalization $\mathcal{B}$ to obtain the $\mathcal{B}$ limits with systematic uncertainties. The signal yield with systematic yield becomes

$N'_{sig} =$

$\mathcal{B}(\text{parameter of interest}) \times (N_{norm} + \Delta N_{norm}) \times \epsilon_{data\,sig} \times \frac{1}{\epsilon_{data\,norm}} \times \frac{1}{\mathcal{B}(D^0 \to K^-\pi^+\pi^-\pi^+)} \times \epsilon + \Delta N_{sig}$,

where the ΔN_{norm}, ϵ, and ΔN_{sig} are nuisance parameters. The fit model (unbinned, extended) $N'_{sig}\text{PDF}_{sig} + N_{bkg}\text{PDF}_{bkg}$ is then convoluted by three Gaussian constraint functions described above. The CL_s method is used to obtain the $\mathcal{B}$ limits with systematic uncertainties. Tables 4.7 - 4.9 summarizes systematic uncertainties for other signal modes.

[2] The KID systematic from normalization mode $K^-\pi^+\pi^-\pi^+$ are included or canceled depending on the signal channel

Table 4.5: PDF functions used for signal and normalization modes for systematics estimations.

Modes	$h^-h^{(\prime)+}e^+e^-$	$K^-\pi^+\pi^-\pi^+$
Signal PDF	Double CrystalBall [66] with shared mean	Signal mode PDF Double Gaussians with shared mean
Background PDF	Second-order Chebychev polynomial	-

Table 4.6: Summary of $K^-\pi^+e^+e^-$ ($m_{ee} \in m_{\rho/\omega}$), $K^-\pi^+\pi^-\pi^+$ systematic uncertainties. The total systematics for the signal mode includes the systematics for the normalization mode with KID cancellations.

	$K^-\pi^+e^+e^-$	$K^-\pi^+\pi^-\pi^+$
Additive (ΔN_{sig})		
PDF variations:		
Double CrystalBall	-0.4	-
Double Gaussians	-	-175,293
Signal mode PDF	-	87,577
Second-order *cheb.*	0.6	-
Floating signal PDF parameters	2.3	-
Total Additive ΔN_{sig}	2.4	196k
Multiplicative (%)		
PID eff. Corrections:		
K ID	0.80	1.07
e ID	4.45	-
MC efficiencies:		
PHSP vs Resonant MC	-3.4	-
Total Multiplicative (%)	5.7	1.1

Table 4.7: Summary of $K^-\pi^+e^+e^-$ systematic uncertainties in different m_{ee} regions. The total systematics for the signal mode includes the systematics for the normalization mode with KID cancellations (same for other signal modes below, if applicable).

Additive (ΔN_{sig})	η	ϕ	non-resonant m_{ee} region
PDF Variation:			
Double CrystalBall	0.1	-0.1	-0.1
Second-order *cheb.*	-0.2	0.4	0.7
$\eta \to e^+e^-\gamma$ background	0.7	-	-
Resonance decays pollution	0.1	-	0.7
Total Additive ΔN_{sig}	0.8	0.4	1.1
Multiplicative (%)			
PID eff. Corrections:			
K ID	0.77	0.80	0.80
e ID	4.56	4.22	3.99
MC efficiencies:			
PHSP vs Resonant MC	14.5	2.7	-
Total Multiplicative (%)	15.3	5.1	4.0

Table 4.8: Summary of $K^-K^+e^+e^-$ systematic uncertainties in different m_{ee} regions. A 0.5 additive systematic is set for $K^-K^+e^+e^-$ @ η region as only one event is observed in data.

Additive (ΔN_{sig})	η	ρ	non-resonant m_{ee} region
PDF Variation:			
Double CrystalBall	-	0.06	-0.1
Second-order *cheb.*	-	-0.09	0.2
Resonance decays pollution	-	-	0.2
Total Additive ΔN_{sig}	0.5	0.11	0.3
Multiplicative (%)			
PID eff. Corrections:			
K ID	1.55	1.63	1.67
e ID	4.80	4.67	4.96
MC efficiencies:			
PHSP vs Resonant MC	10.4	-2.7	-
Total Multiplicative (%)	11.6	5.6	5.1

Table 4.9: Summary of $\pi^-\pi^+e^+e^-$ systematic uncertainties in different m_{ee} regions.

Additive (ΔN_{sig})	η	ρ	ϕ	non-resonant m_{ee} region
PDF Variation:				
Double CrystalBall	-0.1	-0.2	-0.1	-0.6
Second-order *cheb.*	-0.2	-1.3	-0.2	0.8
Resonance decays pollution	-	-	-	0.1
Total Additive ΔN_{sig}	0.3	1.4	0.3	1.0
Multiplicative (%)				
PID eff. Corrections:				
π ID	1.72	1.74	1.82	1.87
e ID	4.43	4.39	4.26	3.98
MC efficiencies:				
PHSP vs Resonant MC	6.6	-2.1	10.2	-
Total Multiplicative (%)	8.3	5.3	11.3	4.6

4.6 Signal modes measured branching fractions and upper limits

The data and MC are in good agreement for the majority of the channels except for the $\pi^-\pi^+e^+e^-$ for ee in ϕ mass region where the data fitted signal yield is $\sim 1.8\sigma$ less than the MC expected from corresponding $\mathcal{B}$, and $K^-K^+e^+e^-$ @ non-resonant mass region where data background is $\sim 3\sigma$ less than MC predicted. Table 4.10 below summarises all signal channels' measured branching fractions and branching fraction upper limits. The preliminary results have been approved by the Belle (I + II) collaboration and shown at the Moriond 2024 conference.

Table 4.10: $D^0 \to h^-h^{(\prime)+}e^+e^-$ decay data fitted signal yield, significance, branching fraction ($\pm\, stat \pm\, syst$), branching fraction upper limits @ 90% C.L. [10^{-7}]. The data fit results are presented in Section 6.3.2. The corresponding MC estimation is shown as a reference. The *BABAR* and BESIII branching fraction (upper limits) are also listed, if available.

m_{ee} region	[MeV/c^2]	Signal yield MC yield	Significance MC Significance	$\mathcal{B}$ MC $\mathcal{B}$	$\mathcal{B}$ UL @ 90% C.L. MC UL	*BABAR* and BES III $\mathcal{B}$ (UL @ 90% C.L.) [43, 46]
$K^-K^+e^+e^-$						
η	520-560	-	$< 0.1\sigma$	-	< 2.3	
		-	$< 0.1\sigma$	-	< 2.1	
ρ^0/ω	> 675	2.6 ± 1.8	2.0σ	1.2 ± 0.9 ± 0.1	< 3.0	
		3.0 ± 2.0	2.1σ	1.3 ± 0.9	< 3.2	< 410 [46]
non-resonant	> 200 [3]	3.5 ± 3.3	1.5σ	3.1 ± 3.0 ± 0.4	< 7.7	
		-0.61 ± 3.0	0.2σ	-0.5 ± 2.6	< 5.0	
$\pi^-\pi^+e^+e^-$						
η	520-560	0.6 ± 2.3	0.3σ	0.4 ± 1.4 ± 0.2	< 3.2	
		-1.2 ± 1.7	0.6σ	-0.6 ± 0.9	< 2.2	
ρ^0/ω	675-875	3.7 ± 4.1	0.9σ	2.0 ± 2.2 ± 0.8	< 6.1	
		8.0 ± 5.1	1.7σ	3.8 ± 2.4	< 7.0	< 70 [46]
ϕ	995-1035	3.6 ± 3.2	1.1σ	1.1 ± 1.1 ± 0.2	< 3.1	
		14.5 ± 4.8	4.0σ	4.1 ± 1.4	< 4.5	
non-resonant	> 200	−0.2 ± 4.1	$< 0.1\sigma$	−0.2 ± 3.4 ± 0.9	< 7.2	
		1.0 ± 4.2	0.2σ	0.7 ± 3.1	< 7.6	
$K^-\pi^+e^+e^-$						
η	520-560	4.0 ± 2.7	1.6σ	2.2 ± 1.5 ± 0.5	< 5.6	
		1.0 ± 2.8	0.3σ	0.4 ± 1.3	< 5.0	
ρ^0/ω	675-875	110 ± 13	11.8σ	39.6 ± 4.5 ± 2.9	-	40.0 ± 5.0 ± 2.2 [43]
		120 ± 13	12.0σ	41.6 ± 4.5	-	< 110 [46]
ϕ	990-1034	4.6 ± 2.4	2.5σ	1.4 ± 0.8 ± 0.3	< 2.9	
		3.3 ± 2.2	1.9σ	1.0 ± 0.7	< 2.4	
non-resonant	> 560	2.2 ± 4.2	0.4σ	1.3 ± 2.4 ± 0.6	< 6.5	
		0.9 ± 6.6	0.1σ	1.5 ± 3.1	< 6.8	< 31 [43]

CHAPTER 5. CONCLUSIONS

A result of the search of the rare charm meson decay $D^0 \to h^- h^{(\prime)+} e^+ e^-$ is reported. No BSM contributions are found above the background predictions for the $D^0 \to h^- h^{(\prime)+} e^+ e^-$ channels. The branching fraction upper limits in different m_{ee} regions of the decay $D^0 \to h^- h^{(\prime)+} e^+ e^-$ are set to be the in range of $[2.3, 7.7] \times 10^{-7}$, which are the world's best branching fraction upper limits to date. The branching fraction of the decay $D^0 \to K^- \pi^+ e^+ e^-$ is measured to be $(39.6 \pm 4.5\,(stat) \pm 2.9\,(syst)) \times 10^{-7}$, in the invariant mass region $675 < m_{ee} < 875\,\mathrm{MeV}/c^2$ ($m_{\rho/\omega}$) using 942 fb^{-1} data collected by Belle. The measured $\mathcal{B}$ is consistent with *BABAR* measurement. To reduce the systematics, the signal $\mathcal{B}$ is measured relative to the normalization mode $D^0 \to K^- \pi^+ \pi^- \pi^+$. The D^0 hadronic decay vetos and Bremsstrahlung recovery are applied to increase the sensitivity.

The Belle II experiment with improved detector performance is expected to deliver 50 ab^{-1} of data, so it is expected to get 50 times of signal yields and about seven times better sensitivity, which brings the branching fraction limits to the order of $\mathcal{O}(10^{-8})$ plus beneficial of improved detector performance. With Belle II data, we expect to observe the decays $D^0 \to \pi^- \pi^+ e^+ e^-$ ($m_{ee} \in m_{\rho/\omega}$ and m_ϕ), and $D^0 \to K^- K^+ e^+ e^-$ ($m_{ee} \in m_{\rho/\omega}$), based on the corresponding LHCb $\mu\mu$ channel $\mathcal{B}$s with the assumption of LFU. The angular analysis and CP violation searches can be performed for $D^0 \to K^- \pi^+ e^+ e^-$ and $\pi^- \pi^+ e^+ e^-$ modes with 50 times of signal. On the other hand, the sensitivity to the $D^0 \to h^- h^{(\prime)+} e^+ e^-$ branching fraction measurements may be further extracted with the help of a charm tagging algorithm and the implementation of machine learning methods for particle identifications and signal event selections.

BIBLIOGRAPHY

[1] A. Pais and S. B. Treiman. "How Many Charm Quantum Numbers are There?" In: *Phys. Rev. Lett.* 35 (23 Dec. 1975), pp. 1556–1559. DOI: 10.1103/PhysRevLett.35.1556.

[2] R. L. Workman et al. "Review of Particle Physics". In: *PTEP* 2022 (2022), p. 083C01. DOI: 10.1093/ptep/ptac097.

[3] J. J. Thomson. "Cathode rays". In: *Phil. Mag. Ser. 5* 44 (1897), pp. 293–316. DOI: 10.1080/14786449708621070.

[4] Y. Fukuda et al. "Evidence for Oscillation of Atmospheric Neutrinos". In: *Phys. Rev. Lett.* 81 (8 Aug. 1998), pp. 1562–1567. DOI: 10.1103/PhysRevLett.81.1562.

[5] S. L. Glashow, J. Iliopoulos, and L. Maiani. "Weak Interactions with Lepton-Hadron Symmetry". In: *Phys. Rev. D* 2 (7 Oct. 1970), pp. 1285–1292. DOI: 10.1103/PhysRevD.2.1285.

[6] Nicola Cabibbo. "Unitary Symmetry and Leptonic Decays". In: *Phys. Rev. Lett.* 10 (12 June 1963), pp. 531–533. DOI: 10.1103/PhysRevLett.10.531.

[7] Makoto Kobayashi and Toshihide Maskawa. "CP-Violation in the Renormalizable Theory of Weak Interaction". In: *Progress of Theoretical Physics* 49.2 (Feb. 1973), pp. 652–657. ISSN: 0033-068X. DOI: 10.1143/PTP.49.652.

[8] ATLAS Collaboration. "A Particle Consistent with the Higgs Boson Observed with the ATLAS Detector at the Large Hadron Collider". In: *Science* 338.6114 (2012), pp. 1576–1582. DOI: 10.1126/science.1232005.

[9] ATLAS Collaboration. "Observation of a new particle in the search for the Standard Model Higgs boson with the ATLAS detector at the LHC". In: *Physics Letters B* 716.1 (2012), pp. 1–29. ISSN: 0370-2693. DOI: https://doi.org/10.1016/j.physletb.2012.08.020.

[10] CMS Collaboration. "Observation of a new boson at a mass of 125 GeV with the CMS experiment at the LHC". In: *Physics Letters B* 716.1 (Sept. 2012), pp. 30–61. ISSN: 0370-2693. DOI: 10.1016/j.physletb.2012.08.021. URL: http://dx.doi.org/10.1016/j.physletb.2012.08.021.

[11] F. Englert and R. Brout. "Broken Symmetry and the Mass of Gauge Vector Mesons". In: *Phys. Rev. Lett.* 13 (1964). Ed. by J. C. Taylor, pp. 321–323. DOI: 10.1103/PhysRevLett.13.321.

[12] Peter W. Higgs. "Broken symmetries, massless particles and gauge fields". In: *Phys. Lett.* 12 (1964), pp. 132–133. DOI: 10.1016/0031-9163(64)91136-9.

[13] Ahmed Abokhalil. *The Higgs Mechanism and Higgs Boson: Unveiling the Symmetry of the Universe.* 2023. arXiv: 2306.01019 [hep-ph].

[14] Jeremy Bernstein. "Spontaneous symmetry breaking, gauge theories, the Higgs mechanism and all that". In: *Rev. Mod. Phys.* 46 (1 Jan. 1974), pp. 7–48. DOI: 10.1103/RevModPhys.46.7. URL: https://link.aps.org/doi/10.1103/RevModPhys.46.7.

[15] David J Griffiths. *Introduction to elementary particles; 2nd rev. version.* Physics textbook. New York, NY: Wiley, 2008. URL: https://cds.cern.ch/record/111880.

[16] *SM diagrams of K^0 decays into two muons.* URL: https://en.wikipedia.org/wiki/Charm_quark#/media/File:K0_decay_to_muons.svg.

[17] J. H. Christenson et al. "Evidence for the 2π Decay of the K_2^0 Meson". In: *Phys. Rev. Lett.* 13 (4 July 1964), pp. 138–140. DOI: 10.1103/PhysRevLett.13.138.

[18] Ling-Lie Chau and Wai-Yee Keung. "Comments on the Parametrization of the Kobayashi-Maskawa Matrix". In: *Phys. Rev. Lett.* 53 (19 Nov. 1984), pp. 1802–1805. DOI: 10.1103/PhysRevLett.53.1802.

[19] Lincoln Wolfenstein. "Parametrization of the Kobayashi-Maskawa Matrix". In: *Phys. Rev. Lett.* 51 (21 Nov. 1983), pp. 1945–1947. DOI: 10.1103/PhysRevLett.51.1945.

[20] J. -E. Augustin et al. "Discovery of a Narrow Resonance in e^+e^- Annihilation". In: *Phys. Rev. Lett.* 33 (23 Dec. 1974), pp. 1406–1408. DOI: 10.1103/PhysRevLett.33.1406. URL: https://link.aps.org/doi/10.1103/PhysRevLett.33.1406.

[21] J. J. Aubert et al. "Experimental Observation of a Heavy Particle J". In: *Phys. Rev. Lett.* 33 (23 Dec. 1974), pp. 1404–1406. DOI: 10.1103/PhysRevLett.33.1404. URL: https://link.aps.org/doi/10.1103/PhysRevLett.33.1404.

[22] American Institute of Physics. *Interview of Wolfgang Panofsky by Harvey Lynch on 1997 April 11 and May 2, Niels Bohr Library Archives.* URL: https://www.aip.org/history-programs/niels-bohr-library/oral-histories/5906.

[23] G. Goldhaber et al. "Observation in e^+e^- Annihilation of a Narrow State at 1865 MeV/c^2 Decaying to $K\pi$ and $K\pi\pi\pi$". In: *Phys. Rev. Lett.* 37 (5 Aug. 1976), pp. 255–259. DOI: 10.1103/PhysRevLett.37.255. URL: https://link.aps.org/doi/10.1103/PhysRevLett.37.255.

[24] "Evidence for penguin-diagram decays: First observation of B→$K^*(892)\gamma$". In: *Phys. Rev. Lett.* 71 (5 Aug. 1993), pp. 674–678. DOI: 10.1103/PhysRevLett.71.674.

[25] J. Ellis et al. "The phenomenology of the next left-handed quarks". In: *Nuclear Physics B* 131.2 (1977), pp. 285–307. ISSN: 0550-3213. DOI: https://doi.org/10.1016/0550-3213(77)90374-1.

[26] "The Belle II Physics Book". In: *Progress of Theoretical and Experimental Physics* 2019.12 (Dec. 2019). ISSN: 2050-3911. DOI: 10.1093/ptep/ptz106. URL: http://dx.doi.org/10.1093/ptep/ptz106.

[27] Suchismita Sahoo and Rukmani Mohanta. "New physics effects in charm meson decays involving $c \to ul^+l^-(l_i^{\mp}l_j^{\pm})$ transitions". In: *The European Physical Journal C* 77.5 (2017), p. 344. DOI: 10.1140/epjc/s10052-017-4888-4. URL: https://doi.org/10.1140/epjc/s10052-017-4888-4.

[28] Svjetlana Fajfer and Nejc Ko šnik. "Resonance catalyzed CP asymmetries in $D \to P\ell^+\ell^-$". In: *Phys. Rev. D* 87 (5 Mar. 2013), p. 054026. DOI: 10.1103/PhysRevD.87.054026. URL: https://link.aps.org/doi/10.1103/PhysRevD.87.054026.

[29] J. P. Lees et al. "Measurement of Branching Fractions and Rate Asymmetries in the Rare Decays $B \to K^{(*)}l^+l^-$". In: *Phys. Rev.* D86 (2012), p. 032012. DOI: 10.1103/PhysRevD.86.032012. arXiv: 1204.3933 [hep-ex].

[30] J. -T. Wei et al. "Measurement of the Differential Branching Fraction and Forward-Backword Asymmetry for $B \to K^{(*)}\ell^+\ell^-$". In: *Phys. Rev. Lett.* 103 (2009), p. 171801. DOI: 10.1103/PhysRevLett.103.171801. arXiv: 0904.0770 [hep-ex].

[31] Roel Aaij et al. "Measurement of Form-Factor-Independent Observables in the Decay $B^0 \to K^{*0}\mu^+\mu^-$". In: *Phys. Rev. Lett.* 111 (2013), p. 191801. DOI: 10.1103/PhysRevLett.111.191801. arXiv: 1308.1707 [hep-ex].

[32] Roel Aaij et al. "Differential branching fractions and isospin asymmetries of $B \to K^{(*)}\mu^+\mu^-$ decays". In: *JHEP* 06 (2014), p. 133. DOI: 10.1007/JHEP06(2014)133. arXiv: 1403.8044 [hep-ex].

[33] Roel Aaij et al. "Measurement of lepton universality parameters in $B^+ \to K^+\ell^+\ell^-$ and $B^0 \to K^{*0}\ell^+\ell^-$ decays". In: (Dec. 2022). arXiv: 2212.09153 [hep-ex].

[34] "Measurement of lepton universality parameters in $B^+ \to K^+\ell^+\ell^-$ and $B^0 \to K^{*0}\ell^+\ell^-$ decays". In: *Phys. Rev. D* 108 (3 Aug. 2023), p. 032002. DOI: 10.1103/PhysRevD.108.032002. URL: https://link.aps.org/doi/10.1103/PhysRevD.108.032002.

[35] "Test of Lepton Universality in $b \to s\ell^+\ell^-$ Decays". In: *Phys. Rev. Lett.* 131 (5 Aug. 2023), p. 051803. DOI: 10.1103/PhysRevLett.131.051803. URL: https://link.aps.org/doi/10.1103/PhysRevLett.131.051803.

[36] S. Fajfer et al. "The Rare decays of D mesons". In: *Nucl. Phys. Proc. Suppl.* 115 (2003), pp. 93–97. DOI: 10.1016/S0920-5632(02)01961-8. arXiv: hep-ph/0208201 [hep-ph].

[37] S. de Boer and G. Hiller. "Flavor and new physics opportunities with rare charm decays into leptons". In: *Phys. Rev.* D93.7 (2016), p. 074001. DOI: 10.1103/PhysRevD.93.074001. arXiv: 1510.00311 [hep-ph].

[38] Stefan de Boer and Gudrun Hiller. "Null tests from angular distributions in $D \to P_1P_2l^+l^-$, $l = e, \mu$ decays on and off peak". In: *Phys. Rev. D* 98 (3 Aug. 2018), p. 035041. DOI: 10.1103/PhysRevD.98.035041. URL: https://link.aps.org/doi/10.1103/PhysRevD.98.035041.

[39] R. Bause et al. "The New Physics Reach of Null Tests with $D \to \pi\ell\ell$ and $D_s \to K\ell\ell$ Decays". In: *Eur. Phys. J.* (2019). DOI: 10.1140/epjc/s10052-020-7621-7. arXiv: 1909.11108 [hep-ph].

[40] Svjetlana Fajfer, Eleftheria Solomonidi, and Luiz Vale Silva. "S-wave contribution to rare $D^0 \to \pi^+\pi^-\ell^+\ell^-$ decays in the standard model and sensitivity to new physics". In: *Phys. Rev. D* 109 (3 Feb. 2024), p. 036027. DOI: 10.1103/PhysRevD.109.036027. URL: https://link.aps.org/doi/10.1103/PhysRevD.109.036027.

[41] S. Sahoo and R. Mohanta. "New physics effects in charm meson decays involving $c \to ul^+l^-(l_i^{\mp}l_j^{\pm})$ transitions". In: *Eur. Phys. J.* C77.5 (2017), p. 344. DOI: 10.1140/epjc/s10052-017-4888-4. arXiv: 1705.02251 [hep-ph].

[42] J. P. Lees et al. "Searches for Rare or Forbidden Semileptonic Charm Decays". In: *Phys. Rev.* D84 (2011), p. 072006. DOI: 10.1103/PhysRevD.84.072006. arXiv: 1107.4465 [hep-ex].

[43] J. P. Lees et al. "Observation of the Decay $D^0 \to K^-\pi^+e^+e^-$". In: *Phys. Rev. Lett.* 122.8 (2019), p. 081802. DOI: 10.1103/PhysRevLett.122.081802. arXiv: 1808.09680 [hep-ex].

[44] J. P. Lees et al. "Search for rare or forbidden decays of the D^0 meson". In: *Phys. Rev. Lett.* 124.7 (2020), p. 071802. arXiv: 1905.00608 [hep-ex].

[45] J. P. Lees et al. "Search for lepton-flavor-violating decays $D^0 \to X^0 e^\pm \mu^\mp$". In: *Phys. Rev. D* 101.11 (2020), p. 112003. DOI: 10.1103/PhysRevD.101.112003. arXiv: 2004.09457 [hep-ex].

[46] M. Ablikim et al. "Search for the rare decays $D \to h(h')e^+e^-$". In: *Phys. Rev.* D97.7 (2018), p. 072015. DOI: 10.1103/PhysRevD.97.072015. arXiv: 1802.09752 [hep-ex].

[47] A. Freyberger et al. "Limits on flavor changing neutral currents in D^0 meson decays". In: *Phys. Rev. Lett.* 76 (1996). [Erratum: Phys. Rev. Lett.77,2147(1996)], pp. 3065–3069. DOI: 10.1103/PhysRevLett.76.3065,10.1103/PhysRevLett.77.2147.

[48] K. Kodama et al. "Upper limits of charm hadron decays to two muons plus hadrons". In: *Phys. Lett.* B345 (1995), pp. 85–92. DOI: 10.1016/0370-2693(94)01610-O.

[49] E. M. Aitala et al. "Search for rare and forbidden charm meson decays $D^0 \to V\ell^+\ell^-$ and $hh\ell\ell$". In: *Phys. Rev. Lett.* 86 (2001), pp. 3969–3972. DOI: 10.1103/PhysRevLett.86.3969. arXiv: hep-ex/0011077 [hep-ex].

[50] Roel Aaij et al. "First observation of the decay $D^0 \to K^-\pi^+\mu^+\mu^-$ in the ρ^0-ω region of the dimuon mass spectrum". In: *Phys. Lett.* B757 (2016), pp. 558–567. DOI: 10.1016/j.physletb.2016.04.029. arXiv: 1510.08367 [hep-ex].

[51] Roel Aaij et al. "Observation of D^0 meson decays to $\pi^+\pi^-\mu^+\mu^-$ and $K^+K^-\mu^+\mu^-$ final states". In: *Phys. Rev. Lett.* 119.18 (2017), p. 181805. DOI: 10.1103/PhysRevLett.119.181805. arXiv: 1707.08377 [hep-ex].

[52] Roel Aaij et al. "Search for the rare decay $\Lambda_c^+ \to p\mu^+\mu^-$". In: *Phys. Rev.* D97.9 (2018), p. 091101. DOI: 10.1103/PhysRevD.97.091101. arXiv: 1712.07938 [hep-ex].

[53] Luigi Cappiello, Oscar Catà, and Giancarlo D'Ambrosio. "Standard Model prediction and new physics tests for $D^0 \to h_1^+ h_2^- l^+ l^- (h = K, \pi; l = e, \mu)$". In: *Journal of High Energy Physics* 2013.4 (2013), p. 135. DOI: 10.1007/JHEP04(2013)135. URL: https://doi.org/10.1007/JHEP04(2013)135.

[54] Stefan de Boer and Gudrun Hiller. "Null tests from angular distributions in $D \to P_1 P_2 l^+ l^-$, $l = e$, μ decays on and off peak". In: *Phys. Rev. D* 98 (3 Aug. 2018), p. 035041. DOI: 10.1103/PhysRevD.98.035041. URL: https://link.aps.org/doi/10.1103/PhysRevD.98.035041.

[55] D Besson and T Skwarnicki. "Upsilon Spectroscopy: Transitions in the Bottomonium System". In: *Annual Review of Nuclear and Particle Science* 43.Volume 43, 1993 (1993), pp. 333–378. ISSN: 1545-4134. DOI: https://doi.org/10.1146/annurev.ns.43.120193.002001. URL: https://www.annualreviews.org/content/journals/10.1146/annurev.ns.43.120193.002001.

[56] S. Kurokawa and Eiji Kikutani. "Overview of the KEKB accelerators". In: *Nucl. Instrum. Meth. A* 499 (2003), pp. 1–7. DOI: 10.1016/S0168-9002(02)01771-0.

[57] A. J. Bevan et al. "The Physics of the B Factories". In: *Eur. Phys. J. C* 74 (2014), p. 3026. DOI: 10.1140/epjc/s10052-014-3026-9. arXiv: 1406.6311 [hep-ex].

[58] K. Akai et al. In: *Nuclear Instruments and Methods in Physics Research Section A: Accelerators, Spectrometers, Detectors and Associated Equipment* 499.1 (2003). KEK-B: The KEK B-factory, pp. 191–227. ISSN: 0168-9002. DOI: https://doi.org/10.1016/S0168-9002(02)01788-6. URL: https://www.sciencedirect.com/science/article/pii/S0168900202017886.

[59] H. Aihara et al. "Belle SVD2 vertex detector". In: *Nuclear Instruments and Methods in Physics Research Section A: Accelerators, Spectrometers, Detectors and Associated Equipment* 568.1 (2006). New Developments in Radiation Detectors, pp. 269–273. ISSN: 0168-9002. DOI: https://doi.org/10.1016/j.nima.2006.05.281. URL: https://www.sciencedirect.com/science/article/pii/S0168900206011193.

[60] H. Bethe. "Zur Theorie des Durchgangs schneller Korpuskularstrahlen durch Materie". In: *Annalen der Physik* 397.3 (1930), pp. 325–400. DOI: https://doi.org/10.1002/andp.19303970303. URL: https://onlinelibrary.wiley.com/doi/abs/10.1002/andp.19303970303.

[61] T. Kuhr et al. In: *Comput. Softw. Big Sci.* 3.1 (2019), p. 1. DOI: 10.1007/s41781-018-0017-9. arXiv: 1809.04299 [physics.comp-ph].

[62] D. J. Lange. In: *Nucl. Instrum. Meth. A* 462 (2001). Ed. by S. Erhan, P. Schlein, and Y. Rozen, pp. 152–155. DOI: 10.1016/S0168-9002(01)00089-4.

[63] D. Kirkby W. Verkerke. *RooFit Users Manual v2.91.* https://root.cern.ch/download/doc/RooFit_Users_Manual_2.91-33.pdf. Document version 2.91-33.

[64] Wouter Verkerke and David Kirkby. *The RooFit toolkit for data modeling.* 2003. arXiv: physics/0306116 [physics.data-an].

[65] A L Read. "Presentation of search results: the CLs technique". In: *Journal of Physics G: Nuclear and Particle Physics* 28.10 (Sept. 2002), p. 2693. DOI: 10.1088/0954-3899/28/10/313. URL: https://dx.doi.org/10.1088/0954-3899/28/10/313.

[66] Tomasz Skwarnicki. "A study of the radiative CASCADE transitions between the Upsilon-Prime and Upsilon resonances". PhD thesis. Cracow, INP, 1986.

[67] D. Griffiths. *Introduction to Elementary Particles. 2nd Edition.* Wiley-VCH, Weinheim, 2008.

[68] J. E. Augustin et al. "Discovery of a Narrow Resonance in e^+e^- Annihilation". In: *Phys. Rev. Lett.* 33 (1974), pp. 1406–1408. DOI: 10.1103/PhysRevLett.33.1406.

[69] J. J. Aubert et al. "Experimental Observation of a Heavy Particle J". In: *Phys. Rev. Lett.* 33 (1974), pp. 1404–1406. DOI: 10.1103/PhysRevLett.33.1404.

[70] G. Burdman et al. "Rare charm decays in the standard model and beyond". In: *Phys. Rev.* D66 (2002), p. 014009. DOI: 10.1103/PhysRevD.66.014009. arXiv: hep-ph/0112235 [hep-ph].

[71] Roel Aaij et al. “Search for lepton-universality violation in $B^+ \to K^+\ell^+\ell^-$ decays”. In: *Phys. Rev. Lett.* 122.19 (2019), p. 191801. DOI: 10.1103/PhysRevLett.122.191801. arXiv: 1903.09252 [hep-ex].

[72] I. Dorsner et al. “Physics of leptoquarks in precision experiments and at particle colliders”. In: *Phys. Rept.* 641 (2016), pp. 1–68. DOI: 10.1016/j.physrep.2016.06.001. arXiv: 1603.04993 [hep-ph].

[73] Gustavo Burdman et al. “Rare charm decays in the standard model and beyond”. In: *Phys. Rev. D* 66 (1 July 2002), p. 014009. DOI: 10.1103/PhysRevD.66.014009. URL: https://link.aps.org/doi/10.1103/PhysRevD.66.014009.

[74] Glen Cowan et al. “Asymptotic formulae for likelihood-based tests of new physics”. In: *Eur. Phys. J. C* 71 (2011). [Erratum: Eur.Phys.J.C 73, 2501 (2013)], p. 1554. DOI: 10.1140/epjc/s10052-011-1554-0. arXiv: 1007.1727 [physics.data-an].

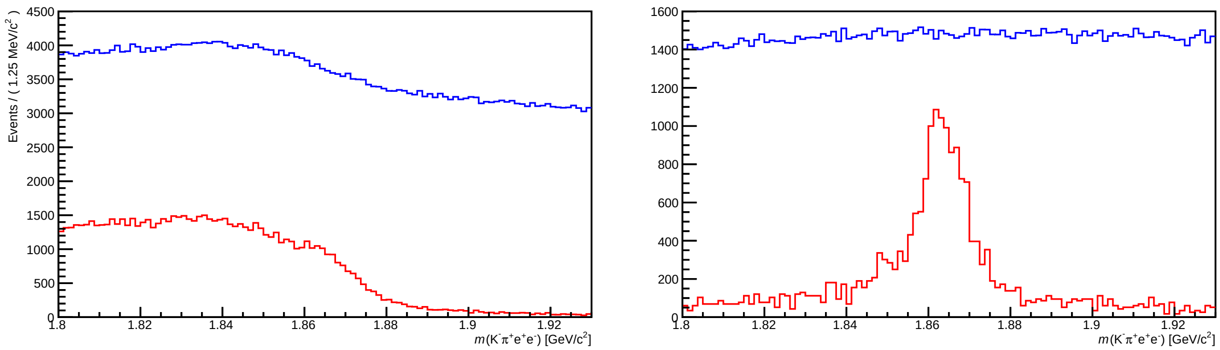

Figure A.1: $D^0 \to K^-\pi^+e^+e^-$ generic charm MC-simulated event m_{D^0} distributions after the preselection. The blue curves are the generic charm background. The red curves are the truth-matched signal (ignoring photons) and are scaled for better visualization.
In the left plot, the bumps at the low m_{D^0} region is due to the $D^0 \to K^-\pi^+\pi^0/\eta$ $[\pi^0/\eta \to e^+e^-\gamma]$ where the hard photon is not reconstructed. This also contributes to the red curve in the left plot at the low m_{D^0} region.
In the right plot, the charm background m_{D^0} distribution becomes flat after requiring $m_{ee} > 200$ MeV/c^2. The 200 MeV/c^2 cut is also applied to the $K^-K^+e^+e^-$ and $\pi^-\pi^+e^+e^-$ modes. For the Cabibbo favored decay $D^0 \to K^-\pi^+\eta$, we require $m_{ee} > 560$ MeV/c^2 for the m_{ee} region excluding ee resonances. The e bremsstrahlung recovery is not applied for m_{ee} at m_η $(520, 560)$ MeV/c^2 region to avoid recovering the hard photon from $\eta \to e^+e^-\gamma$. The red curve in the right plot is the truth-matched signal m_{D^0} with η and π^0 decay pollution vetoed, which shows the expected signal ee mode m_{D^0} shape.

A.1 Signal MC distributions

A.1.1 $D^0 \to \pi^-\pi^+e^+e^-$ resonance signal MC distributions after preselection

The $D^0 \to \pi^+\pi^-\eta/\phi\ [\eta/\phi \to ee]$ resonance signal MC-simulated events is shown as examples for showing signal modes MC-simulated event distributions m_{ee} (Figs A.2 - A.3) and PID responses (Figs A.4).

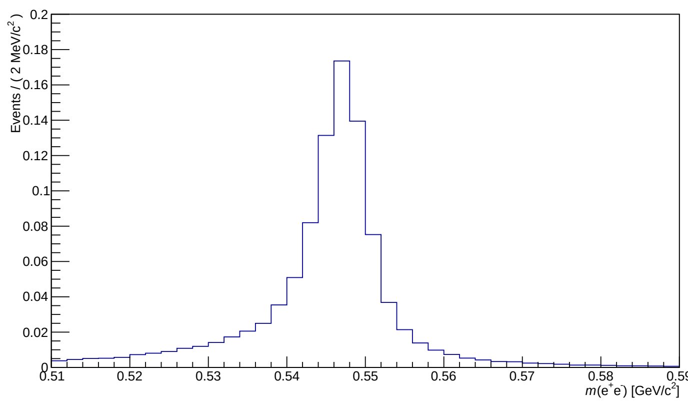

Figure A.2: $D^0 \to \pi^+\pi^-\eta\ [\eta \to ee]$ truth-matched signal MC. The resonance peaks at η mass ($\sim 548\,\mathrm{MeV}/c^2$) can be seen in the m_{ee} distribution. The low mass tail is because of electron bremsstrahlung.

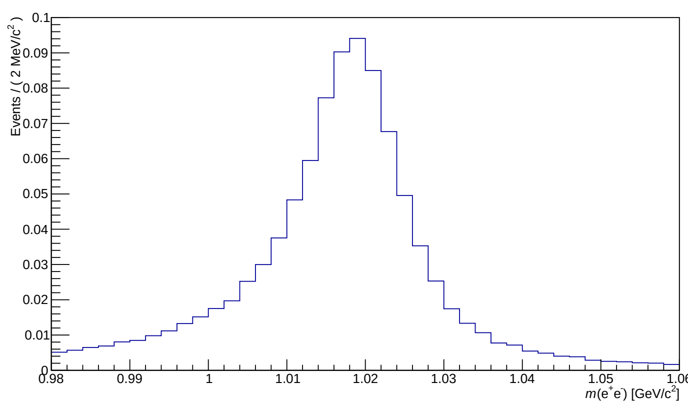

Figure A.3: $D^0 \to \pi^+\pi^-\phi\ [\phi \to ee]$ truth-matched signal MC. The resonance peaks at ϕ mass ($\sim 1.02\,\mathrm{GeV}/c^2$) can be seen in the m_{ee} distribution. The low mass tail is because of electron bremsstrahlung.

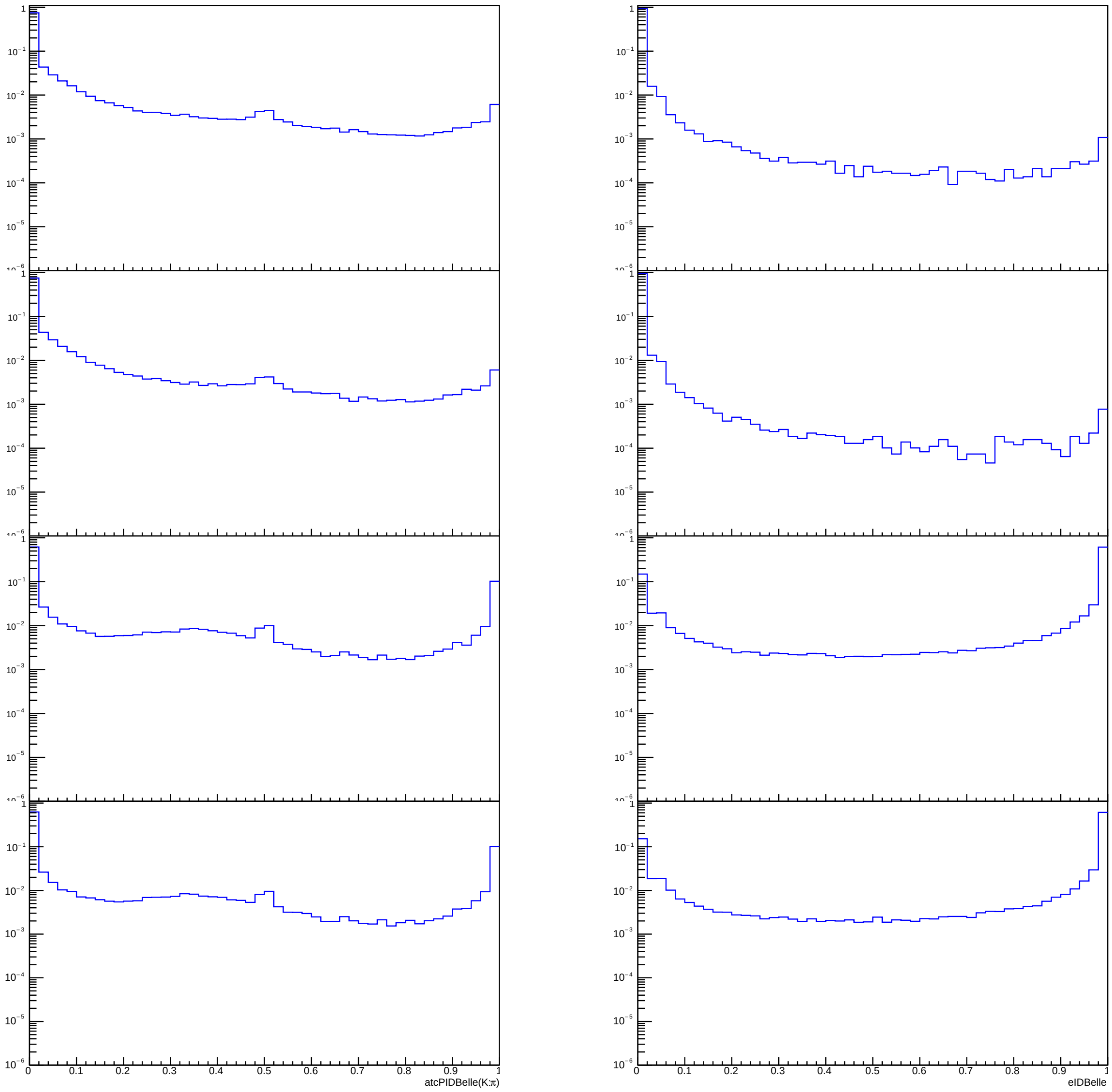

(a) KID (b) eID

Figure A.4: $D^0 \to \pi^+\pi^-\eta$ $[\eta \to ee]$ truth-matched signal MC PID responses. Each row gives the PID response for the four tracks from D^0 (from top to bottom: π^+, π^-, e^+, e^-). Each column gives the PID output for that track (left: KID, right: eID)

A.1.1.1 Signal MC m_{D^0} fit PDF parameters

The corresponding resonance signal MC ($\rho \to ee$) is used as examples for showing the m_{D^0} fit of all signal modes (Figure A.5).

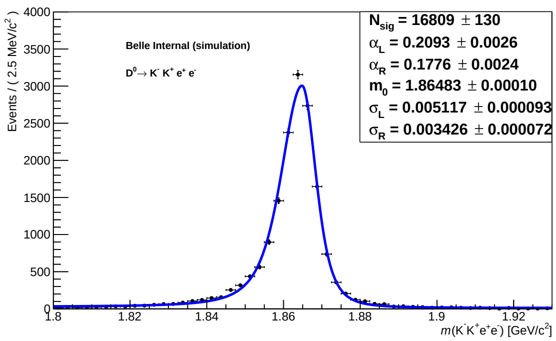

(a) $K^-K^+e^+e^-$

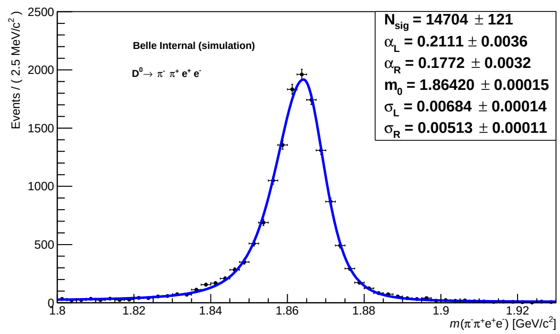

(b) $\pi^-\pi^+e^+e^-$

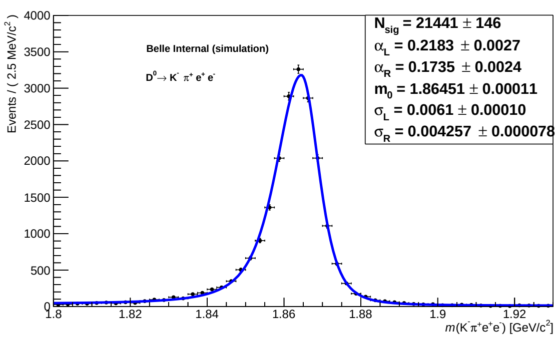

(c) $K^-\pi^+e^+e^-$

Figure A.5: $D^0 \to h^-h^{(\prime)+}e^+e^-$ signal MC m_{D^0} fit. The m_{D^0} distribution left tail is because of the electron bremsstrahlung.

A.1.2 Generic MC distributions of $K^-\pi^+e^+e^-$, $K^-K^+e^+e^-$, $\pi^-\pi^+e^+e^-$ and normalization mode $K^-\pi^+\pi^-\pi^+$

A.1.2.1 $D^0 \to K^-\pi^+e^+e^-$

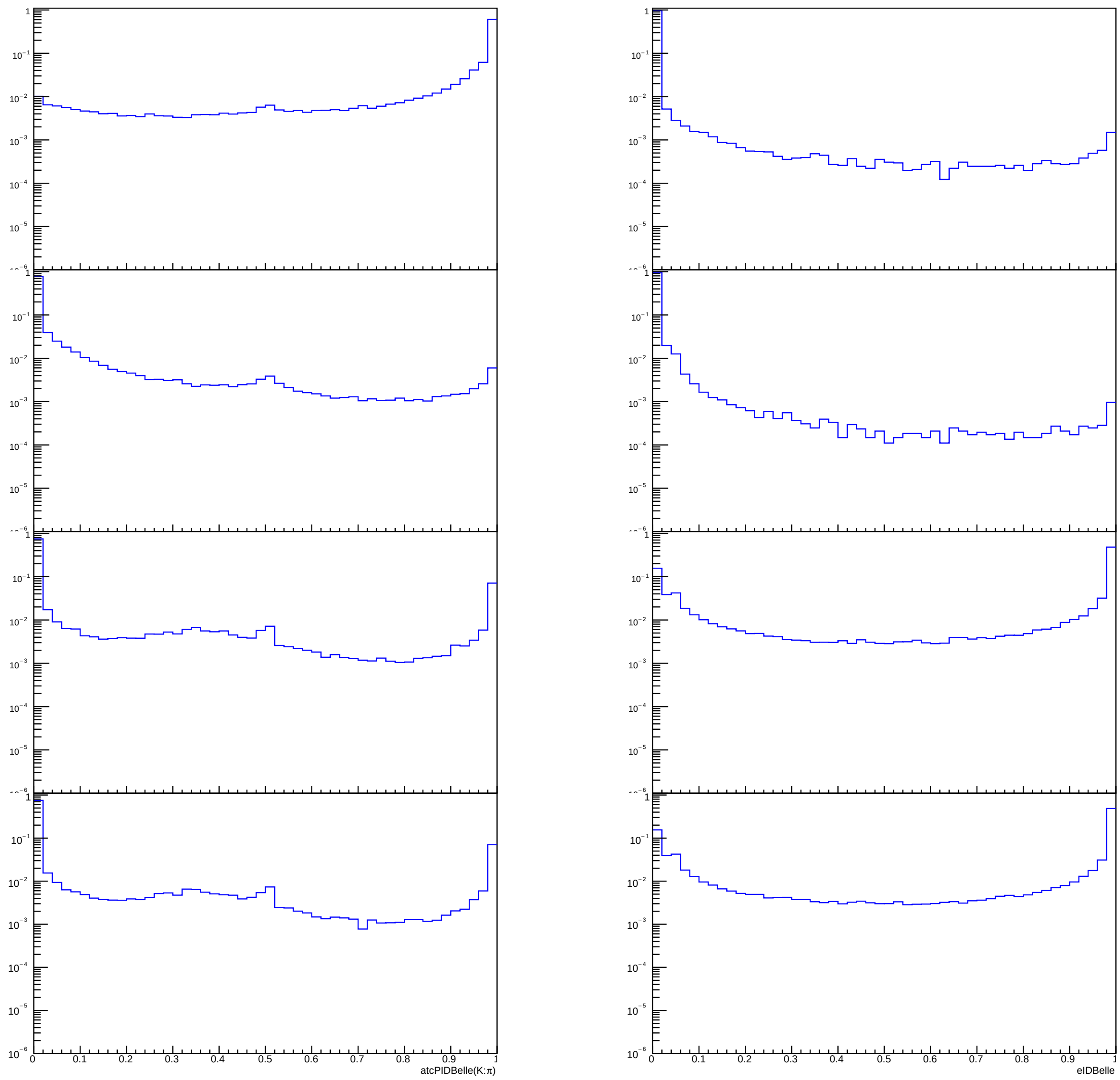

(a) KID (b) eID

Figure A.6: $D^0 \rightarrow K^-\pi^+e^+e^-$ (γ) generic charm MC PID response. Each row gives the PID response for the four tracks from D^0 (from top to bottom:K^-, π^+, e^+, e^-). Each column gives the PID output for that track (left: KID, right: eID). The PID responses for the corresponding correct particle are populated close to one, whereas the others are not.

A.1.2.2 $D^0 \to K^- K^+ e^+ e^-$

Besides the mass peak at $\phi \sim 1.02$ GeV/c^2 in the Figure A.7 a, other peaks at ~ 1.2 and 1.6 GeV/c^2 are from the decay $D^0 \to K^{*+}\ K^-$, with $K^{*+} \to \pi^0\ K^+$ and $\pi^0 \to e^+\ e^-\ \gamma$. The m_{ee} peak near zero as shown in Figure A.7 b is contributed by photon pole mode decay $D^0 \to K^-\ K^+\ \gamma$ with $\gamma \to e^+ e^-$. Another peak at ~ 0.12 GeV/c^2 is from $\pi^0 \to e^+\ e^-\ \gamma$, where the γ is not reconstructed. As mentioned in the preselection, we require $m_{ee} > 200\,\text{MeV}/c^2$ which suppresses the photon pole mode and π^0 decays pollution. The PID responses are shown at last in Figure A.8.

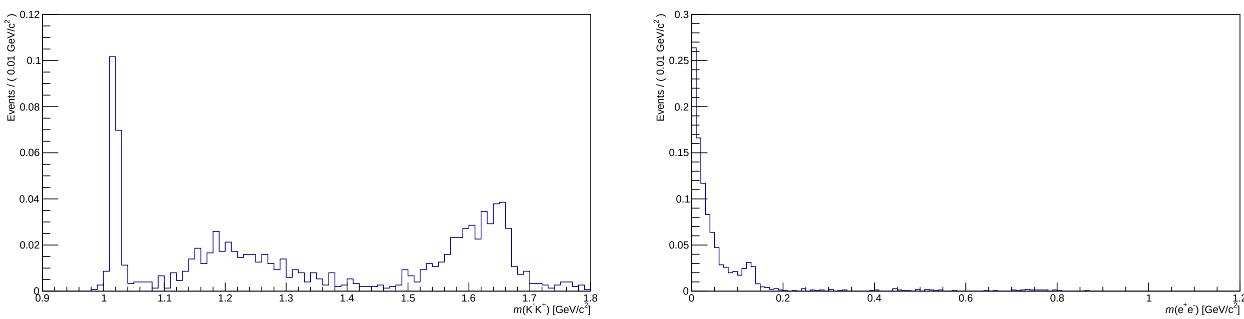

(a) $m_{K^+K^-}$

(b) m_{ee}

Figure A.7: $D^0 \to K^- K^+ e^+ e^-$ truth-matched generic charm MC distribution

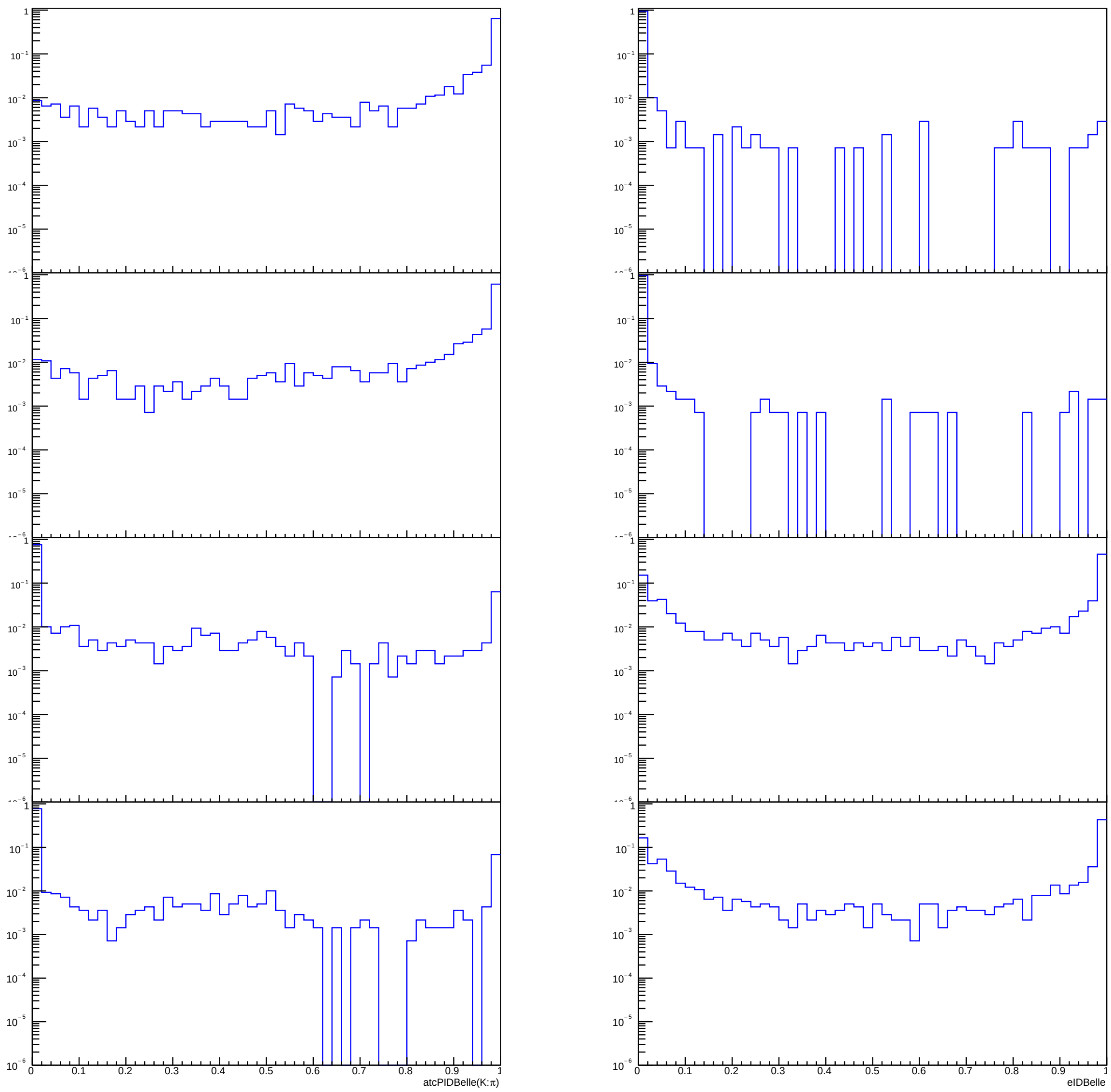

(a) KID (b) eID

Figure A.8: $D^0 \to K^- K^+ e^+ e^-$ truth-matched generic charm MC PID response. Each row gives the PID response for the four tracks from D^0 (from top to bottom: K^-, π^+, e^+, e^-). Each column gives the PID output for that track (left: KID, right: eID)

A.1.2.3 $D^0 \to \pi^-\pi^+e^+e^-$

Besides the mass peak at $\rho \sim 0.78$ GeV/c^2 in the Figure A.9 (a), another peak at ~ 0.6 and 1.6 GeV/c^2 are from the decay $D^0 \to \rho^+ \, \pi^-$, with $\rho^+ \to \pi^0 \, \pi^+$ and $\pi^0 \to e^+ \, e^- \, \gamma$. The m_{ee} peaks at ~ 0 and 0.12 GeV/c^2 as shown in Figure A.9 (b) are contributed by photon pole mode decay $D^0 \to \pi^- \, \pi^+ \, \gamma$ with $\gamma \to e^+e^-$, and $D^0 \to \pi^- \, \pi^+ \, \pi^0$ with $\pi^0 \to e^+ \, e^- \, \gamma$, where γ is not reconstructed. The peak at $\phi \sim 1.02$ GeV/c^2 can be also seen in Figure A.9 (b). The PID responses are shown at last in Figure A.10.

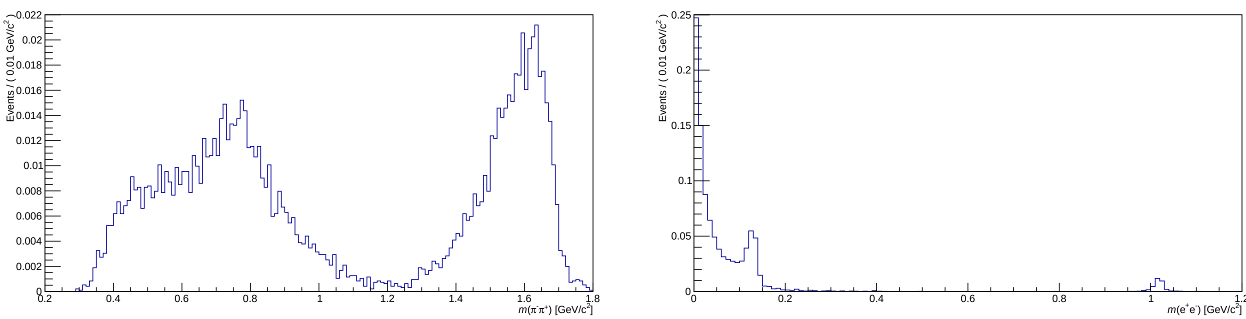

(a) $m_{\pi^+\pi^-}$ (b) m_{ee}

Figure A.9: $D^0 \to \pi^-\pi^+e^+e^-$ truth-matched generic charm MC distribution

A.1.2.4 $D^0 \to K^-\pi^+\pi^-\pi^+$

The PID responses for the truth-matched $D^0 \to K^-\pi^+\pi^-\pi^+$ decay are given in Figure A.11.

A.1.3 $D^0 \to K^-\pi^+e^+e^-$ FOM distributions

Figure A.12 shows the FOM distributions for $D^0 \to K^-\pi^+e^+e^-$ with $m_{ee} \in m_{\rho/\omega}$ decay using six streams of Belle Generic MC-simulated events and $\sim$ 400k $D^0 \to K^-\pi^+e^+e^-$ ρ resonance signal MC-simulated events.

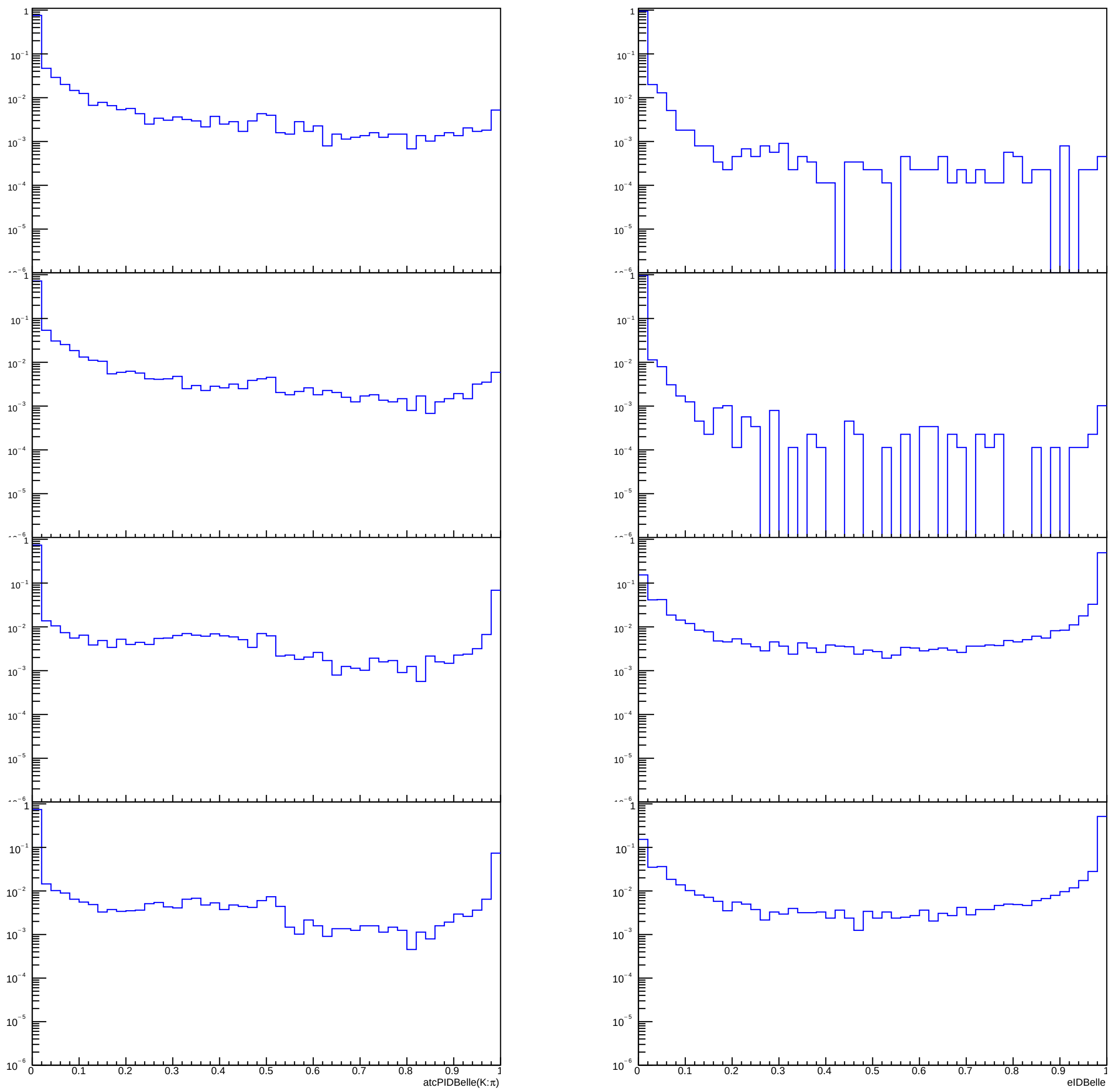

(a) KID

(b) eID

Figure A.10: $D^0 \to \pi^-\pi^+e^+e^-$ truth-matched generic charm MC PID response. Each row gives the PID response for the four tracks from D^0 (from top to bottom: K^-, π^+, e^+, e^-). Each column gives the PID output for that track (left: KID, right: eID)

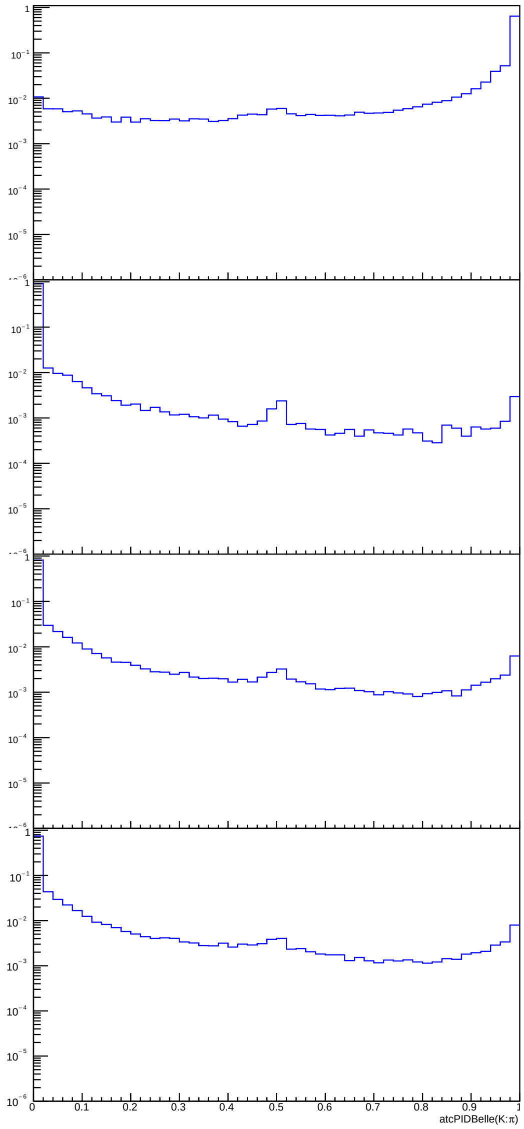

(a) KID

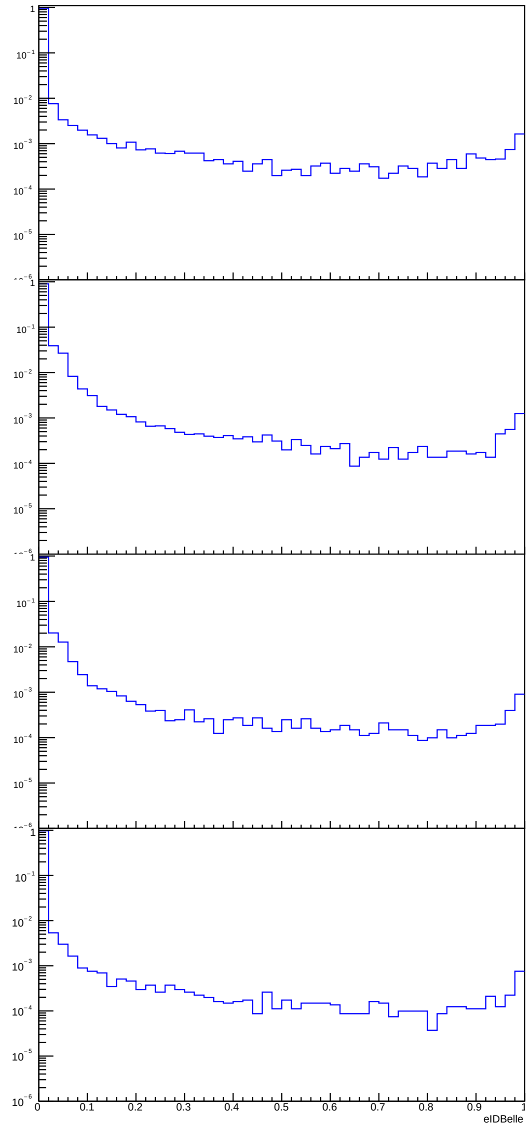

(b) eID

Figure A.11: $D^0 \to K^-\pi^+\pi^-\pi^+$ truth-matched generic MC PID response. Each row gives the PID response for the four tracks from D^0 (from top to bottom: K^-, π^+, π^-, π^+). Each column gives the PID output for that track (left: KID, right: eID).

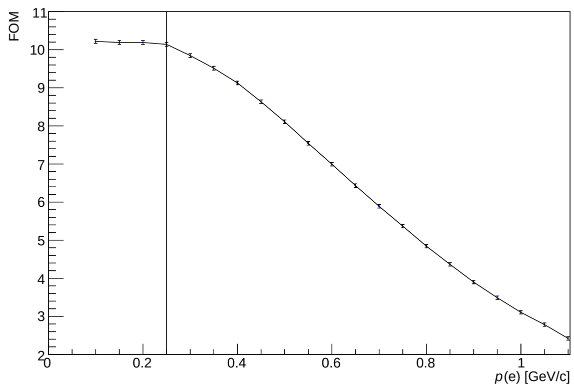

(a) $p(e)$

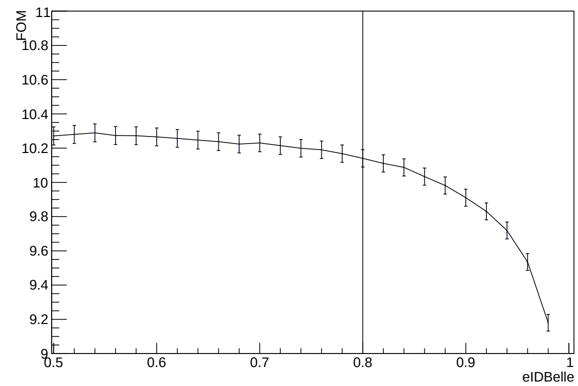

(b) eID

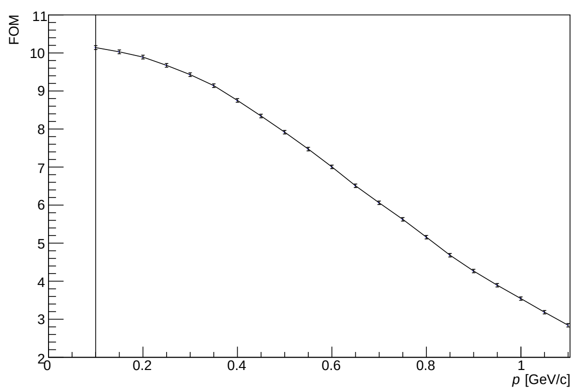

(c) $p(\notin e)$

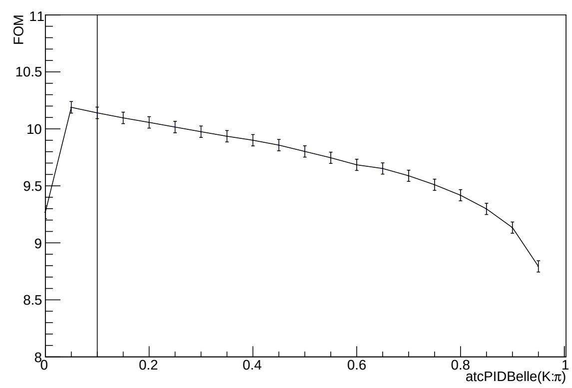

(d) KID

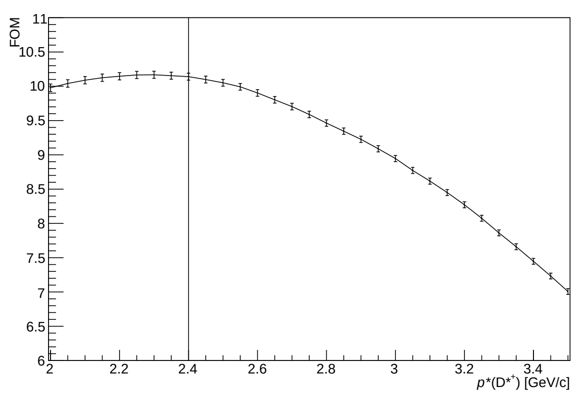

(e) $p^*(D^{*+})$

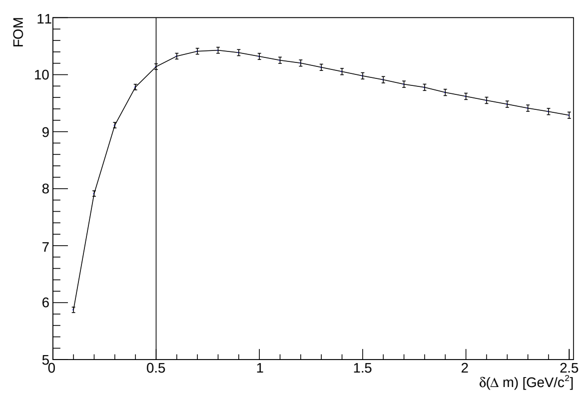

(f) $\delta(\Delta m)$

Figure A.12: $D^0 \to K^- \pi^+ e^+ e^-$ with $m_{ee} \in m_{\rho/\omega}$ FOM distributions. In each distribution the other variables are set to the optimized values. The vertical line indicates the final optimized selection.

A.1.4 Signal modes optimized selections for m_{ee} in $m(\rho/\omega), m(\phi)$ and non-resonant m_{ee} regions.

Table A.1: Optimized selection criteria for m_{ee} in ρ/ω mass region ($K^-\pi^+e^+e^-$, $\pi^-\pi^+e^+e^-$: $675 < m_{ee} < 875$ MeV/c^2, $K^-K^+e^+e^-$: $m_{ee} > 675$ MeV/c^2).

Modes $D^0 \to$	$K^-\pi^+e^+e^-$	$K^-K^+e^+e^-$	$\pi^-\pi^+e^+e^-$
Impact parameter selection:			
d_0 [cm]		< 0.25	
z_0 [cm]		< 4.5	
K selection:			
KID	> 0.1		-
eID	< 0.6	< 0.2	-
π selection:			
KID	-		< 0.4
eID	< 0.6	< 0.2	< 0.05
e selection:			
p_e [GeV/c]	> 0.25		> 0.3
eID	> 0.8		> 0.9
$p^*(D^{*+})$ [GeV/c]	> 2.4		> 2.5
$P(\chi^2_{D^{*+}})$		> 0	
$\delta(\Delta m)$ [MeV/c^2]		< 0.5	
Photon conversion veto:			
$P(\chi^2_{\gamma^*})$		> 0	
θ_{ee} [rads]	< 0.07 or	< 0.06 or	< 0.08 or
m_{ee} [GeV/c^2]	< 0.1	< 0.06	< 0.04
Hadronic D^0 decay veto:			
$P(\chi^2_{D^{*+}})$		> 0	
$\delta(\Delta m)$ [MeV/c^2]	< 0.4	< 0.5	< 0.8
$\delta(m_{D^0})$ [MeV/c^2]	< 3	< 5	< 10
Best candidate selection:		closest to the nominal value of Δm	

Table A.2: Optimized selection criteria for m_{ee} in ϕ mass region ($K^-\pi^+e^+e^-$: $990 < m_{ee} < 1034$ MeV/c^2, $\pi^-\pi^+e^+e^-$: $995 < m_{ee} < 1035$ MeV/c^2).

Modes $D^0 \to$	$K^-\pi^+e^+e^-$	$\pi^-\pi^+e^+e^-$
Impact parameter selection:		
d_0 [cm]	< 0.25	
z_0 [cm]	< 4.5	
K selection:		
KID	> 0.1	-
eID	< 0.6	-
π selection:		
KID	-	< 0.7
eID	< 0.6	
e selection:		
p_e [GeV/c]	> 0.3	
eID	> 0.8	
$p^*(D^{*+})$ [GeV/c]	> 2.5	
$P(\chi^2_{D^{*+}})$	> 0	
$\delta(\Delta m)$ [MeV/c^2]	< 0.5	<0.4
Photon conversion veto:		
$P(\chi^2_{\gamma^*})$	> 0	
θ_{ee} [rads]	< 0.1 or	< 0.04 or
m_{ee} [GeV/c^2]	< 0.06	< 0.04
Hadronic D^0 decay veto:		
$P(\chi^2_{D^{*+}})$	> 0	
$\delta(\Delta m)$ [MeV/c^2]	< 0.4	< 0.5
$\delta(m_{D^0})$ [MeV/c^2]	< 3	< 5
Best candidate selection:	closest to nominal value of Δm	

Table A.3: Optimized selection criteria for m_{ee} non-resonant regions ($K^-\pi^+e^+e^-$: $m_{ee} \in$ (560, 675), (890, 990), (> 1034) MeV/c^2, $\pi^-\pi^+e^+e^-$: $m_{ee} \in$ (200, 520), (560, 675), (875, 995), (> 1035) MeV/c^2, $K^-K^+e^+e^-$: $m_{ee} \in$ (200, 520), (560, 675) MeV/c^2).

Modes $D^0 \to$	$K^-\pi^+e^+e^-$	$K^-K^+e^+e^-$	$\pi^-\pi^+e^+e^-$
Impact parameter selection:			
d_0 [cm]		< 0.25	
z_0 [cm]		< 4.5	
K selection:			
KID	> 0.1	> 0.1	-
eID	< 0.2	< 0.2	-
π selection:			
KID	-	-	< 0.4
eID	< 0.2	< 0.2	< 0.05
e selection:			
p_e [GeV/c]	> 0.35	> 0.25	> 0.35
eID	> 0.8	> 0.8	> 0.9
$p^*(D^{*+})$ [GeV/c]	> 2.7	> 2.5	> 2.8
$P(\chi^2_{D^{*+}})$		> 0	
$\delta(\Delta m)$ [MeV/c^2]		< 0.4	
Photon conversion veto:			
$P(\chi^2_{\gamma^*})$		> 0	
θ_{ee} [rads]	< 0.04 or	< 0.04 or	< 0.04 or
m_{ee} [GeV/c^2]	< 0.08	< 0.06	< 0.04
Hadronic D^0 decay veto:			
$P(\chi^2_{D^{*+}})$		> 0	
$\delta(\Delta m)$ [MeV/c^2]	< 0.8	< 0.4	< 0.8
$\delta(m_{D^0})$ [MeV/c^2]	< 5	< 5	< 10
Best candidate selection:		closest to nominal value of Δm	

A.1.5 Background compositions after final selection

The background after final selections is studied using basf2 topoana module. For simplify, the corresponding non-resonant selections are applied to the $K^-\pi^+e^+e^-$ and $\pi^-\pi^+e^+e^-$ modes. The $K^-K^+e^+e^-$ background composition is not studied due to low statistics after the final selection. The dominant background are semi-leptonic B or D/D_s decays.

Table A.4: Background compositions after final selections [%].

Modes $D^0 \to$	$\pi^-\pi^+e^+e^-$	$K^-\pi^+e^+e^-$
events / total background		
$c\bar{c}$ background	41	61
$b\bar{b}$ background	46	36
events / $q\bar{q}$ background		
At least a e from semi-leptonic D or D_s [$c\bar{c}$]	67	70
At least a e from semi-leptonic B or D [$b\bar{b}$]	68	69